DOCTOR OF PHILOSOPHY

Laboratory modelling of breaking internal solitary waves

Franklin, James

Award date:
2014

College of Art, Science & Engineering

School of Engineering, Physics and Mathematics

Division of Civil Engineering

Laboratory modelling of breaking internal solitary waves

James Franklin

A dissertation submitted for the

degree of Doctor of Philosophy

to the University of Dundee

21st July 2014

Declaration

This is to certify that (i) the candidate is the author of this thesis, (ii) all references cited have been consulted by the candidate, unless otherwise stated, (iii) the work of which the thesis is a record has been done by the candidate and (iv) the thesis has not been previously accepted for a Higher Degree.

James Franklin (candidate), Dundee, 21st July 2014

Prof. Peter Davies (supervisor), Dundee, 21st July 2014

Acknowledgements

This work was funded jointly by Engineering and Physical Sciences Research Council (EPSRC) and Northern Research Partnership (NRP) PhD studentships. A further award (Lessells Travel Scholarship) from the Royal Society of Edinburgh allowed me to travel to the University of Oslo, Norway to carry out a programme of laboratory experiments, thereby enhancing my work considerably. I am grateful to my supervisors Prof. Peter Davies, Dr. Magda Carr and Dr. Yakun Guo for their direction and support. I would also like to thank Dr. Stuart King for additional guidance and support. I am indebted to the staff at the University of Oslo for making me welcome and allowing me the use of their laboratory, particularly Prof. John Grue and Prof. Atle Jensen.

I would like to thank all the technical staff within the Department of Civil Engineering at the University of Dundee. I would like to thank, in particular, John Anderson for his guidance and hard work with apparatus development and Mike McKernie for help with instrumentation. Last but not least I want to thank Emma my wife for her continuing support and encouragement.

Abstract

Results are presented from a laboratory modelling investigation of internal solitary waves (ISWs) that were breaking in shallow, stably-stratified fluid systems. The mechanism(s) for wave breaking were investigated with 2- and 3-layer density configurations. Velocity and density measurements have been made of the internal structure of the breaking waves for cases in which the flow was generated by Kelvin-Helmholtz (KH), Holmboe (H) and convectional instability. Where appropriate comparisons were made with (i) existing numerical models of ISW breaking and (ii) KH and/or H billows produced on uniformly stratified shear flows. For 3-layer configurations the spatial and temporal development of billows, generated through KH and/or H shear instability, was measured as a function of the parameters of the shear flow at the peak of the ISW.

The first key result of the study was to demonstrate that a non-dimensional scaling can be obtained to parameterise the time dependant behaviour of the billows. This enabled the growth rate of billows, with various initial conditions, to be collapsed onto one of three curves. It was possible to distinguish between the three curves, or billow types, by using the ratio of the velocity and density interfacial thicknesses (R). Knowing the vertical non-dimensional billow amplitude at saturation allowed the mixing per billow to be estimated. Hence a simple model to estimate the mixing due to a passing ISW in a 3-layer stratification was given. The second key result of the study was the quantification of the change in potential energy of the system caused by breaking ISWs in 2-layer density configurations. Measurement of the density field far upstream and 1 wavelength downstream of an ISW peak indicated that breaking ISWs were transitioning to ISWs with a rotating core. During the transition it was found that the entrainment of fluid within the core resulted in a local loss of potential energy to the background stratification (P_B).

Contents

Table of figures

Notation

a	Amplitude of ISW
a_1	ISW amplitude measured from the isopycnals that coincided with the smallest ISW amplitude
a_2	ISW amplitude measured from the isopycnals that coincided with the largest ISW amplitude
A_c	Area of a circular billow
A_s	Special measure of amplitude
a_s	Asymmetry of the density and velocity profiles
a_{sn}	Non-dimensional asymmetry of the density and velocity profiles
b	Buoyancy
B	Vertical buoyancy flux
c	Wave speed
c_0	Linear long wave speed
C_b	Horizontal component of billow speed
C_{best}	Estimated billow speed
C_{bmes}	Measured billow speed
C_c	Constant
C_{wave}	ISW speed
D	Mixed turbulent layer thickness
d'	Thorpe displacement
d_z	Interfacial thickness of the region of shear in a vertical velocity profile
E	Total Energy
E_n	Entrainment coefficient
Fr	Froude Number
g	Gravitational acceleration
g'	Reduced gravitational acceleration
H	Total depth of water in tank
h_1	Upper layer thickness accounting for half the pycnocline
H_1	Layer depth in the density stratification
$\hat{H}_1$	Average of layer depths H_1 and H_2
h_2	Lower layer thickness accounting for half the pycnocline
H_2	Layer depth in the density stratification
$\hat{H}_2$	Average of layer depths H_2 and H_3
H_3	Layer depth in the density stratification
H_e	Vertical height of billow when spatially averaged
H_s	Vertical height of billow at saturation when spatially averaged
k	Wave number
KE	Kinetic energy
K_m	Eddy viscosity (vertical momentum)
K_p	Eddy viscosity (vertical mass)
L	Tank dimension in x direction
L_b	Vertical amplitude of a billow
L_G	Partially submerged gate position in the x direction
L_k	Kolmogorov scale
L_{max}	Vertical amplitude of a billow at saturation

L_o	Ozmidov length scale
L_R	Length scale associated with the flow
L_T	Thorpe Scale
L_{Tmax}	Maximum Thorpe scale
L_x	Horizontal length of the pocket of instability
L_x	Length of the pocket of instability in the x direction
M	Mixing rate
N	Buoyancy frequency
n	Constant
N_{max}	Maximum Buoyancy frequency
N_w	Number of waves
P	Production of TKE
P_A	Available potential energy
P_B	Background Potential energy
P_{Bs}	Monotonically reordered background Potential Energy
PE	Potential Energy
Pr	Prandtl Number
R	Scale ratio
r	Radius of a billow
Re	Reynolds number
Re_{trans}	Transitional Reynolds number
Ri_B, J	Bulk Richardson Number
Ri_c	Critical Richardson Number
Ri_f	Flux Richardson number
Ri_g	Gradient Richardson Number
Ri_{min}	Minimum Richardson Number
r_{max}	Radius of circular billow at saturation
S	Velocity shear
s	Amplitude to billow wavelength ratio
TKE	Turbulent Kinetic Energy
T_w	Time over which parcels of fluid were subjected to Ri_g<0.25
U	Mean flow in the x direction
U_{core}	Horizontal component of flow of the rotating ISW core
U_{wave}	Horizontal component of flow of the ISW wave
u	Small vertical displacement
u'	Turbulent fluctuation (from the mean value) of the x directed velocity component
u_e	Entrainment velocity
u_{emax}	Entrainment velocity calculated using r_{max}
V	Voltage
v	Velocity scale associated with the flow
w'	Turbulent fluctuation (from the mean value) of the z directed velocity component
Z	Maximum amplitude of an ISW when approximated with the KdV equation
α	Non-dimensional wave number
α_T	Constant relating L_o to L_T
Γ	Mixing efficiency
ΔzN	Vertical resolution when measuring N

ε	Viscous dissipation rate
η	Vertical displacement of an isopycnal
η_0	Excursion of the pycnocline due to the volume added behind the gate
κ	Thermal diffusion rate
λ	ISW wavelength
λ_B	Billow wavelength
λ_H	ISW wavelength of Half width
ρ	Density
ρ_0	Reference density
$\rho_{1...3}$	Density of layer 1...3
ρ_{av}	Average density
σ_i	Average growth rate of the instability in the pocket of where Ri_g<0.25
τ	Reynolds stress
υ	Kinematic viscosity
$^{\circ}E$	Easting
$^{\circ}N$	Northing

1 Introduction

The focus of this PhD thesis is the laboratory study of internal solitary waves (ISWs) that are breaking in shallow, stably-stratified fluid systems. The study addresses the lack of current understanding of the mechanisms which lead to wave breaking for different density field conditions. There is a need for quantitative laboratory data on (i) the consequences of breaking for the structure of the ISW and (ii) the characteristic spatial and temporal features of the billows that form as a result of breaking. Addressing these knowledge gaps will enable oceanographic field observations of breaking ISWs to be understood more fully and the consequences of wave breaking to be parameterised more satisfactorily than at present.

ISWs are nonlinear, finite-amplitude, non-oscillatory, pulse-like disturbances that appear as a hump of water with either a crest but no trough (wave of elevation) or a trough but no crest (wave of depression). They propagate with permanent form on density interfaces, maintaining their shape through a balance of dispersion and nonlinearity, processes that in isolation tend to broaden or sharpen the wave respectively (Sutherland, 2010). Flows in the environment are often density-stratified via vertical variations in temperature, variations in salinity or a combination of both of these effects. Such flows are statically stable when the density increases with depth (i.e. the direction of the gravitational acceleration vector). A ubiquitous feature of stably-stratified oceans, coastal seas, estuaries and lakes is the internal wave (Sutherland, 2010) and, in particular to this study, the ISW a subset of internal waves. In these environments, ISWs are generated primarily by tidal motions over sub-sea ridges or continental shelves (e.g. Moum *et al*., 2003), wind-induced internal seiches (e.g Horn *et al*., 2001) or freshwater outflows (Nash & Moum, 2005).

In the peak of an ISW, shear instabilities such as the Kelvin-Helmholtz (KH) and Holmboe (H) instabilities can develop. These instabilities roll up into billows, the billow saturate when the buoyant force becomes dominant over the shearing force. The billows then undergo a transition to turbulence, during this process some of the fluid entrained in the billows is mixed, thereby raising the potential energy of the background stratification (P_B). This process will be referred to as breaking. Breaking ISWs redistribute passive marine organisms that can function as biological tracers, apply undesirable forces to subsea structures and, not least, are an important sink of energy in the energy balance of oceanographic and weather models.

The laboratory investigation of breaking ISWs was undertaken for two different vertical density stratification configurations. The first was typical of stratifications in the ocean, referred to as a three layer stratification and the second was a stratification that is less common, referred to as a two layer stratification. KH billows have been studied extensively on horizontal shear flows in various experimental setups. The results of these experiments were complicated by the measurement of the velocity interfacial thickness (d_z) which was developing either temporally and/or spatially. ISWs are unique in that instabilities are repressed in the front of the ISW where the shear flow accelerates. At the ISW peak, where instabilities are not repressed, the shear flow is relatively constant with time. Consequently breaking ISWs offered a unique opportunity to study KH and H billows that have occurred under relatively similar conditions when compared to previous experimental investigations.

The document is organised as follows: Chapter 1 gives a broad introduction and some historical context to breaking ISWs. Chapter 2 reviews the previous laboratory, field and

numerical studies in the relevant subject areas and introduces some key concepts. Chapters 3 and 4 discuss the experimental method for the three and two layer experiments respectively. Chapters 5 and 7 highlight the key experimental observations for the two main groups of experiments. Chapters 6 and 8 respectively deliver the experimental findings from these groups and discuss the findings in the context of the subject area. Chapter 9 provides a summary of the findings, the bounds of their applicability and offers ideas for future research in the area.

1.1 Surface solitary wave

Though the focus of this thesis is the internal solitary wave (ISW), it is useful to place the properties of such flows in a historical context and to make reference to the first descriptions of solitary waves, as they occurred on the free surface of a water channel. John Scott Russell (1808-1882) was first to observe and recognise the significance of a surface solitary wave while conducting experiments in the Union Canal near Edinburgh for an entirely different purpose (Eilbeck, 2013). The surface solitary wave or 'wave of translation' (as Russell called it) appeared on the surface of the water in the canal as a smooth hump of water with no trough. It was generated when a barge being pulled on the canal was suddenly brought to rest. Russell recalls that the wave was of constant form and speed and that it lost little height as it travelled along the canal.

An important result, which Scott Russell later demonstrated experimentally, was that the square of the solitary wave phase speed c increased approximately linearly with wave amplitude a in the range he sampled. That is,

$$c^2 = g(H+a) \qquad \text{Equation 1}$$

where: g is the acceleration due to gravity, H is the depth of water and a is the amplitude of the wave. Wave theory at the time ($u_t+u_{xxx}=0$, where: u is a small vertical displacement at horizontal position x and time t, u_t is the time evolution of the wave and u_{xxx} is the linear dispersive term) was able to model linear and dispersive wave motion but could not represent the surface solitary wave that Russell had observed. For the solitary wave, the assumption that the amplitude of the wave is small compared to the water depth has to be discarded. In doing so Korteweg and De Vries in 1895 (Miles, 1981) proposed Equation 2 commonly referred to as the KdV equation to describe the solitary wave.

$$u_t + u\,u_x + u_{xxx} = 0 \qquad \text{Equation 2}$$

Where: uu_x is a nonlinear term responsible for the steepening of the wave and suffices represent partial derivatives with regard to either x or t as appropriate. The assumption that the wavelength is large compared to the water depth was retained such that the equation still describes shallow water waves. It should be noted that Equation 2 has also been published by Boussinesq in 1872, 1877 and Rayleigh in 1976 in different forms (Miles, 1981). The KdV equation represents the simplest combination of dispersion and nonlinearity for a propagating wave. A solution representing a soliton (or, more generally, a solitary wave) would have these two effects in exact balance. It is useful to note that the meaning of 'soliton' is subtly different from that of a solitary wave (Zabusky & Kruskal, 1965; Weidman & Maxworthy, 1978). When solitary waves collide or interact and emerge unchanged in form and speed whilst also not obeying the principle of superposition they are called solitons. The term 'internal soliton' has been used in the literature to delineate the behaviour of internal solitary waves and internal solitons. In this study, where collisions and interactions of ISWs are not considered, the terms 'internal soliton' and 'internal solitary wave' may be used interchangeably. For consistency, the latter has been adopted throughout the thesis.

1.2 Internal waves

Internal waves (more specifically interfacial internal waves) require a statically-stable, vertically-stratified fluid system (i.e. a less dense fluid overlying a more dense fluid) in order to propagate. An initial disturbance is required to vertically displace a density surface in order to generate an internal wave. Following such a disturbance, the propagation of an internal wave takes place horizontally along the interface under the restoring action of gravity (buoyancy). A small parcel of fluid that has been displaced vertically from its rest height will experience a vertical restoring force (buoyancy) due to gravity acting on the density difference between the fluid parcel and its new surroundings. The restoring force moves the parcel back toward its rest height but due to the momentum carried by the parcel it will overshoot this position, leading to an oscillation of characteristic frequency N determined by the strength of the undisturbed density gradient $\partial\rho/\partial z$ in the fluid. The frequency $N(z)$ is conventionally denoted as the buoyancy (or Brunt-Väisälä) frequency and is a function of the vertical coordinate (z) in the stably stratified system. For a linearly-stratified system, N is a constant. An internal wave is a collection of oscillating fluid parcels. The continuous nature of water, at a macroscopic scale, allows internal waves to transmit energy through the medium. Homogenous bodies of water cannot support internal waves; a disturbance in a homogenous system has no restoring force (other than along its upper air-water interface) and therefore cannot propagate. In a continuous stratification, where the density continuously increases with depth across the whole depth, internal waves can still propagate horizontally along isopycnals (contours of constant density) but their energy may also propagate vertically along the density gradients; these waves are normally referred to as wave rays or beam (Munk, 1981). Continuous stratifications are not considered further, to do so would expand the scope of this thesis beyond manageable limits.

The first record of laboratory experiments on standing internal waves was found in a letter sent by Benjamin Franklin whilst sailing to Madeira 1762 (Gill, 1982). In the letter Franklin noted his observations of the motions within an oil and water lamp. He noted that *"..tho' the surface of the oil was perfectly tranquil, and duly preserved its position and distance with regard to the brim of the glass, the water under the oil was in great commotion rising and falling in irregular waves."*. The effect of oceanic internal waves had been recorded for centuries before Franklin made his observations of internal waves in oil and water lamps. Nansen had experienced the dead water phenomenon whilst onboard the polar exploration vessel *Fram* (1893-1896), where his vessel was unable to move forward even under full power. In a letter to Nansen, in 1898, Bjerknes may have been the first to attribute the so-called 'dead water phenomenon' to internal waves. Subsequently, in 1904 Ekman, Bjerknes' PhD student, substantiated what Bjerknes had suspected in a series of experiments, verifying that the deadwater phenomenon (i.e. the failure of a vessel to advance in regions in which the water column is stratified) was due to the energy intended for propulsion being lost wholly to the generation of internal waves (Gill, 1982).

KdV theory developed for surface waves can also be applied to waves at the interface of two superimposed immiscible fluids of different density (internal waves) (Long, 1956, Part II). Seeking exact analytical solutions to the KdV equation, relationships between excursion (η), amplitude (a), wavelength (λ) and speed (c) can be obtained. One such relationship can be seen in Equation 3 (Long, 1956, Part II). Non-periodic solutions to the KdV equation give rise to solitary waves, whereas periodic solutions to the KdV equation result in cnodial waves

$$\eta(x,t) = -a\,\mathrm{sech}^2[(x-ct)/\lambda] \qquad \text{Equation 3}$$

Nonlinear waves, such as ISWs, propagate faster than their linear counterparts so that $c>c_0$. Long (1956, Part II), and later documented by Grue *et al.* (1999), showed that the linear long wave speed (c_0) of an internal wave could be estimated using Equation 4 assuming $h_1<h_2$.

$$c_0^2 = \frac{[gh_2h_1(\rho_2-\rho_1)]}{(\rho_1h_2)+(\rho_2h_1)} \qquad \text{Equation 4}$$

Where h_1 and h_2 are the upper layer and lower layer of the density stratification respectively and $\rho_{1...2}$ are the respective densities. The interfacial layer in this case was assumed to be vanishingly thin. For three layer stratifications, where the interfacial layer could not be assumed to be vanishingly thin, c_0 was estimated with Equation 5 (Fructus *et al*., 2009).

$$c_0 = (N H_2) / Y \qquad \text{Equation 5}$$

Where N is the buoyancy frequency, Y is some function of H_1/H_2 and H_3/H_2, H_1 is the thickness of the upper layer, H_2 is the thickness of the interfacial layer and H_3 is the thickness of the lower layer in the vertical density stratification ($h_1+h_2 \approx H_1+H_2+H_3$). c_0 was used as a natural reference for the velocity of large amplitude ISWs, c/c_0 can be thought of as a measure of nonlinearity. The KdV equation has been studied extensively however its ability to mimic the behaviour of large amplitude ISWs was limited when the ISWs were highly nonlinear (King *et al.,* 2011). Hence recent investigators have turned to direct numerical simulation to study the large amplitude ISWs that were under investigation here.

1.3 Internal waves in the environment

Internal waves occur frequently in the Earth's atmosphere. Indications of their passing can be seen, for example, in wave clouds which appear as uniform stripes of cloud when viewed from above or from below. Such clouds are formed when parcels of atmosphere, in the peak of the internal waves, are vertically displaced, causing condensation of water vapour. This displacement could be attributed to a variety of internal waves. For example, standing

internal waves (lee waves), forming in the wake of some geographical feature (i.e. behind a mountain range), can lead to the formation of wave clouds. ISWs in the atmosphere can trap displaced air which then travels with the wave giving the appearance of a moving cloud stripe such as the Morning Glory cloud which is known to form in the Gulf of Carpentaria (Northern Australia).

Internal waves (or any flow involving statically-stable, vertically-stratified shear) in the environment may be susceptible to shear instabilities, leading to the formation of billows. Early evidence of shear instabilities forming on internal waves in stratified waters was recorded by Woods (1968), who photographed the evolution of a dye tracer released in the summer thermocline in the ocean. He noted that shear in the stratified regions resulted in the generation of 'breakers' or billows. More evidence of billows forming in stratified shear, although not necessarily due to internal waves was given by Thorpe (1977) who described billows forming on the thermocline in Loch Ness soon after the onset of surface shear (wind) while the loch was stratified. Further evidence of billows forming in stratified flows, not necessarily due to internal wave motion was given by De Silva *et al.* (1996) who reported that the amplitude of billows in the ocean can be in the range 5...20m and Luce *et al.* (2010) reported the occurrence of shear-induced billows 1.6km in amplitude in the atmosphere. Billows have been reported in a number of natural stratified flows, such as salt wedges in estuaries (Geyer & Smith, 1987) and stratified tidal flow over bathymetry (Farmer & Armi, 1999). Of particular importance for the present study is that several authors have recorded shear-induced billows forming on ISWs (Moum *et al.*, 2003; Lamb & Farmer, 2011).

The development of thermistor chains in the 1960's allowed the thermal density stratification in stratified oceans and lakes to be estimated (Helfrich & Melville, 2006). This led to improved observations of internal waves. Perry & Schimke (1965), notable early users of thermistor chains, recorded groups of internal waves of up to 82m in amplitude with wavefronts of 2000m propagating on the main thermocline in the Andaman Sea. The origin of the waves was shown (Osborn & Burch, 1980) to be tidal flow through the Andaman Nicobar Island chain. Therefore the internal waves recorded by Perry & Schimke had travelled hundreds of kilometres. These observations and others (Ziegenbein, 1970; Halpern, 1971) showed that the internal waves observed were nonlinear; i.e. they had a large amplitude compared with their wavelength. Furthermore, they were not dispersive; i.e. they retained a finite amplitude while travelling long distances. It appeared that the internal waves observed displayed several properties of internal solitary waves.

It was in the same period that that Gardener *et al*. (1967) obtained exact solutions to the KdV equation which could represent groups of rank-ordered solitary waves. Hunkins & Fliegel (1973) used KdV theory to show that the internal wave train that followed the internal undular surges in Seneka Lake were ISWs. Further evidence that ISWs were a common feature in nature came from advances in remote sensing. Ziegenbien (1970) and, later, Apel *et al*. (1975) demonstrated that ISWs could be detected from the scattering of marine radar. Seasat, the first remote sensing satellite, was equipped with Synthetic Aperture Radar (SAR) and the technique was able to show that ISW groups were commonly found to be separated by tidal periods (i.e. they were generated tidally, not from unusual conditions) and that ISWs were numerous in the ocean. Examples of SAR images can be found in Fu & Holt (1982). The satellite only functioned for 100 days but subsequent satellites deploying SAR technology benefited greatly from the experiences gained in the operation of Seasat.

On the water surface, internal waves and ISWs in oceans or lakes leave little observable indication of their passing. The surface roughness of the sea or lake is modulated by the passing of an ISW (Figure 1*(c)*), however this is only easily observable from aerial photography or satellite images. Although the surface signature of an ISW has been observed by research vessels (Ramp, 2006), it would not be a sensible means of detecting them at sea. ISWs can be time consuming and expensive to study in the field, not least because they are difficult to locate, but also given the scale of ISWs and the turbulent state of the ocean. Given that many field investigations already exist, and the difficulties mentioned, the detailed study of ISWs lends itself to laboratory experiments.

ISWs, at the oceanic scale, propagate typically at 8km/h with wavefronts of 100km and with wavelengths of up to 4km; they are usually found as rank-ordered packets, with the leading wave having the largest amplitude (Sutherland, 2010). They exist in stratified oceans and lakes. This stratification can be established through surface heating or cooling, from river outflow, ice melting or various other natural processes. The density stratification in many oceans and lakes can be described by one of the following stratifications; either (i) a three-layer stratification consisting of a homogeneous upper layer separated from a denser homogeneous lower layer by a relatively thin, linearly-stratified interface (pycnocline) with the upper layer usually much shallower than the lower layer (Michallet & Ivey, 1999) or (ii) a two-layer stratification consisting of a linearly-stratified upper layer on top of a homogenous lower layer, the upper layer is usually much shallower than the lower layer. For example, a two-layer stratification can be seen in Figure 1*(b)*, the location of the sample can be found in Figure 1*(a)*. An ISW observation taken at nearly the same position (Figure 1*(c)*) (but at a different time) shows a time series of isopycnals, the stratification could be defined as a three

layer stratification in this instance, although it can be seen that the lower layer is not quite homogenous.

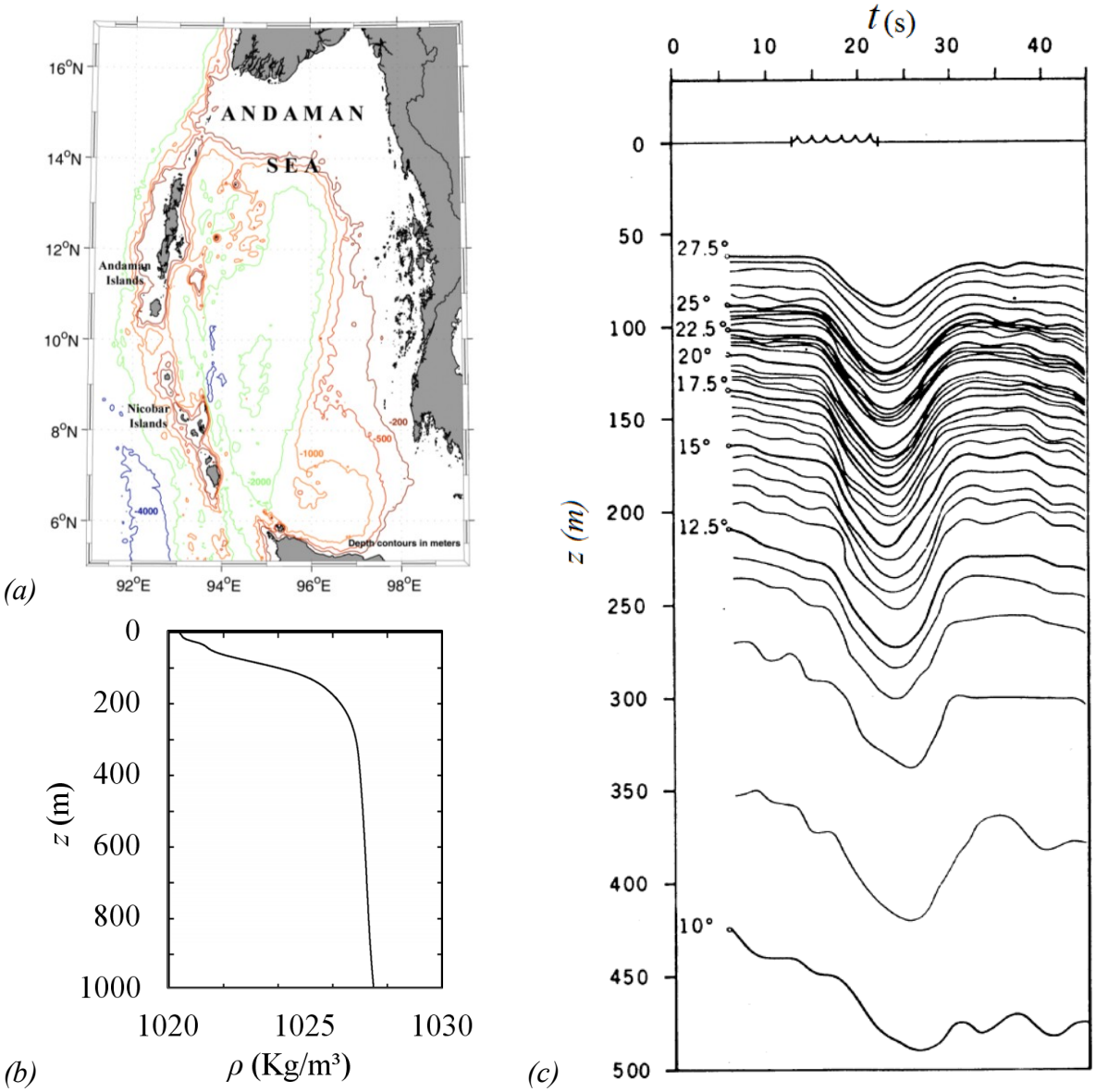

Figure 1 – (a) Bathymetry of the Andaman sea (Smith and Sandwell, 1997). (b) Density stratification at rest (Source: NODC Global Ocean Temperature and Salinity Profiles (June 1991)) Density profile derived from SD2 data collected on 1 February 1972 at 7.000N, 94.970E. (c) Thermal stratification as an ISW passes an XBT (eXpendable Bathy Thermograph) cast carried out on 25 October 1976 at 6°53′ N. and 97°04′ E (Osborne and Burch, 1980).

These stratifications will be referred to as two and three layer stratifications henceforth. ISWs may be waves of elevation or depression, unlike surface solitary waves which are always

waves of elevation. ISWs propagating in a two or three layer stratification will be of the depression type if the pycnocline occurs above the mid-height of the flow. That is, the pycnocline is deflected downward, away from the surface, by the propagating ISW. All the ISWs considered in this experimental study were of the depression type. Note that ISWs of elevation have also been observed (Klymak & Moum, 2003; Moum *et al.,* 2007) in the oceans (when the pycnocline is below the mean depth of the water column) but waves of depression are much more common.

1.4 Properties of ISWs

ISWs have some of the properties of surface solitary waves and internal interfacial waves covered so far. ISWs are nonlinear waves of constant speed and form where dispersion is balanced by nonlinearity as the wave propagates in a density stratified system. ISWs are considerably slower than surface solitary waves due to their smaller restoring force compared with the restoring force at the air-water free surface interface. ISWs can be of large amplitude relative to the water depth through which they propagate; this leads to them being highly nonlinear (Fructus *et al*., 2009). Unlike surface solitary waves, the amplitudes of large ISWs are constrained by the conjugate limit (Benjamin, 1966). The conjugate limit allows a proportion of the overall depth to be reserved for the return flow. This limit constrains waves to broaden rather than deepen beyond a certain amplitude, causing nonlinear behaviour which strengthens as the limit is approached. When ISWs are propagating in deep water the return flow necessary to maintain hydrostatic balance is small; conversely, in shallow water, the return flow is larger. For example, a stable ISW approaching a continental shelf in the ocean may become susceptible to shear instabilities as the depth into which it propagates reduces.

1.5 Breaking ISWs

There are several conditions that will lead to an ISW breaking. A change in polarity of the wave (Helfrich *et al*., 1984) occurring as a result of shoaling on shallow slopes. Overturning via steepening of the ISW (Lamb, 2002) on steeper slopes can also produce wave breaking. The dynamic balance can be disturbed through shoaling at a continental shelf or other bathymetric obstacle, leading to the violent breakdown of an ISW (Sveen *et al*., 2002; Aghsaee *et al*., 2010; Moum *et al*., 2003). The external environment can prompt the breakup of an ISW by upsetting the dynamic balance, causing an ISW to disperse into a wave train (Djordjevic & Redekopp, 1978). There are many other factors that could lead to a large scale destabilisation of an ISW such as variation in stratification, currents or surface forcing. None of these breaking mechanisms were considered in the present work. The experiments were conducted in a rectangular tank that had a flat horizontal bed, there was no surface forcing and no background currents and every effort was made to keep the stratification uniform along the tank's length. Therefore the remaining mechanisms for an ISW to break were of the flow instability type:

- In a three layer stratification the shear layer near/at the ISW peak is susceptible to shear instabilities such as the KH or H instabilities (Fructus *et al*., 2009). These instabilities cause the flow to roll up into billows. These billow saturate (i.e. reach their maximum vertical extent) when the effects of buoyancy (which tend to stabilise the flow) dominate over those of shear (which tend to destabilise). The billows then undergo transition to turbulence via buoyant secondary instabilities, such that some of the fluid entrained in the billows is mixed. This mixing raises the potential energy of the background stratification (Strang & Fernando, 2001a).

- In two layer stratifications, local fluid velocities in the front of the ISW can exceed the phase velocity of the ISW, causing convective instabilities. The small scale density inversions in the front of the ISW are advected downstream into billows which in turn grow and collapse (Carr *et al.*, 2008).

- For a two layer stratification, a large scale recirculation, referred to as a rotating core, within the ISW can cause density inversions within the wave (Lamb, 2002; Carr *et al*., 2012). The transition to this state is not well understood.

1.6 Applications/motivation

Breaking ISWs redistribute passive marine organisms that can function as biological tracers, apply undesirable forces to subsea structures and, not least, are an important sink of energy in the energy balance of oceanographic and weather prediction models. In the context of civil engineering one must know the external conditions to which a structure is subjected in order to design to a given standard; for example, a structure is to withstand a 1 in 100 year storm. In stratified oceans and lakes (e.g Andaman Sea, Sulu Sea, South China Sea, coastal Angola), ISWs contribute loadings to offshore exploration and production structures in their path. In such regions ISWs can attain significant amplitude (up to 60 - 150m in water depths of 200 – 350m, see Osborne and Burch, 1980; Duda *et al.,* 2004); consequently, they should be considered in the design loading when operating, building and decommissioning in such environments. Early warning systems have been developed for offshore installations to aid in the preparation for the arrival of ISWs (Goff & Jeans, 2010). In shallow seas, passing ISWs can entrain sediments which, in turn, can disrupt subsea communication. The settling of these disturbed sediments can bury plant if it has been stored or installed on the sea bed. Acoustic techniques that supply the oil and gas industry with bathymetry and geophysical data must be calibrated to cope with effects associated with the stratified water column. Problems arise

when the stratification rapidly changes or there is an increase in suspended sediment in the water column; for example, as a result of the passing of an ISW (Apel *et al.*, 1997).

The entrainment of the water columns into the core of ISWs contributes to the transport of pollutants/solutes/zooplankton and other biological tracers. The passing of breaking ISWs enhances the vertical mixing of the water column, making breaking ISWs of interest to any field that monitors or models the quantities mentioned. Large scale (geophysical) numerical models (weather prediction models, for example) must parameterise rather than simulate small scale phenomena such as the breaking of ISWs which cannot be resolved due to the grid spacing/computational overhead. Sub grid parameterisation of breaking ISWs so that they may be incorporated into these models would allow the small scale effects to be captured without simulating the physical process (Kershaw, 1995). Potentially, this can improve the energy balance in such models as breaking ISWs are thought to be a significant sink of energy in the open ocean.

1.7 Objectives

The primary objective was to study the breaking due to shear and convectional instability on ISWs. Potentially ISWs offered an excellent opportunity to make general observations on shear flows. KH billows have been studied extensively on horizontal shear flows in various experimental setups (Thorpe, 1971; Koop & Browand, 1979; Lawrence *et al*., 1991; De Silva *et al.*, 1996). The results of these experiments were complicated by the measurement of the velocity interfacial thickness (d_z) which was developing either temporally and/or spatially as the instabilities and billows were developing. ISWs are unique in that instabilities are repressed in the front of the ISW where the shear flow accelerates. At the ISW peak, in the frame of reference of the wave, where instabilities are not repressed, the longitudinal

variation in the vertical shear is relatively small compared with the longitudinal variation of shear on the limbs of the wave profile. The consequence of this is that instabilities at the ISW peak have relatively constant initial conditions compared to other experimental setups.

A laboratory investigation of breaking ISWs was undertaken to study the behaviour of the billows associated with breaking for two different configurations, namely a three layer stratification and a two layer stratification. To the authors knowledge this was the first investigation of this type. The objectives of the study were:

- To investigate and characterise the spatial and temporal development of the waves undergoing shear and/or convective instability
- To take novel measurements of the internal density structure of billows generated by shear instability to allow parameterisation of the billows.
- To investigate the entrainment and mixing that results from a passing ISW
- To attempt to generate the rotating core type ISW in a two layer stratification and to observe its evolution

2 Literature review

This study should be viewed in the overall context of previous work on the general characteristics and behaviour of instabilities, billows, ISWs and breaking ISWs. It has been necessary to review the previous work on the stability of stratified, horizontal shear flows as much of the study of KH and H billows has been focused both experimentally and numerically on such flows. Linear stability analysis and stability diagrams have been included to help the reader gain a deeper understanding of the mechanisms that lead to either KH or H billows forming. Consideration has been given to the effect of flow asymmetry on horizontal shear flows; this parameter can affect the type of instability that occurs and consequently the type of billow that is formed. Only a small amount of work regarding convective breaking and rotating core type ISWs exists; what exists has been reviewed. Lastly, entrainment, mixing and dissipation are discussed along with the energy balance in stratified flows. Key concepts are introduced as appropriate.

2.1 Internal solitary waves

The wave profiles predicted for non breaking solitary waves by the KdV equation and the finite depth equation (Joseph, 1977) were first tested against the wave profiles of experimental ISWs of small but finite amplitudes by Koop & Butler (1981) and then again by Segur & Hammack (1982). The finite depth equation, like the KdV equation, describes the evolution of an internal wave propagating in one direction with a small but finite amplitude, where the wave is long compared to the water depth. It is suitable for use with internal waves in an intermediate depth of water, whereas the KdV equation is suited to shallow water waves. Segur & Hammack (1982) found that the KdV equation outperformed the finite depth equation in terms of accuracy and range of validity. Kao *et al*. (1985) tested in the laboratory how well inverse scattering theory (see Alblowitz & Segur 1981; Whitham 1974) predicts the

number of ISWs generated by releasing varying volumes of water into a three layer stratification, using a gate arrangement to confine a prescribed volume of fluid prior to release. Inverse scattering theory allows linear methods to be applied to certain nonlinear problems; it provides the general solution to an initial value problem. Kao *et al*. (1985) found good agreement between the predicted and the actual number of ISWs produced from a given volume of water for ISWs of varying amplitudes including some ISWs that were quite large. This was surprising; typically the KdV equation does not predict the wave profile of large (i.e. highly nonlinear) ISWs accurately because it is a weakly nonlinear equation. For a three layer stratification in which the middle layer is thin, Grue *et al*. (1999) demonstrated that KdV theory produced acceptable results when $h_1/h_2<0.4$, when compared with experimental ISW profiles. Here h_1 is the depth of the upper layer, h_2 is the depth of the lower layer and the transitional layer was assumed to be vanishing thin. When $h_1/h_2>0.4$ it was found that KdV theory became an increasingly unreliable way to predict the ISW profile (see Figure 2*(a)*). A fully nonlinear interfacial model derived by Grue (Grue *et al*., 1997) showed good agreement with stable experimental ISWs when $h_1/h_2>0.4$.

Breaking due to shear in the rear of an ISW can significantly alter the profile of the ISW, as shown in Figure 2*(b)*. Note that the front of the ISW was unaffected by breaking and continued to be well predicted by the fully nonlinear interface model.

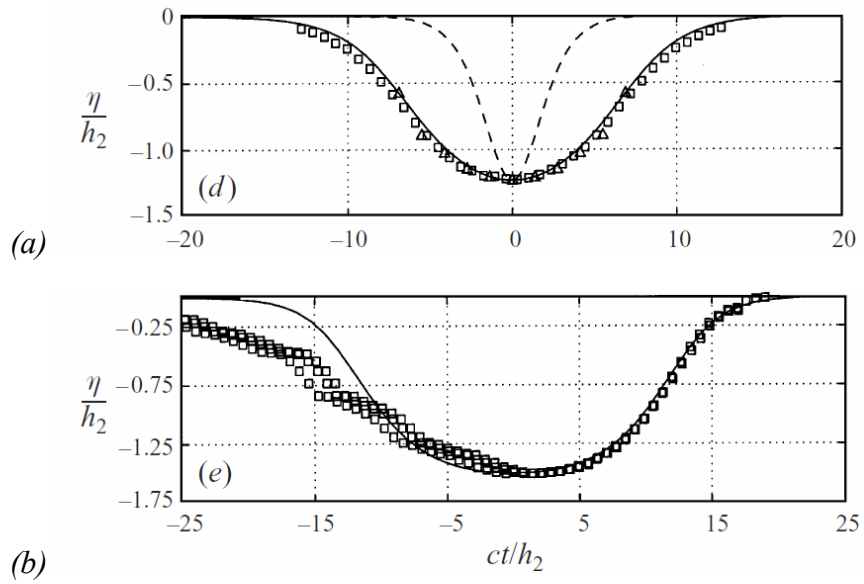

Figure 2 – Excerpt from Grue et al. (1999) showing the ISW profile η(ct) from a fixed position 10.5 m downstream. Squares: measured pycnocline, Solid line: fully nonlinear theory, dashed line: KdV theory. (a) a/h_2 = 1.23, stable ISW. (b) a/h_2 = 1.51, breaking ISW.

Michallet & Barthelemy (1998) found good agreement when comparing experimental ISWs in the range $0.4<h_1/h_2<0.6$ to the extended KdV (eKdV; Djordjevic & Redekopp 1978, Kakutani & Yamasaki 1978, Lee & Beardsley 1974). However, beyond $h_1/h_2>0.6$ agreement became increasingly poor.

As established in the introduction, large amplitude ISWs can be highly nonlinear. That is, the ISW amplitude does not scale linearly with the ISW celerity (Figure 3*(b)*). Furthermore, the ISW profile, the area it encompasses and, consequently, the potential energy of the ISW does not scale linearly with amplitude (Figure 3*(a)...(b)*, Figure 4*(a)...(b)*). It can be seen from Figure 3*(a)* that ISW profiles widen and flatten as the non-dimensional ISW amplitude (here denoted as z_n) approaches the conjugate limit (z_n=1, by definition). Small amplitude ISWs may exhibit a linear relationship between ISW celerity and amplitude if they are far from the conjugate limit. It can be seen in Figure 4*(b)* that progressively larger ISWs have diminishing gains in *KE* for increased amplitude as the conjugate limit is approached. ISWs in this study

have large amplitudes and as a consequence they are highly nonlinear; they are approaching the conjugate limit and therefore have a wave profile that shows significant flattening of the wave peak (see Fig 3*(a)*). Very large ISWs that are close to the conjugate limit eventually behave such that the fore and aft portions of the wave become increasingly decoupled as the amplitude is increased (Benjamin, 1966). It follows that the events that arise due to the ISW passing, such as turbulence, cannot be parameterised easily with ISW amplitude, celerity or energy.

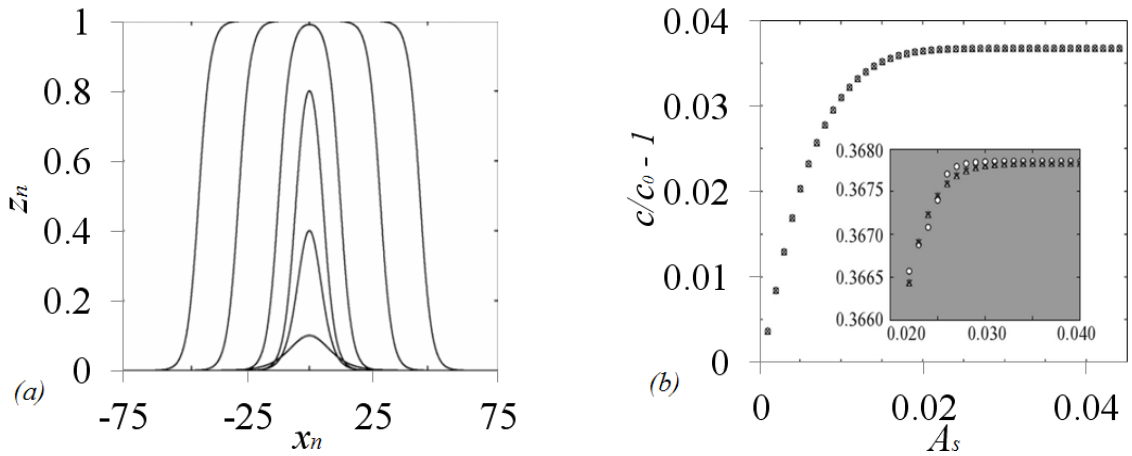

Figure 3 – (a) Successively larger KdV approximations to ISW profiles where z_n and x_n were non-dimensional vertical excursion and horizontal position respectively (Fochesato et al., 2005). (b) A special measure of non-dimensional amplitude (A_s) versus non-dimensional ISW celerity (c/c_0 - 1) (King et al., 2011).

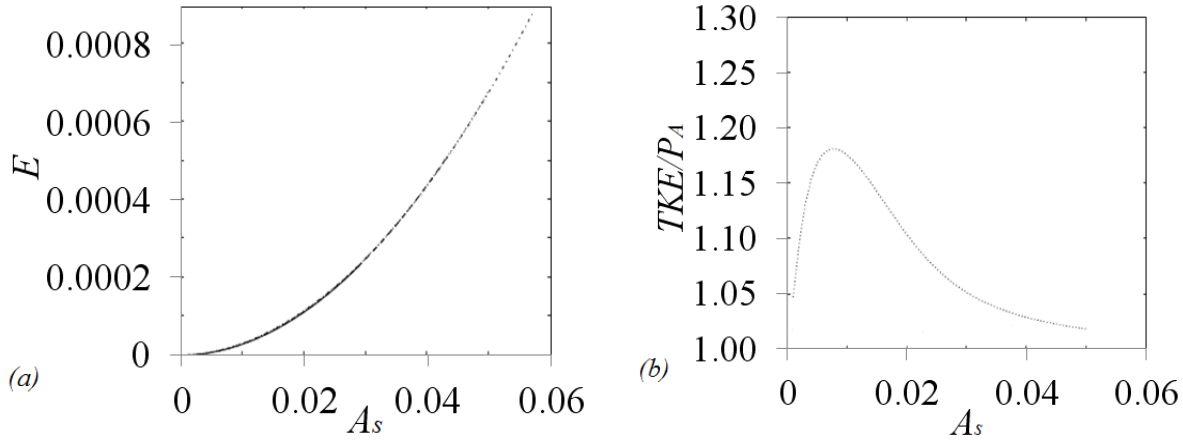

Figure 4 – (a) Non-dimensional Total Energy (E) vs. A_s (King et al., 2011). (b) Ratio of turbulent kinetic energy (TKE) to available potential energy (P_A) vs. A_s, (King et al., 2011).

2.2 Breaking ISWs

When certain criteria are fulfilled an ISW can break, resulting in energy being transferred to smaller scales than the scale of the ISW itself. In the context of the present work, there were three proposed mechanisms for breaking: shear breaking, convective breaking and the rotating core. Previous studies of these processes will be discussed in the following section. Note that convective breaking is particular to the two layer stratification (where a linearly-stratified upper layer lies above a homogeneous lower layer), whereas shear instabilities are universally applicable to shear flows.

2.2.1 *The gradient Richardson number*

Numerous authors (e.g Howard & Maslowe, 1974; Turner1979; Fernando, 1991) have used the gradient Richardson number (Ri_g) or similar as a convenient way to predict the onset of shear breaking in a horizontal stratified shear flow. The gradient Richardson number is a non-dimensional measure of the relative importance of stratification to velocity shear. A large value of Ri_g is typical of a flow dominated by stratification whereas a small value of Ri_g is typical of a flow where shear is dominating. Here, Ri_g is defined with regard to a Cartesian coordinate system (x,y,z) for two horizontal, miscible layers of density ρ_0 and $\rho_0+(\Delta\rho)$ respectively, as:

$$Ri_g = N^2 / (\partial U/\partial z)^2 \qquad \text{Equation 6}$$

Where: $\partial U/\partial z$ is the vertical shear in the horizontal velocity U and $N=[(g/\rho_0)(\partial\rho/\partial z)]^{1/2}$ is the buoyancy frequency characterising the stratified system, for which: $\partial\rho/\partial z$ is the vertical gradient of density and ρ_0 is a reference density. The buoyancy frequency can be approximated by $N^2 \approx g'/H_2$ where: g' $(g'=g(\Delta\rho)/\rho_0)$ is the reduced gravitational acceleration for which: $\Delta\rho$ is the change in density.

Linear stability analysis of a two-dimensional shear flow has been used to demonstrate that a critical Richardson number (Ri_c) defines a stability transition below which small perturbations in the flow are able to overcome the suppressing effects of stratification (Taylor, 1931; Miles, 1961; Howard 1961). The value of Ri_c for two-dimensional linear instability has often been given as $Ri_c \leq 0.25$ (Taylor, 1931; Miles, 1961; Howard 1961). This happens to be true for a specific set of conditions and only if H instabilities are ignored (Holmboe, 1962), as discussed later.

2.3 Stability of a shear flow

The conditions required for shear instabilities to form, on large amplitude ISWs in a three layer system, were investigated theoretically and experimentally by Fructus *et al*. (2009). Fructus *et al.* reported that large amplitude ISWs with $Ri_g \leq 0.25$ can be stable and proposed that the breaking threshold $L_x/\lambda_B > 0.86$ (where L_x is the horizontal length of the pocket of instability and λ_B is the billow wavelength) was a more appropriate criterion for breaking compared with $Ri_c \leq 0.25$. This was a sensible extra criterion which essentially meant that there must be a sufficient length available for an instability to develop. Barad & Fringer (2010), investigating breaking ISWs numerically in a three layer system, acknowledged the condition $L_x/\lambda_B > 0.86$ and presented a time-equivalent criterion $\sigma_i T_w > 5$, where σ_i was the average growth rate of an instability in the pocket where $Ri_g < 0.25$ and T_w was the time in which parcels of fluid were subjected to $Ri_g < 0.25$. This was another sensible criterion, requiring that there was sufficient time for an instability to grow. Barad & Fringer (2010) added a further criterion $Ri_c < 0.1 \pm 0.01$, described as being more attractive because of its ease of use. However it was misleading, as it was not based on any physical mechanism.

Troy & Kosseff (2005) examined shear breaking on progressive, periodic, lowest mode internal waves in the laboratory. They described the subsequent breaking on the pycnocline as closely resembling KH billows. However, if they had examined the density profiles through the billows they may have concluded that they actually had evidence of asymmetric Holmboe billows, which are visually difficult to distinguish from KH billows (Carpenter *et al.*, 2007). The growth of the instabilities and the subsequent billows was strongly modified by rapidly varying shear which was at a maximum in the wave peaks and troughs. It was suggested that the time scale for billow growth could be limited by the wave period when considering these periodic linear internal waves. This aspect was previously hypothesized by Thorpe (1968).

It has been demonstrated numerically that the front of an ISW filters out perturbations through stretching and filamentation of small amplitude wave packets (Camassa, 2012). It was thought that this was the mechanism which prevents KH and H billows from forming on the front of the ISWs. The shear environment on a breaking ISW varies temporally and spatially; intuitively an ISW should then alter the shear-induced breaking somehow, when compared with a parallel stratified shear flow. However, if the behaviour of the billows is not altered and a satisfactory correspondence between billows on a horizontal shear flow and billows on an ISW is found, the ISW offers a unique setting in which to study the general evolution of KH or H billows. The horizontal variation of shear at or near the peak of an ISW is relatively small, therefore the initial conditions of KH or H billows that forms on or near the ISW peak are relatively constant. This is not the case in the tilt tank type experiments (Thorpe, 1968, 1971, 1973), in which the parallel shear flow was slowly varying, and in the wave maker type experiments (Troy & Koseff, 2005) where the shear was rapidly varying. Furthermore, it was difficult to vary the scale ratio (R; shown in Figure 5) in the afore-

mentioned experiments (Personal communication: Ivey, 2013) whereas varying R in the ISW experiments was simply achieved by increasing the amplitude of the ISW.

2.4 Shear breaking in horizontal flows

Early horizontal shear flow experiments were conducted in 1883 by Reynolds (Jackson & Launder, 2007) who, using immiscible fluids, tried to identify a critical velocity at which instability would occur. Studies similar to this, using immiscible and miscible fluids, were conducted by Mittendorf (1961) and, more notably, Thorpe (1968), who described the technique used by Reynolds and qualitatively described the instabilities and the subsequent billows that arose due to the flow. Unlike immiscible flows, miscible flows, such as those in the ocean, often have pycnoclines in the same order of thickness as the velocity interface thickness; these are the types of stratification that have been considered in this document. Mittendorf (1961) was able to show that the KH billow locally reduced shear which could lead to a state of marginal stability. Turner (1979) speculated, with reference to Mittendorf (1961), that a gravity driven flow would accelerate to a point where instabilities and billows form, which, in turn, would increase drag, thereby slowing the flow. Subsequently, the flow would then accelerate again when the instabilities had died down. The control of the mean flow in this manner, near a state of turbulence, is referred to as marginal stability. Thorpe (1971) conducted more experiments, this time in a larger and better instrumented tank comparing wavelength, flow conditions and vertical growth rate to theoretical values from the Taylor-Goldstein equation (Taylor, 1931; Goldstein, 1931; Miles, 1961, Drazin & Howard, 1966). Good qualitative agreement was obtained but quantitative differences were significant; this was attributed to the amplitude of an instability at the point in its growth where measurements were possible. That is, as soon as instability could be seen, it was already beyond the applicable range of the Taylor-Goldstein equation, which assumes infinitesimal disturbances (Hazel 1972). Thorpe (1971) also made some observations of

finite amplitude instabilities or billows. He showed that the instability wavelength was proportional to the theoretical density interface length scale. This length scale was used in place of the actual density interface thickness due to the difficultly in measuring the interface. It was also noted that once the instability or billow reached finite amplitude it had a remarkably linear growth rate (linear stability analysis predicts an exponential growth rate for the instability).

The structure of the billows that resulted from KH instabilities were investigated again by Thorpe (1973) who found, using conductivity sensors, that the final state of a billow was dependent on its initial conditions for billows with an amplitude (a) to wavelength (λ_B) ratio ($s=a/\lambda_B$) in the range $0.05>s>0.5$. In this study, the range $0.5>s>0.9$ was investigated for KH billows. Thorpe was able to estimate the gain in background potential energy (P_B) to the stratification and the loss of *KE* to the mean flow per unit cross sectional area and, in doing so, could estimate the energy lost to dissipation in heat and internal wave motion. Thorpe (1987) gave the mixing efficiency of the billow (*PE* gain / *KE* loss) as about 0.25 when the gradient Richardson Number was small. The mixing efficiency decreased as the critical Richardson Number was approached. Thorpe's data (1968; 1971; 1973) although valuable to the early study of KH billows was later found to be contaminated with side wall effects due to the width of the channel used (Gregg, 1987).

Koop & Browand (1979) investigated stratified turbulence with a novel re-circulating horizontal shear flow, which allowed a longer window of reliable sampling compared to the tilt tank experiments of Thorpe. The development of the KH billows to a first and second pairing was normally observed. It was found that the thickness of the velocity interface (d_z;

see Figure 5) set the vertical scale of the billow. Where previous studies (Thorpe, 1973) had considered regimes where $R \approx 1$ (see Figure 5) and asymmetry $a_s \approx 0$ (see Figure 8), Koop & Browand were able to reach small scale ratios ($R<1$) in asymmetric flows ($a_s \neq 0$), which was shown to have an important effect on the billows. It was found that scaling the vertical growth of billows with d_z collapsed the various billows and the normalised quantity appeared to be independent of Reynolds number ($200<Re<1450$) and that λ_B was linearly proportional to d_z. Billows appeared to reach their maximum vertical extent or saturation point at vertical billow amplitude (L_b) $L_b/d_z \approx 4.5 \pm 0.5$ in a non-dimensional time ($t\, g'/\Delta U \approx 7$). Experimentally Thorpe (1973) found the time to saturation to be $tg'/\Delta U \approx 6$. In the numerical study of Corcos & Sherman (1976) the time till saturation was found to be $tg'/\Delta U \approx 4.5$, where ΔU was the horizontal velocity difference (see Figure 13).

De Silva *et al*. (1996), by comparing laboratory, numerical and field data, demonstrated for cases of parallel, stratified, shear flows that billows of different scales were self-similar when scaled with their instability wavelength. It was shown that the time required for complete billow growth was $\Delta U t/\lambda_B \approx 5$ and that, up to that time, the Thorpe length scale (described in section 5) was relatively constant when measured vertically within the middle quarter of the billow.

It has been demonstrated numerically (Smyth & Winters, 2003) that the ratio of the density interface thickness and the velocity interface thickness, referred to as the scale ratio R ($R=d_z/H_2$; see Figure 5), was a critical parameter when analysing stratified horizontal shear flows. Figure 5 shows in sketch form $U(z)$, the vertical variation of the horizontal velocity component of the flow with depth and $\rho(z)$, the vertical variation of density with depth.

When the critical Richardson Number (Ri_c) for stability was derived by Miles (1961) and Howard (1961) the scale ratio was fixed to unity (R=1). Deviation from R=1 will affect the stability of the flow to small perturbations and consequently the value of Ri_c, as shown in the following section.

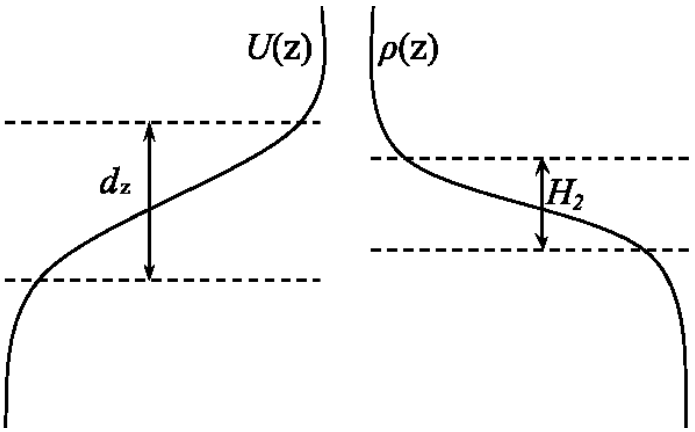

Figure 5 – In sketch form U(z), the vertical variation of the horizontal velocity component of the flow with depth and ρ(z), the vertical variation of density with depth. to illustrate the scale ratio R ($R=d_z/h_2$)

Several authors (Holmboe, 1962; Baines & Mitsudera, 1994; Caulfield, 1994; Smyth & Winters, 2003; Carpenter *et al*., 2010) argue that there is a limiting value of R which determines the type of instability that arises from the flow (Figure 6). Smyth & Winters (2003) suggested that turbulent regimes where R>2.4 would give rise to H instabilities instead of KH instabilities that were found at lower R values. This was a simplification, in a linear stability diagram, if R increases, the pocket where a KH instability would occur shrinks. When this pocket is sufficiently small (say at R=2.4), a very small Richardson number is required to cause a KH instability, very small Richardson numbers are unlikely to ever occur in nature because an unusually steep velocity gradient would be required. This can be seen in Figure 6*(a)* (where R>>1), the critical Richardson Number had dropped from the expected value Ri_c<0.25 (when R=1) to a lower value Ri_c<0.05. The condition R=1 may be common in nature therefore the instability criterion Ri_c<0.25 offers a good approximate

value for stability if little is known about the flow. Figure 6*(b)* shows that a background stratification can be established to give an effectively infinite *R* value, removing the pocket where KH instabilities exist. In such stratifications only Holmboe H instabilities will grow.

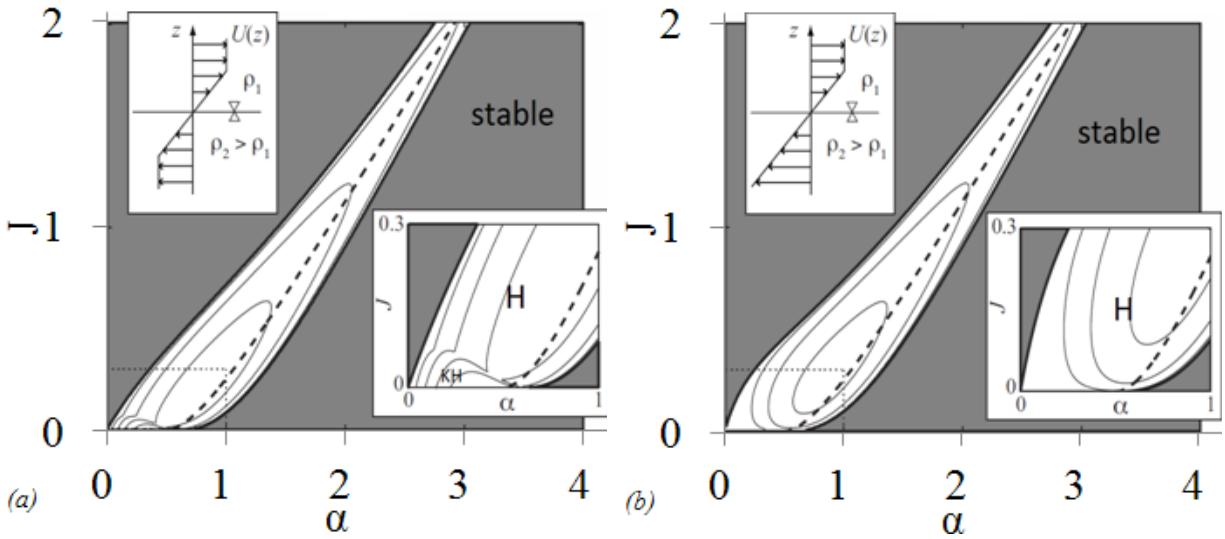

Figure 6 – Excerpt from Carpenter et al. (2010) showing stability diagrams. Ri_B (here labelled J), versus the instability growth rate (contours) versus the instability wave number (α), grey areas are stable (reproduced from Baines & Mitsudera, 1994) (a) The inset shear profiles shows a large R value (b) The inset shear profiles shows an infinite R value.

Following the experimental work by Thorpe (1973), the time evolution of the velocity field of KH billows was numerically (Patnaik *et al*., 1976) and analytically (Corcos & Sherman, 1976) investigated. It was found that, at billow saturation, nearly all the fluid in the stratified shear layer had moved into the core. This resulted in stretching of the braid region between billows. Growth was self limiting because of a finite supply of vorticity in one wavelength. At small amplitude linear stability was in good agreement with the simulations when considering the growth rate and wavelength of instabilities. The state at which a billow achieves maximum amplitude was not in equilibrium; billows were found to overshoot the equilibrium state followed by damped oscillations. In real shear flows the fastest growing instability will always be dominant (for a fixed value of Ri_B, R and a_s). Klaassen & Peltier (1985a) were able to study the evolution of the KH billow numerically, for a longer non-

dimensional time and at a higher Reynolds number than was previously possible ($300<Re<900$). They found that KH billows produced, at these higher Reynolds numbers, were less sensitivity to the amplitude and structure of the initial disturbance when compared to the billow of Patnaik *et al*. (1976).

The Reynolds number *Re* is a ratio of inertial forces to viscous forces, its value is useful for determining flow regimes. The transitional Reynolds number Re_{trans} is an approximate value at which a regime change from viscously-dominated flow, to an inertially-dominated flow would be expected. Here,

$$Re = v\, L_R / \upsilon \qquad \text{Equation 7}$$

where: v is the mean velocity, in the case of a shear flow the velocity difference (ΔU) of the free streams may be appropriate. L_R is a length scale associated with the flow, in this case the width of the velocity interfacial thickness (d_z) and υ is the kinematic viscosity of the fluid (Koop & Browand, 1979). Several authors (Peltier *et al*., 1978; Davis & Peltier, 1979) have found that KH billows with Re<<500 are dominated by diffusive processes. The maximum vertical height of a KH billow was shown to increase rapidly with Reynolds number $300<Re<500$ and at a decreasing rate in the range $500<Re<900$ (Peltier *et al*., 1978; Davis & Peltier, 1979). It was estimated that the effect of Reynolds number would be absent with Re>1000 (in this study $Re>3000$). Klaassen & Peltier (1985b) investigated the effect of Prandtl number (*Pr*) on the KH billow, where *Pr* is a dimensionless ratio of the rate of viscous diffusivity (momentum diffusivity) to thermal diffusivity.

$$Pr = \upsilon / \kappa \qquad \text{Equation 8}$$

where κ is the thermal diffusion rate. A low value of Pr (Pr<1) is typical of a gas and a high Pr (Pr>1) is typical of a more viscous fluid e.g. water (Pr≈7). Values of Pr in the laboratory and ocean/lake are similar.

During the study of mixing layers in gases (Brown & Roshko, 1974), three dimensional motions were observed that appeared as small scale streamwise streaks in the wake of the two dimensional motion of the KH billows. These features were also found at lower Reynolds numbers in water (Breidenthal, 1981). This prompted the study of secondary instabilities as a mechanism for the transition from two dimensional motions to turbulence (Bernal & Roshko 1986). Klaassen & Peltier (1991) numerically investigated the initial instabilities that follow the roll up of a KH billow and the effect of stratification on those secondary instabilities. It was found that two instabilities occur, even in the presence of stratification, which may lead the KH billow from the ordered periodic state to one of turbulence. As computing power increased it became possible to numerically model the transition to turbulence in three dimensions giving a much clearer picture of the secondary instabilities and the mixing transition (Caulfield & Peltier, 2000). Caulfield & Peltier (2000) demonstrated that the localised convective instabilities around the eye of the billow, that form once the KH billow reaches saturation, grow in the streamwise direction and collide/attach with streamwise vortices from adjacent billows. It was the colliding of the vortex streaks that led to the violent transition to turbulence. Peltier & Caulfield (2003) offer a thorough review of stratified shear flow mixing in which they remark that, under certain conditions, (high Reynolds Number and low Bulk Richardson Number) mixing will be dominated by the convective collapse of the KH billow rather than the secondary instabilities in the braid.

2.5 Mechanism for KH instability

The growth of KH instabilities may be understood conveniently in terms of the interaction of two independently-propagating velocity perturbations travelling in opposite directions along a thin transitional layer (Figure 7*(a)*). Dominant wave number perturbations 'phase lock' and cause mutual growth in one another (Figure 7*(b)*). The phase locking of perturbations concentrates vorticity in the thin transitional layer which results in the amplification of the instability. Further amplification results from the pressure distribution across the instability; pressure in the concave part of the instability is greater than that over the convex part of the instability. The eventual overturning of the wave formed by the growth of the instability is recognised as the classic KH billow (Figure 7*(c)*) (Thorpe, 1971). The KH instability forms independently of the density field, forming in homogenous or stratified density fields. The criterion $R < 2.4$ needs to be fulfilled for KH overturning according to Smyth & Winters (2003); in essence, this means that the oppositely-propagating perturbations must be close enough to interact.

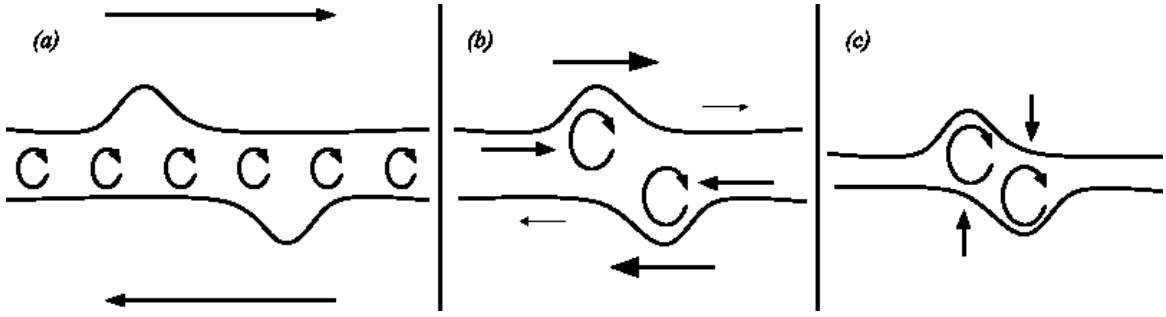

Figure 7 – Schematic of the mechanism that brings about the Kelvin Helmholtz instability.

2.6 Mechanisms for H instability

Unlike the KH instability, the H instability required a stratified density field allowing waves to form, in addition to perturbations in the vorticity field. If the thin transition layer described in the previous section (see Fig 5) increased in thickness beyond R =2.4 or thereabouts, the velocity perturbations that cause a KH instability cannot phase lock, they are too far apart

(assuming Ri_g was not very small). Another way to think about it was that if R increased (if d_z was fixed), H_2 must decrease, consequently the stratification would increase (N^2 increased with decreasing H_2), such that, at a certain level, the stratification (Ri_g increases with increasing N^2, assuming $\partial U/\partial z$ is fixed) would be able to suppress KH instabilities and allow the development of H instabilities. It has been proposed by several authors (Holmboe, 1962; Baines & Mitsudera, 1994; Caulfield, 1994; Smyth & Winters, 2003; Carpenter *et al*., 2010) that the dominant vorticity perturbation phase locks with a perturbation in the density field when another vorticity interface is not available. Baines & Mitsudera (1994) clearly demonstrated that this was possible by only permitting one density and one vorticity interface in their model (see Figure 6*(b)*).

2.7 Convective breaking

Convective breaking has been observed experimentally on ISWs in a 2 layer regime (Carr *et al*., 2008) and investigated numerically (Helfrich & White, 2010). The breaking was characterised by local fluid velocities in the front of the ISW exceeding the wave phase speed, resulting in small scale mixing. Conceptually, this process is described well in Liu *et al*. (2010). In essence, the disparity in the velocities results in the distortion of isopycnals (surfaces that represents constant density) to the point where there is a density inversion. The mixing in the front of the wave appeared to make the ISW more prone to breaking via KH instabilities downstream of the small scale convective instabilities. Convective breaking does not occur in 3 layer regimes (Carr *et al*., 2008; Fructus *et al*., 2009); why the 3 layer regime suppresses convective breaking remains an open question.

2.8 Core behaviour

The term ‘rotating core’ has been used to describe an ISW in a two layer or continuous stratification in which a trapped volume of fluid was rotating within the ISW. The rotation of

the core can cause instability when isopycnals, distorted by the core or within the core are inverted, thereby causing the density profile to become statically unstable. ISWs with rotating cores can be created via shoaling of the ISWs over bathymetric obstacles (Lamb, 2002) or along a low angled slope (Lien *et al*., 2012) in a two layer or continuous stratification. Lamb (2002) demonstrated numerically that any mixed layer at the surface, however thin, will significantly alter the behaviour of an ISW, preventing the formation of a rotating core. Lamb (2002) stated that the rotating core type ISW was likely to be rare under most oceanic conditions as having a monotonic stratification to the surface was unlikely in the presence of surface stress (wind). It was pointed out that most oceanic vertical density and velocity observations are recorded from the first 0.5m downward, and to understand the rotating core type ISW it was critical to know what was happening in the first 0.5m. Although the conditions for a trapped core ISW are rare, trapped rotating cores have been observed in the field (Lien *et al*., 2012). Lien *et al*. observed a rotating core type ISW developing over bathymetric features from a steady state ISW, leading to a core that mixed continually with the surrounding water leaving a wake of mixed fluid. Rotating cores can be initiated without the help of bathymetry (Helfrich & White, 2010), where convective instabilities initially destabilise an ISW which then evolves to a rotating core or, by the ISW encountering a density perturbation that acts in the same manner as the convective instability (Preusse *et al*., 2012). Scotti & Pineda (2004) suggested that the elevation type, near-bed, trapped core ISW was an important factor in across-shore transportation of plankton and contaminants. Diamessis & Redekopp (2006) suggested that the elevation type, near-bed, trapped core ISW may also carry sewage from outfalls back inshore and contribute to near-shore sediment transport. Recent numerical experiments (Carr *et al*., 2012) have shown that ISWs propagating in a 2 layer system can have at least two types of core. The first has a

homogenous non-rotational core which moves with the wave celerity *c*. The second has an unstable stratified core that rotates about the centre of the core.

2.9 Asymmetric shear flows

The vertical distance ($a_s=z_2-z_1$) between the centre of the velocity profile interface and the centre of the density profile interface is considered a measure of asymmetry (a_s) (Lawrence 1991; Carpenter *et al*., 2007). Figure 8 shows a_s in sketch form where: *U(z)* is the vertical variation of the horizontal velocity component of the flow with depth and *ρ(z),* the vertical variation of density with depth. A KH billow that forms in a symmetrical (a_s=0) flow will be stationary and a KH billow that forms in an asymmetric flow will propagate with the velocity of the background flow at the billow's position (personal communication: Lawrence & Carpenter, 2012). This is contrary to the conclusion of Fructus *et al*. (2009) who suggest, based on a small number of experiments, that the billow speed is a constant proportion of the wave speed.

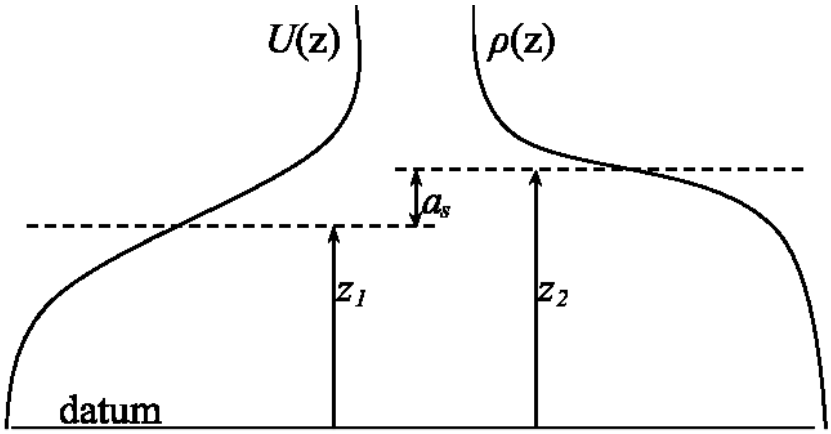

Figure 8 – Sketch defining asymmetry a_s as the difference in elevation of the mid-points of the undisturbed velocity U(z) and density ρ(z) profiles in a stratified shear flow .

A Holmboe (H) instability in a symmetric flow results in the formation of two billows propagating in opposite directions, whereas a Holmboe instability in an asymmetric flow (AH) generates a single billow that propagates with the velocity of the background flow at

the billow's position. This was well documented by Carpenter *et al*., (2007; 2010; 2013). To attain a symmetric flow, in the context of an ISW, the return flow under the ISW must match the ISW speed. This is an unlikely scenario in practice so it is reasonable to expect billows to be asymmetric most of the time. No stationary billows were observed in the experiments reported in this thesis.

Haigh & Lawrence (1999) used linear stability analysis to study the effect of asymmetry on H instabilities and to review the results from Holmboe (1962). They found, for the symmetric case, that the H instability has two oppositely-propagating modes which have the same growth rate and wavelength. It was also clear that, in the presence of asymmetry, one of the two modes is always faster, leading to a single mode presenting in simulations and experiments (Carpenter *et al*., 2007). Extending the work of Lawrence *et al*. (1991), where the vertical domain of the stability analysis was bounded, it was found that growth rates were noticeably affected when the domain was less than 5 times the shear layer thickness. Effects of the boundaries were negligible when the domain was 10 times the shear layer thickness or greater. The assumption that instabilities were initially 2D was found to be true past this limit. Lawrence *et al*. (1991) set out to produce the symmetric Holmboe instability in the laboratory but found this difficult because of the initial profile asymmetry in their experiments. For the AH instabilities they found good agreement with the wavelength predicted by linear stability analysis.

Carpenter *et al*. (2007) demonstrated, with direct numerical simulation, that an AH billow had an appearance that was very similar to that of a KH billow, as shown in Figure 9. It was

noted that the AH billow did not overturn the central isopycnal. In Figure 9 it can be seen that none of the lower density fluid is present in the arm of the billow.

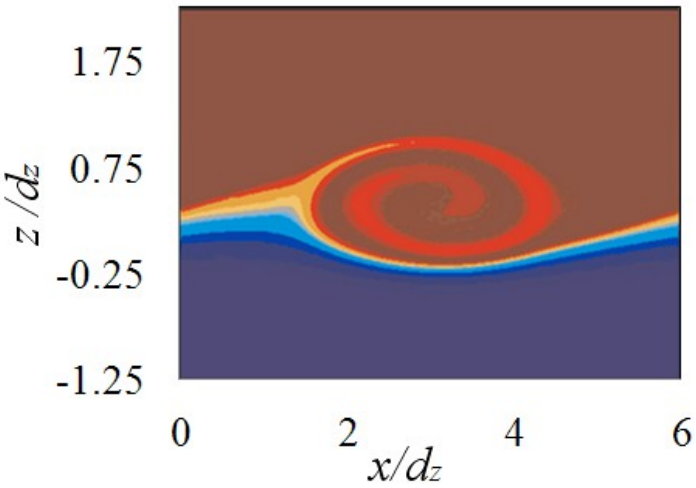

Figure 9 – Excerpt from Carpenter et al. (2007) showing DNS of a Holmboe billow growing in a strongly asymmetric (a_s=0.5) flow where the velocity interface is much thicker than the density interface (R=3) and Ri=0.15. The velocity interfacial thickness was denoted as h_0.

2.10 Entrainment, mixing and dissipation

Attempts to characterise entrainment and mixing in shear layers initially focused on the mixing efficiency of near symmetric KH billows (Thorpe, 1973), where the mixing efficiency or flux coefficient (Γ) was defined as the ratio of vertical buoyancy flux ($B=P_A+P_B$) to turbulent kinetic energy (*TKE*) dissipation (ϵ), $\Gamma = B/\epsilon$, where P_A was the flux of available potential energy (*PE*) and P_B was the flux of background PE. Thorpe's experimental investigation found that, at saturation, when a KH billow collapsed, 15-25% of the *PE* extracted from the mean flow by the billow was used to increase the background *PE*. What proportion of the *TKE* that was converted into internal waves and *PE* was unknown (Fernando, 1991). Strang & Fernando (2001a; 2001b) were able to show that very little energy was lost to radiating internal waves by considering the energy balance of local production of *TKE* (P) to B and ϵ (P / ($B+\epsilon$) ≈ 1), finding that the balance rarely deviated from unity by more than the error in the measurements. Koop & Browand (1979)

demonstrated experimentally that the effects of a_s and R on a shear flow significantly complicated matters, compared to the earlier near symmetric experiments of Thorpe. They also found that given a larger window of observation billow pairing was more likely. Both Thorpe and Koop & Browand found that the Richardson number was an important factor when characterising the behaviour of stratified turbulence. Patterson *et al*. (2006) found experimentally that (i) the amount of mixing was strongly dependent on the time evolution of the KH billows in the flow and (ii) the mixing transition could be triggered by the pairing of billows or by the onset of secondary instabilities. It was shown that virtually no mixing took place before the billows were saturated. Their results (only 2 experiments) broadly agreed with Thorpe's estimate for mixing. De Silva *et al*. (1996) found, with good experimental data but a limited number of experiments, that the braid region (the stretched pycnocline between billows) did not make a significant contribution to mixing through the secondary instability. Schowalter *et al*., (1994) demonstrated experimentally and numerically that streamwise vortex tubes in the braid were more prevalent in non stratified shear layers as buoyancy acts to weaken the vortices in stratified flows.

Rather than study the structure of turbulence it can be advantageous to focus on the time- or spatially-averaged motions of the flow. Solving the Navier-Stokes equations numerically requires the smallest scales of turbulence to be resolved (Tennekes & Lumley, 1972), leading to a very fine mesh and a large number of calculations, even over a relatively small domain. To reduce the number of calculations required, so that larger domains can be studied, it is desirable to model the small scale turbulence. In 1895 Reynolds (Miles, 1981) decomposed the velocity field into time averaged motions and turbulent fluctuations which led to the Reynolds Averaged Navier-Stokes (RANS) equations. A component of the RANS equations is the Reynolds stresses (τ) which requires modelling to achieve closure of the RANS

equations. Eddy viscosity or turbulent viscosity (K_m) models have been used to try and determine the value of Reynolds stress since Boussinesq first attempted to do so (Boussinesq, 1887). The concept was extended by Prandtl in 1925 (Miles, 1981) with his mixing length concept. A more modern and widely adopted model is the K-epsilon (K-ε) model (Launder & Spalding, 1974). For the case of an incompressible two-dimensional shear flow the vertical Reynolds stress can be written as (Thorpe, 2007):

$$\tau/\rho_0 \approx -\langle u'w' \rangle = K_m (\partial U/\partial z) = P/S^2 (\partial U/\partial z) \qquad \text{Equation 9}$$

where u' and w' are the turbulent fluctuations (from the mean values) of the velocity components in the x and z directions, P is the production of TKE in the shear layer, S is the shear and $\langle\ \rangle$ denotes averaging. Eddy viscosity models often perform badly or require tuning when compared to DNS. This is due to the models treating turbulence as a property of the fluid (Tennekes & Lumley, 1972) effectively discarding any understanding of the turbulence, which is a property of the flow not of the fluid.

The problem when trying to capture the vertical mixing in one term can be illustrated by Carpenter *et al*. (2007) who found that, since asymmetric Holmboe instabilities do not overturn the central isopycnal and symmetric and asymmetric Homboe instabilities produce 2 and 1 billows respectively, mixing rates were highly dependent on the asymmetry of the flow. Furthermore, depending on the parameter R, discussed previously, a shear flow may produce turbulence in the form of KH or H billows. The mixing per billow was investigated numerically by Smyth & Winters (2003) using three dimensional DNS. They showed that ϵ and the mixing rate (M) were maintained at a higher rate for longer in the symmetric H billow, when compared to the KH billow.

The length scale at which the conversion of *TKE* to heat takes place is known as the Kolmogorov length scale (L_k) which, assuming stationary, isotropic, homogeneous turbulence (i.e. $TKE \approx \epsilon$), can be expressed as:

$$L_k \propto \upsilon^{3/4} / \epsilon^{1/4} \qquad \text{Equation 10}$$

where υ is the kinematic viscosity of the fluid. Using dimensional arguments, ϵ can be related to the large scale motions of the flow (in this case, the maximum vertical amplitude of a billow (L_{max})). It has been shown (numerically) by several authors that stratified turbulence can be invariant (statistically speaking) with respect to translation in time, space and rotation (Holt *et al*., 1992; Itsweire *et al*., 1993).

$$\epsilon \approx (\Delta U)^3 / L_{max} \qquad \text{Equation 11}$$

If a billow scaling for L_{max} could be found, ϵ could be estimated using Equation 11. However, it will be shown that different values for L_{max} exist for KH, H and AH billow. Furthermore the assumption that $TKE \approx \epsilon$ is not valid for stratified flows. TKE is also used to raise the background *PE* (P_B) in stratified flow so that $TKE \approx \epsilon + P_B$. An alternative approach to estimating ϵ utilised the Ozmidov length scale (L_o):

$$L_o = \epsilon^{1/2} / N^{3/2} \qquad \text{Equation 12}$$

where N is the buoyancy frequency (see section 3.4). L_o provides an estimate of the largest eddies that can be support by a stratified flow (Thorpe, 2007). L_o can be related to the Thorpe scale, L_T, (Thorpe, 1977; Thorpe, 2007) by:

$$L_o = \alpha_T L_T \qquad \text{Equation 13}$$

where α_T is a constant ranging from 0.65 (Itsweire, 1984) to 0.95 (Ferron *et al*., 1998). Dillon took field measurements of L_o and L_T in the seasonal oceanic thermocline (a location relevant to this study) and found α_T=0.79±0.4. Given Equation 12 and Equation 13, ϵ can be recast as follows:

$$\epsilon = \alpha_T L_T^2 N^3 \qquad \text{Equation 14}$$

Osborn (1980), making the marginal stability assumption, related the upper bound of vertical eddy viscosity of mass (K_ρ) to ϵ:

$$k_\rho < (\Gamma \epsilon) / N^2 \qquad \text{Equation 15}$$

$$K_\rho = -\langle b'w' \rangle / N^2 = B / N^2 \qquad \text{Equation 16}$$

The production of *TKE* in the shear layer (P) is balanced in the stratified case by ϵ and buoyancy flux ($P \approx B+\epsilon$), B is a product of the available (P_A) and background (P_B) potential energy and $B \approx P_A+P_B$ (Strang & Fernando, 2001b). The flux coefficient, mixing efficiency or sometimes, flux Richardson number (Γ or Ri_f) is often taken to be 0.2, although it is known to fluctuate (Moum *et al*., 1989; Strang & Fernando, 2001b; Carpenter *et al*., 2007). Osborn (1980) arrived at $\Gamma \approx 0.2$ by assuming that a general critical Richardson number existed for marginal stability. An initially stable shear flow exhibiting marginal stability will have a gradient Richardson Number that reduces until the shear flow breaks. The breaking will raise the gradient Richardson Number and restores stability. The process is repeated. Linear stability analysis has demonstrated that a general critical Richardson number does not exists. The three dimensional numerical simulations of Peltier & Caulfield (2003) showed that, although the instantaneous mixing efficiency varied while the two dimensional KH billow rolls up, the amount of mixing was small (as was the dissipation ϵ). When the two dimensional billow reached saturation, three dimensional convective instabilities were shown to trigger streamwise vortices and the impact/joining of these vortices between adjacent billows triggered the mixing transition. When the mixing transition occurred and the amount of mixing increased, the instantaneous mixing efficiency settled to Osborn's value of $\Gamma \approx 0.2$.

The ability of Equation 15 to correctly predict k_ρ was tested by Strang & Fernando (2001a) against a direct measurement ($K_\rho = B/N^2$). Osborn's (1980) method performed badly, with deviations from the measured value of up to 150%. Estimating Γ using the Richardson number as opposed to Osborn's method reduced deviations to a maximum of 30%. The direct measurements of K_ρ and K_m were compared with models (Pacanowski & Philander, 1981; Peters *et al*., 1988) and oceanic measurements (Peters *et al*., 1995) and poor agreement was found. When eddy viscosities were non-dimensionalised by ΔU and L_o better agreement with theory was obtained. Eddy diffusivities and the flux coefficient were found to be directly related to a characteristic Richardson number. This indicated that either, a_s and R were relatively constant across the experimental investigation, or that linear stability analysis was not applicable to the type of turbulence observed. It was unlikely that KH billows were observed as $R \approx 2$ across the range of experiments.

The entrainment velocity (u_e) is the rate at which a mixed turbulent layer, of nearly uniform density and with a thickness of D, thickens ($u_e = dD/dt$). Many entrainment coefficients (E_n) have been derived (in the form $E_n = u_e/U \approx C_c\, RI_B^{-n}$; where U was the mean horizontal velocity, C_c and n were constants), using many different experimental approaches, that relate entrainment to Richardson number. A thorough review of the various entrainment coefficients can be found in Fernando (1991). Strang & Fernando (2001b) produced highly resolved experimental measurements of E_n. It was proposed that below a critical Richardson number KH instabilities had altered the entrainment rate subtly; otherwise E_n was found to be in good agreement with previous studies. It was shown that entrainment was independent of Ri_B when Ri_B (Ri_g<0.09) was small ($E_n = u_e/U \approx 0.024$), which was consistent with Christodoulou (1986), who found that entrainment had a constant value in the range $0.02 < u_e/U < 0.04$ at low Ri_B. Strang & Fernando (2001b) demonstrated that, for larger values of

Ri_B ($0.1<Ri_g<1$), E_n was proportional to Ri_B but with considerable scatter. At larger values again ($Ri_g>1$) only Holmboe billows occurred and E_n remained proportional to Ri_B. A fourth regime was possible, but no measurements were presented. This regime was dominated by viscosity, so it was unlikely to make a meaningful contribution to mixing (see Fernando, 1991). Mixing efficiency (also Strange & Fernando, 2001b) was found to fall into 3 regimes. For low Ri_B, i.e. in a KH regime, mixing efficiency was low ($\Gamma<0.15$). As Ri_B was increased it was proposed that KH billows resonated with 'wavelike' (probably symmetric Holmboe) instabilities causing a higher mixing rate ($\Gamma<0.4$). Increasing Ri_B further led to the often quoted mixing rate ($\Gamma\approx0.2$) and a Holmboe type mixing regime.

3 Experimental setup - Three layer stratification

3.1 Experimental description

The experiment was designed in such a way that comparisons could be made between the laboratory and oceanographic scales. This was achieved by matching geometrical aspect ratios as far as practicable and ensuring internal Froude similarity between model and prototype conditions. The Froude number (Fr) is defined as:

$$Fr = U /(g'H_2)^{0.5} \qquad \text{Equation 17}$$

Where U is the characteristic velocity of the shear layer and $(g'H_2)^{0.5}$ represents the velocity of an internal gravity wave on the pycnocline. The Bulk Richardson number (Ri_B) is equal to the square of the inverse Froude number.

$$Ri_B = 1/Fr^2 = g'H_2 / U^2 \qquad \text{Equation 18}$$

The bulk and gradient Richardson numbers are equivalent ($Ri_B = Ri_g$) when R=1. For conventional reasons Reynolds number similarity could not be satisfied. Experiments were run only for high values of the appropriate Reynolds number in order to exploit the weak dependence of flow properties upon Reynolds number (particularly within the turbulent eddies associated with breaking). The presence of lateral confining walls had a frictional effect upon the ISWs, previous experiments (Fructus et al, 2009) have shown that this effect was not dynamically important for the development of the wave.

The schematic experimental arrangement can be seen in Figure 10. A rectangular-section, horizontal tank of length L and width W was filled initially with a homogeneous layer of fluid of density ρ_3 to a depth H_3. A linearly-stratified layer (pycnocline) of thickness H_2 was then

placed above the first layer using the double reservoir technique (Fortuin, 1960; Hill, 2002; Economidou & Hunt, 2009) such that the density within this layer varied linearly between ρ_3 and ρ_1. The upper homogeneous layer of density ρ_1 and thickness H_1 was then added via a floating sponge. The total depth of the fluid system was H. An excess homogenous volume of fluid of density ρ_1 was then added behind a partially-lowered, solid gate G located at a distance L_G from one end of the tank ($L_G << L$), resulting in a depression η_0 in the pycnocline behind the gate. When the gate was removed vertically, a single ISW of depression propagated away from the gate on top of the pycnocline in the main part of the channel. The geometrical dimensions of the section of the tank behind the gate (and the magnitude of the excess volume of fluid of density ρ_1) were chosen carefully (Kao *et al*., 1985), in order to generate a single solitary wave of prescribed amplitude a and half-width λ_H, see appendix G for details.

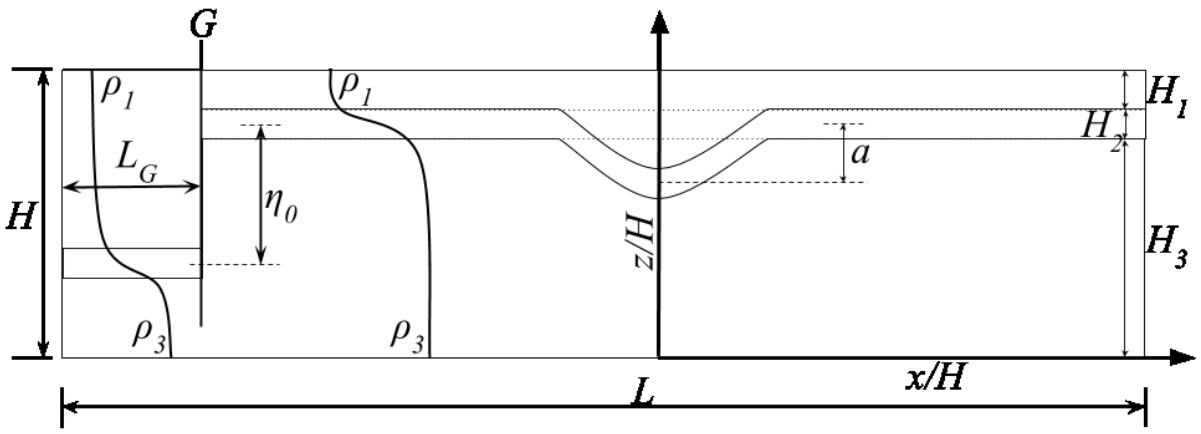

Figure 10 – Schematic experimental setup for the three layer experiments

The experiments were performed in a wave tank having dimensions 12.6m x 0.5m x 1m, as described in Fructus *et al*. (2009). The prescribed density difference $\Delta\rho$ ($\Delta\rho=\rho_3-\rho_1$) was 25.0 ± 1.5 kg/m^3 in all cases. After the tank had been filled, a rigid lid was placed on the free surface of the upper layer. The rigid lid configuration has been used commonly in internal

wave experiments in the laboratory (e.g Fructus *et al*., 2009). The rigid lid served several purposes. Firstly, it made comparisons with numerical simulations, in which the rigid lid assumption has been commonly applied, more straightforward. Secondly, it suppressed surface tension effects that are known (Grue *et al*., 1999) to generate spurious effects in such experiments. Finally, the lid suppressed spurious free surface disturbances associated with the generation of the ISWs.

The densities $\rho_{1,3}$ of the saline solutions were chosen to ensure that the small, spherical, light-reflecting Pliolite tracer particles (150-300μm diameter), that were added to the system for flow visualisation purposes (such as Particle Image Velocimetry (PIV)), were neutrally-buoyant at some height within the pycnocline. Natural variations in the density of the Pliolite beads within a given sample ensured that the tracer particles were distributed throughout the fluid depth. Since the particles were present preferentially in the pycnocline, this region was seen most easily and the overturning regions formed when the wave breaks were easily identified.

A bank of light boxes, arranged below the transparent base of the tank provided a narrow, partially-collimated, vertical plane of illumination at the mid-plane of the tank. The motion of the tracer particles within this plane could then be viewed and recorded from the side by an array of three fixed cameras with either, (i) overlapping fields of view, located along the measurement section at approximately $x \approx L/2$, or with (ii) spatially-distinct fields of view, evenly spaced along the measurement section. Images from the fixed cameras were processed using the PIV function of DigiFlow software (Dalziel, 2006; Dalziel *et al*., 2007)

to determine time-dependent synoptic velocity fields (u,v) within the two-dimensional, illuminated sections (x,y) of the wave tank.

3.2 Methodology

There were many potentially important length scales associated with the ISWs. It was decided that the stratification would be fixed and ISWs of successively larger amplitude would be used. This approach varied the parameter R, previously discussed. It was difficult to control Ri_g as there were 5 parameters that set this value, some of which contributed to R (R varies between 0.6...2.2). Therefore it was decided that Ri_g would not be fixed, but kept low ($Ri_g < 0.12$ in all but 2 experiments), to encourage KH breaking. Two experiments with $Ri_g > 0.25$ and $R > 2$ were conducted to investigate H instabilities. Important parameters can be found in Table 1 (Appendix H).

3.3 Defining layers

There cannot be an infinitely thin transition between homogenous regions of miscible fluid that have different densities. Any vertical depth of fluid of homogeneous density was defined as a layer, any transitional region (with reasonably constant gradient) between layers of homogenous density was also defined as a layer. In the literature it has been common for a stratification defined here as a three layer system, to be referred to as two layer system, because numerically a very thin pycnocline can be achieved. The experiments herein, referred to as 'three layer' experiments, had three layers of fluid of thicknesses $H_{1,2,3}$ in the stratification (in the main tank) into which the ISW propagated, this can be seen in Figure 11. Layers were labelled from the surface downward and were measured prior to the ISW passing. Figure 11 demonstrates the method, using the intercepts of the tangents to the vertical density stratification, that defined the intermediate layer depth from the vertical density profile.

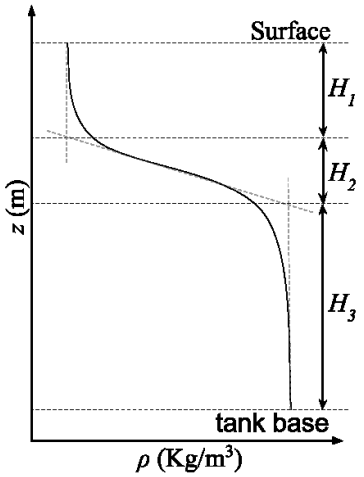

Figure 11 – Schematic plot of depth (z) versus density (ρ) showing the method used to define layer depths $H_{1,2,3}$ in a 3-layer configuration

3.4 Stratifying the tank

In all experiments, the middle layer H_2 was as close to a linearly stratified layer as possible, allowing the buoyancy frequency (N) to be calculated using the gradient of the linearly stratified region (Figure 12). Measurements of the vertical density stratification were made while the tank was at rest, prior to the gate release. Measurement of the buoyancy frequency prior to the gate release was advantageous in the laboratory as the stratified region at the ISW peak was often distorted by the generation of instabilities and billows, making the measurement of N unreliable. The presence of a measurement device, like a conductivity sensor, in the ISW peak would have introduce further unwanted disturbances to the flow.

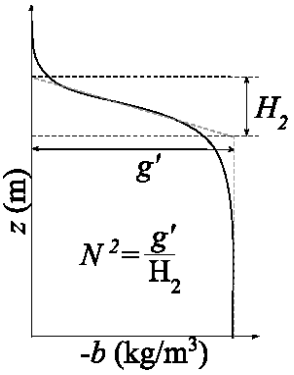

Figure 12 – Schematic plot of buoyancy (b) versus depth (z)illustrating the method used to measure density stratification in regions of non-uniform density, where $-b = g'$.

An alternative method of gaining an appropriate value of the buoyancy frequency within the stratified layer was to plot $N(z)$ and looking for the peak value N_{max}. Using this method it was shown, by several authors (Toole & Schmitt, 1987; Polzin, 1996; Kunze *et al*., 1990) that the measurement of N^2 may be dependent on the vertical resolution (Δz_N) and the variation of Δz_N, if for example, the rate of data acquisition was not constant. It was confirmed in this study that the N_{max} method was more sensitive to the quality and the resolution of the data, consequently the linearised density gradient method shown was adopted.

3.4.1 *Measuring density profiles and layer depths*

Density profiles were obtained by means of an array of rapid-response, micro-conductivity sensors (Head, 1983) located at fixed positions along the channel and mounted on a motorised, rigid, rack and pinion traverse system fitted with a potentiometer. Each of the sensors was calibrated in advance using saline solutions of known density and temperature. At prescribed elapsed times, the sensors were driven rapidly through the fluid depth (in a typical transit time of approximately 1s), to obtain (after application of calibration data) quasi-instantaneous, synchronised density profiles in the breaking part of the ISW. The traverse system was positioned within the field of view of the cameras such that the density profiles could be associated with feature in the flow visualisation. The sample rate of the sensors was low, approximately 100Hz, due to hardware constraints. This was sufficient to capture density profiles as the phenomena of interest, KH and H billows, were large and slow moving. Approximately three samples per cm were obtained, corresponding to approximately thirty samples from a fully developed KH billow. When measuring N ($N=[(g/\rho_0)(\partial\rho/\partial z)]^{1/2}$), $\partial\rho/\partial z$ was substituted for $\Delta\rho/H_2$ as it was assumed that they were effectively the same in a linear stratification. This allowed the linearised density gradient method, discussed in section 3.4, to be used.

3.5 Measuring velocity profiles

Post-processing of the images captured was accomplished using the PIV functionality within *Digiflow* (Dalziel, 2006; Dalziel *et al*., 2007), allowing the horizontal velocity shear to be measured. The depth of the velocity shear layer (d_z) within the ISW was obtained from a vertical transect of horizontal velocities through the peak of the ISW. The profile was averaged over several frames to reduce the noise that arose from PIV errors. The interfacial layer depth (d_z) was defined by the levels at which a tangent to the strained region intersected with a vertical tangent to the peak upper and lower velocities, as depicted in Figure 13. The magnitude of the change in horizontal velocity (ΔU) was defined as shown in Figure 13.

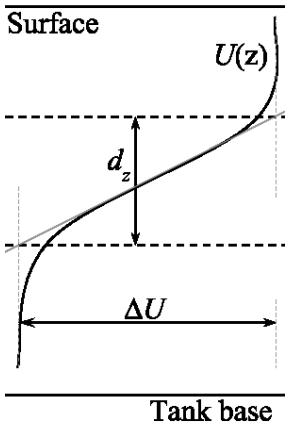

Figure 13 – Sketch defining the vertical thickness of the velocity interface (d_z) and the velocity difference (ΔU) across the shear layer

Alternatively, a plot of $\partial u/\partial z$ versus H would show a peak at the point where the gradient was most steep and this plot could be used to determine the mean level of the velocity interface. This method was not adopted for several reasons: the plot of $\partial u/\partial z$ versus H required smoothing, whereas the gradient method chosen did not (the averaging of several profiles was sufficient). PIV was sometimes under-resolved and the chosen method based on linearised representation of the velocity shear performed better in these situations. As previously mentioned it was shown, by several authors, (Toole & Schmitt, 1987; Polzin, 1996; Kunze *et*

al., 1990) that the measurement of $\partial u/\partial z$ may be dependent on the vertical resolution (Δz_v) and sensitive to variations in sample rate. The chosen method also provided an unambiguous method for numerical comparison. When calculating the gradient Richardson number (Ri_g; Equation 6) $\partial u/\partial z$ was substituted for $\Delta U/d_z$; it was assumed that they were effectively the same when using an idealised linear velocity profile.

3.6 Measurement of ISW amplitude and ISW speed

Measuring the wave phase speed (c) of a breaking ISW was challenging. Establishing the horizontal position of the ISW peak was a somewhat subjective process for a strongly breaking ISW, where the back of the ISW was temporally and spatially varying. The following scheme was devised to obtain an accurate measurement of wave speed.

At a given horizontal position in the camera frame at time $t=t_0$ a vertical column, one pixel in width, of the captured image was retained. At time $t=t_0$+1/30s at the same position in the camera frame another vertical column of image was retained. Placing these and subsequent vertical columns of image in time order produced a time series image of the ISW where the ISW peak was more easily identifiable. Such a time series image can be created for any horizontal position x within the camera frame. Producing times series images at multiple camera positions allowed the position of the ISW peak to be plotted versus time, the gradient of which gave the ISW speed. Carrying out this scheme manually was time consuming, consequently the process was automated.

An algorithm was created which located the bright band, which corresponds with the preferentially-lit pycnocline, within any given time series image. This was done by assuming that the intensity of light vertically had a Gaussian distribution in the preferentially-lit

pycnocline. The preferentially-lit pycnocline was found by fitting a Gaussian distribution vertically at each location in a time series image. By fitting a simple quadratic shape through the pycnocline centre obtained above, the location of the ISW peak was obtained. This allowed the time for the peak of the ISW passing position x to be identified. This procedure was then repeated every 10 pixels throughout the camera frame for each camera. A plot of position against time was produced typically with 100 points. Outliers produced by the linear fitting were removed by the assessment of Cook's distance (Cook, 1979). The gradient of the position time plot gave the wave speed. The error associated with this procedure was assessed to be approximately ±6% by examination of the maximum and minimum gradient lines of best fit that could be drawn through the data. There were further errors associated with the refractive index, present within each image captured, that were unaccounted for in this estimate. Refractive index errors were partially accounted for by calibration of the software (digiflow) displaying the time series images. The remaining refractive errors were small in comparison with other errors in the procedure. (Credit for the algorithm that automated this procedure must go to Dr. Stuart King).

To obtain measurements of the ISW amplitude, time series images from the centre of each camera frame were used. By tracing the initial height of the preferentially-lit pycnocline, and its subsequent minimum height at the ISW peak a measure of the ISW amplitude was found. The ISW amplitude was measured from a given initial height which was always chosen to lie within the initial location of the pycnocline. The initial vertical location of the pycnocline was found using the conductivity sensors. This method ensured that the amplitudes measured are comparable with those reported by Fructus *et al*. (2009). The error associated with the initial choice of the height of the bright patch within the pycnocline was $a \pm \Delta a/2$, where: $\Delta a=(a_2-a_1)$, a_1 was the amplitude measured from the isopycnal that coincided with the

smallest amplitude and a_2 the largest. Uncertainty in the measurement was further reduced by taking 9 similar measurements from three different cameras and from locations within the central third of each camera view. As described above, refractive errors were partially accounted for by calibration of the software displaying the time series image. The remaining refractive error was negligible compared with the selective error associated with choosing a height within, but not expressly on, the boundary of the pycnocline.

3.7 Creating Breaking ISWs in a three layer regime

Breaking ISWs were created in the laboratory in three ways:

- Creating a large amplitude ISW maximised the return flow in the tank (at the ISW peak), this in turn maximised the horizontal velocity difference at the wave peak (see Figure 13). As a result $(\partial u/\partial z)^2$ increased, and the Richardson number at the wave peak decreased. This made breaking more likely. When the amplitude of an ISW reached the conjugate depth (Benjamin, 1966) it would not increase in amplitude, instead the peak of the wave flattened. At this point, making successively larger waves did not result in increased ISW speed and consequently higher shear across the middle layer.

- Reducing the density difference or the reduced gravity (g') across the linearly stratified layer H_2 (pycnocline; see Figure 14) reduced the buoyancy frequency (N), which in turn decreased the Richardson number at the ISW peak, making breaking more likely. Obviously decreasing the density difference to zero prohibited ISW activity.

- Reducing the layer depth H_2. This appeared to be counterproductive because reducing H_2 increased the buoyancy frequency (N) and subsequently increased the Richardson number at the ISW peak. However H_2 was not squared in the Richardson number so

the effect upon Ri_g of increasing H_2 was smaller compared with that of changing ΔU or the reduced gravity (g'). In practice, a thin H_2 was more likely to allow breaking, for otherwise identical conditions. It is worth noting that reducing H_2 changed the Ratio R ($R=d_z/H_2$) which, if a threshold value of R was passed, will change the instability type. Furthermore, it will be shown later in this thesis that reducing the thickness of the pycnocline resulted in more numerous billows. Although breaking can be encouraged in three ways, waves with similar Richardson numbers (at the ISW peak) may experience different instability types because the R value can be very different for a similar Richardson number.

4 Experimental setup - two layer stratification

The stratification in the main tank for the two layer experiments can be seen in Figure 14. Layers were labelled from the surface downward. This stratification was considered a natural extension of the three layer experiments where what was previously labelled H_1 was taken to the limit (zero). What was label H_2 in the three layer experiments, from here on will be label H_1 and H_3 will, from here on be labelled H_2. The density of the volume of water behind the partially submerged gate, that becomes the ISW when the gate is released, matched the density of the water at the surface in the main tank.

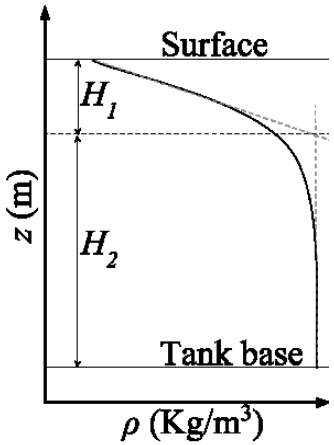

Figure 14 – Defining the layer depths H_1 and H_2 for the 2-layer experiments

4.1 Experimental Description

The schematic experimental arrangement can be seen in Figure 15. A rectangular-section, horizontal tank of length L and width W was filled initially with a homogeneous layer of fluid of density ρ_2 and thickness H_2. A linearly-stratified layer (pycnocline) of thickness H_1 was then placed above the first layer using the double reservoir technique (Fortuin, 1960; Hill, 2002; Economidou & Hunt, 2009) or an alternative technique (see section 4.2 below), such that the density within this layer varied between ρ_2 and ρ_1. The total depth of the fluid system was H. An excess homogenous volume of fluid of density ρ_1 was then added behind a partially-lowered, solid gate G located at a distance L_G from one end of the tank ($L_G << L$),

resulting in a depression η_0 in the pycnocline behind the gate. When the gate was removed vertically, a single ISW of depression propagated away from the gate and on top of the pycnocline in the main part of the channel. The geometrical dimensions of the section of the tank behind the gate (and the excess volume of fluid of density ρ_1) were chosen carefully (Kao *et al*., 1985), in order to generate a single solitary ISW.

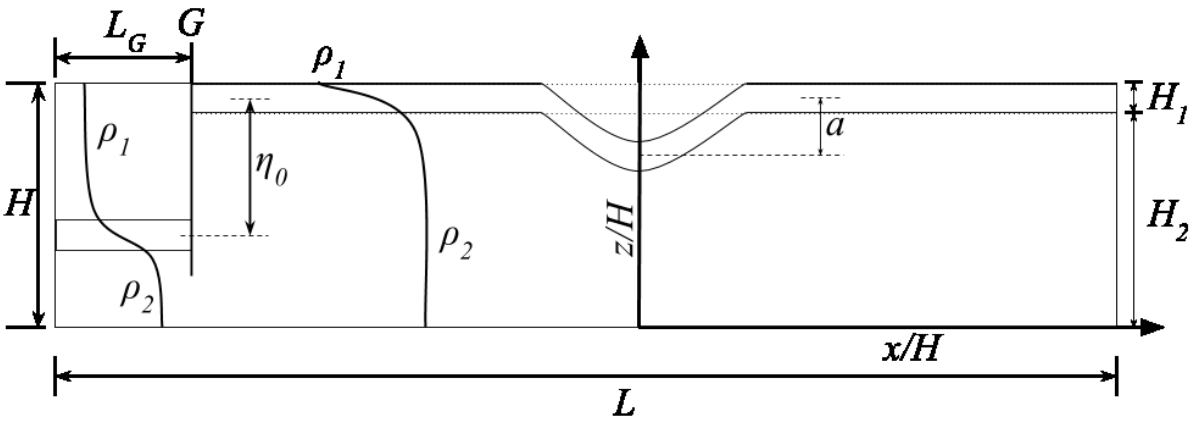

Figure 15 – The laboratory arrangement for experiments with the two layer stratification.

The 2 layer experiments were performed in a wave tank with dimensions of 6.4 m × 0.4 m × 0.6 m, as described in Carr *et al.* (2008). Combinations of salt solutions of prescribed solute concentration were used as the stratifying agents. In some cases after the tank had been filled, a rigid lid was placed very carefully on the free surface as discussed previously. The seeding and illumination of the tank has already been described in section 3.1.

4.2 Stratifying the tank

The stratification obtained using the double reservoir technique was difficult to repeat and it provided a limited range of layer depths for the 2 layer stratification. Consequently, an alternative method (wave method) was used that allowed experimental parameters to be repeated more easily with a broader parameter range. The wave method involved releasing a volume of fluid density ρ_1 from behind the gate into the main tank filled with homogenous fluid density ρ_2. When the fluid in the tank had come to rest a linear stratification remained.

The subtleties of this process were discussed in Appendix A. In all experiments, the upper layer was as close to a linearly stratified layer as possible, allowing the buoyancy frequency (N) to be calculated using the gradient of the linearly stratified region (Figure 16). Measurements of the vertical density stratification were made while the tank was at rest, prior to the gate release.

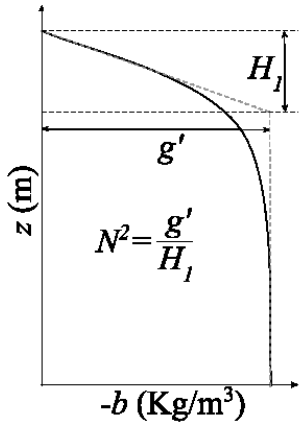

Figure 16 – Schematic plot of -b versus z for the 2-layer experiments

4.2.1 *Measuring density profiles and layer depths*

Density profiles were obtained, as previously described, by means of an array of rapid response (800 Hz) micro-conductivity sensors (Head, 1983; see appendix D for details) located at fixed positions along the channel and mounted on a motorised, rigid, rack and pinion traverse system fitted with a potentiometer (Figure 17).

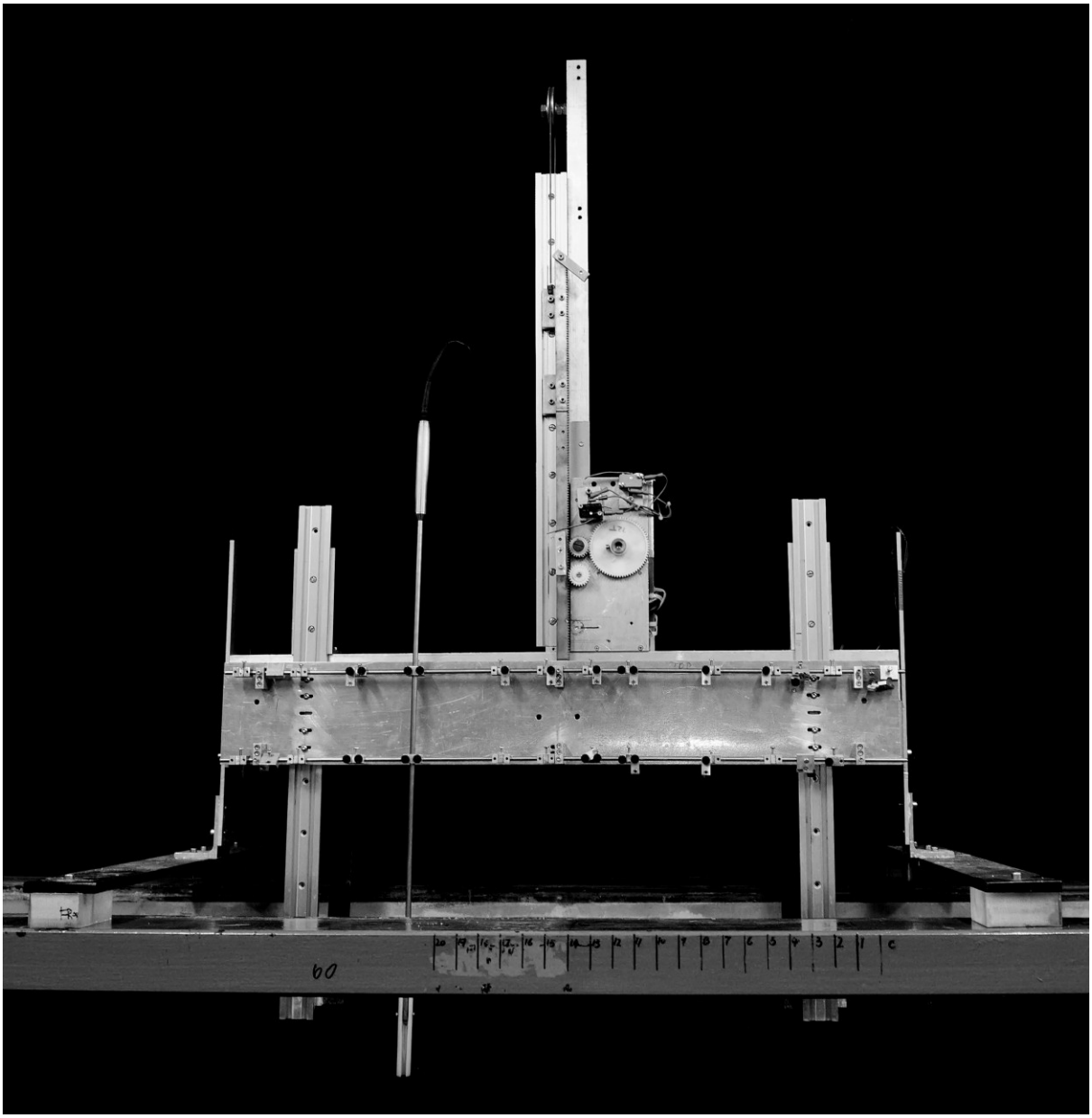

Figure 17 – Side view of the motorised traverse system used for density profiling. A vertically orientated micro-conductivity probe is shown attached to a plate which was driven vertically by the motor. The plate moved on two runners for stability.

For the 2 layer experiments the acquisition rate of the analogue to digital converter (ADC) card (DAS1000; see appendix E for details) was set at a higher rate of 2000 Hz, a previously unattainable rate during the 3 layer experiments due to the hardware constraints at the time. The high sampling rate on the ADC allowed the sensors to be oversampled (their response rate was ~800 Hz) removing any residual aliasing from the signal. A further advantage of the

new ADC was that it accepted 16 analogue channels meaning many more sensors could be used at once, where previously during the three layer experiments the old equipment was restricted to 5 sensors per ADC. The sensors were connected to the ADC via a Bayonet Neill–Concelma (BNC) signal connection box (BNC-16SE; see appendix F for details); schematically this can be seen in Figure 18.

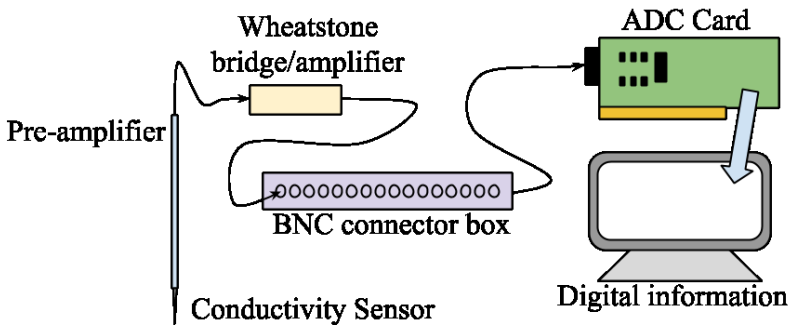

Figure 18 – Schematically the electronics were connected as shown

A stand alone program for Windows was written by the author using labVIEW (National Instruments, 2013) to take advantage of the new hardware.

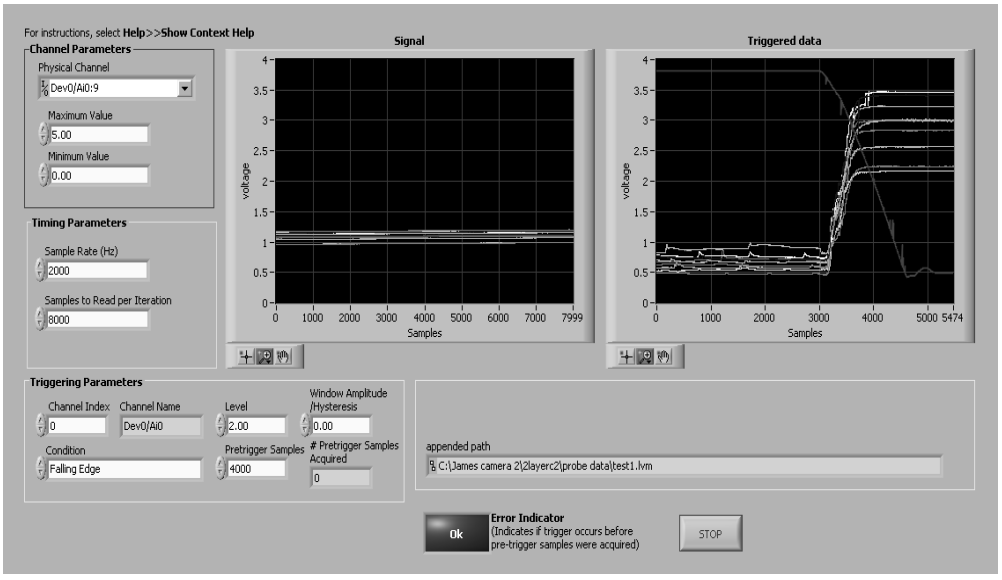

Figure 19 – Data acquisition program

A screenshot of the program can be seen in Figure 19; the right hand side of the screen displayed the last data capture triggered by the signal from channel 0, while the left hand side of the screen displayed a live view of the data stream from the ADC. Various parameters can

be set including the type of trigger, the sample rate and the number of data items per trigger, making it a versatile tool for future studies. Sensor calibration was discussed previously in section 3.4.1.

Layer depths were defined when a tangent to the linearly stratified region intersected with a tangent to the homogeneous layer as depicted in Figure 14. This was done shortly before each experiment was conducted.

4.2.2 *Estimating the background potential energy P_B*

The vertical distribution of density was measured before an ISW was released (solid line in Figure 20), to obtain the layer depths. At this time the fluid was at rest and the stratification was stable so that TKE=0 and P_A=0. Profiles were also taken during an experiment and in the wake of an ISW, after a duration of approximately one wave period (see dashed line in Figure 20). After one wave period the velocity shear across the pycnocline was small and $P_A \approx 0$, i.e. comparing the monotonically reordered background profile (P_{Bs}) to the measured profile (P_B) showed very little change ($P_A = P_{Bs} - P_B \approx 0$). Typically this was true, and if instabilities existed they were small approaching the scale of the noise associated with the sensor. It was also assumed that one wave period gave sufficient time for the Richardson number to rise well above its critical value, it followed that there was no more entrainment due to shear instabilities. From observation this appeared to be true, buoyancy appeared to be dominating after one wave period. Measurements of P_B before and after the ISWs passing would assist in characterising the vertical mixing. The timing of the profiles taken from the ISW's wake was limited to one wave period after the passage of the ISW due to the finite length of the tank. After more than one wave period the profiling was affected by reflection of the ISW on the downstream wall.

There were several sources and sinks of energy in the system which could not be accounted for. The removal of the gate contributed to mixing and ultimately raising the background potential energy. Boundary layers on the tank walls and tank base were another energy sink that was difficult to quantify. For this reason the total energy budget approach was not attempted. Instead the energy loss from the initial stratification was found. It was thought that this may show evidence of the ISW transitioning to the rotating core type ISW.

It can be seen (Figure 20) that the pycnocline was still depressed in the post ISW density profile, this was due to a trailing volume of fluid that did not get into the leading ISW. Given a longer tank, the post wave profile would have recovered to its previous level after the volume trailing the ISW had passed. For this reason the pre and post wave profiles were aligned about the undisturbed section of pycnocline, simulating the pycnocline recovery. This approach excluded an unrealistic energy loss to P_B. Thus only the potential energy, labelled P_B in Figure 20*(b),* was considered.

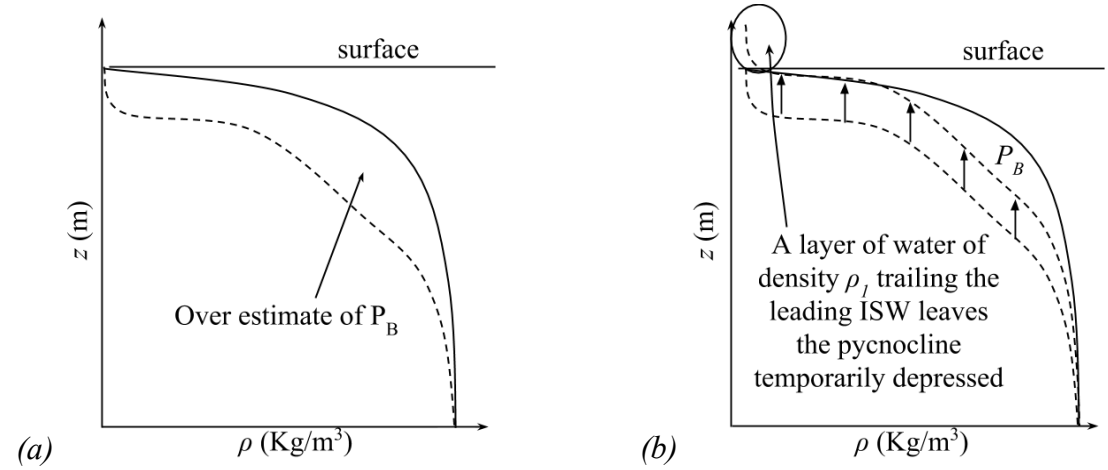

Figure 20 – Defining the energy lost from the background stratification (a) A typical density profile pre (solid line) and post (dashed line) ISW. (b) The post ISW density profile was shifted.

The potential energy (*PE*) of a vertical 1D transect of the water column was calculated by evaluating Equation 19 numerically. This resulted in *PE* per unit area (kg/s^2 per m^2). In the absence of turbulent motions and if local velocities were sufficiently low then P_B was found using Equation 19.

$$PE = \int_0^H \rho(z)\ g\ z\ dz \qquad \text{Equation 19}$$

The area of the segment labelled P_B (Figure 20*(b)*) was found by subtracting the adjusted *PE* of the water column after the wave had passed, from the *PE* of the water column prior to the waves passing. In practice several sensors were used to obtain the vertical transects which were then averaged, reducing the chance of an anomaly in the density field skewing the data. A further example can be seen in section 7.3.

5 Experimental observations – Three layer stratification

Figure 21 shows a side view of a breaking ISW; variation in brightness can be attributed to the variation in concentration of the light scattering Pliolite particles seeded within the flow. The ISW was travelling from left to right, as were the billows which travel in the same direction as the ISW with a speed that was somewhat less than the ISW phase speed. The speed attained by the billows was proportional to the degree of asymmetry of the billow (Lawrence *et al*., 1991). Asymmetry and billow speed has been discussed in more detail in section 6.1.6. The conductivity sensors can be seen twice in a retracted position in the upper part of the image; this was an artefact from the compilation of the composite image. Three camera stills, from three different x/H locations, at two times were used in the composite image. The rear part of the ISW ($x/H < 0.42$) was constructed from images taken simultaneously from 3 cameras with overlapping fields of view. The front part of the ISW ($x/H > 0.42$) was constructed from the same 3 cameras at an earlier time, the non-dimensional interval between the 2 times was ΔtN=17.4. The boundary between the two times is marked by a thin white line at $x/H = 0.42$. Fructus *et al*., (2009) established that the front of a breaking ISW was of constant form, this was verified by inspection of the current experiments. The composite image in Figure 21 therefore represents an accurate view of the ISW as seen in the experiments, with the composite technique merely being required to construct a full wavelength from static cameras, each of which had a field of view too narrow to show the entire ISW.

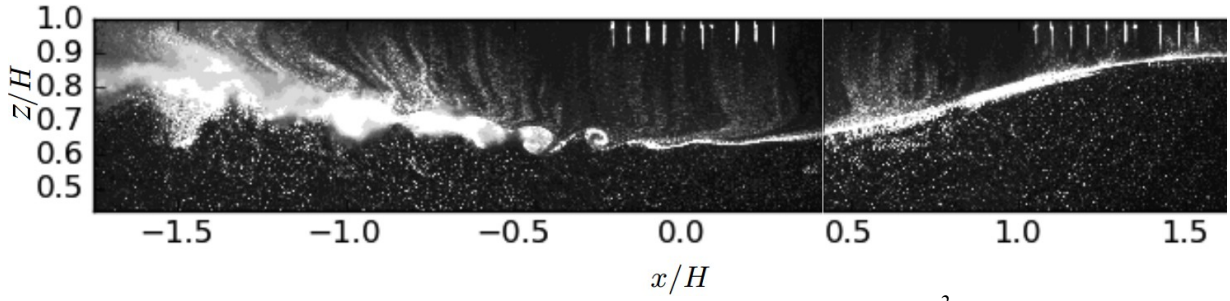

Figure 21 – Composite image from Experiment 141010 where: $N \approx 3.5s^{-2}$, $R \approx 1.1$, $Ri_g \approx 0.07$, $c/c_0 \approx 1.4$, $a/H \approx 0.27$, further parameter can be found in Appendix H.

The velocity shear across the pycnocline was known to vary with horizontal position, reaching a maximum value near the ISW peak (Fructus *et al*., 2009). It can be seen in Figure 21 that instabilities formed on or near the ISW peak, the position of maximum shear. It can also be seen that billows were suppressed on the front of the ISW. This was consistent with previous studies of breaking ISWs both experimentally (Fructus *et al*., 2009), and numerically (Carr *et al*., 2011; Camassa *et al*., 2012). For very large amplitude ISWs instabilities can be found slightly ahead of the ISW peak (Carr *et al*., 2011).

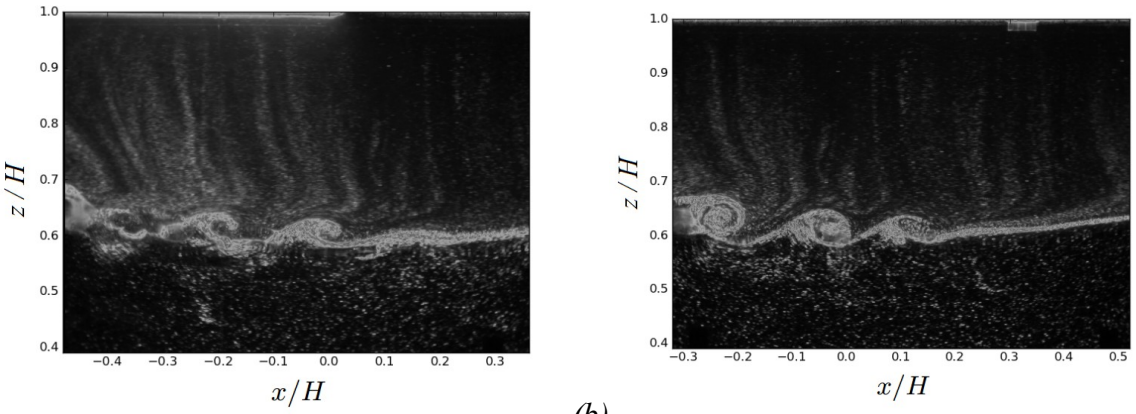

Figure 22 – Images showing billows that appear to (a) not grow in series ($t=t_0$) and that (b) do appear to grow in series ($t=t_0+\Delta t$). Experiment 141010, key parameter in Figure 21's caption.

It was observed that, although the instabilities all started to grow around the ISW peak, they did not always grow from exactly the same point on the ISW. For example Figure 22*(a)* shows two billows that were at approximately the same stage in their time evolution,

therefore they must have grown from two different locations on the ISW. Conversely, at other times the billows can grow from more-or-less the same location on the ISW and therefore appear to grown in series as shown in Figure 22*(b)*. In both cases, billows could be consistently described by tracking their evolution since their own inception, regardless of the position on the ISW. This has been demonstrated in section 6.1.3. The description of a billow was characterised against the time since its own inception from here on as opposed to its position on the ISW.

Figure 23 shows the time development of an individual billow. The initial perturbation's vertical growth (Figure 23*(a)*) was preferentially advected by the shear flow, concentrating vorticity. This initial perturbation subsequently overturned (Figure 23*(b...d)*), forming a recognisable KH billow. The entrainment into the billow appeared to be closed off (Figure 23*(e)*) and the vertical growth slowed. The billow reached its maximum vertical extent at $tN \approx 11$, referred to as saturation, buoyancy became dominant over shear and the billow began to collapse (Figure 23*(f)*).

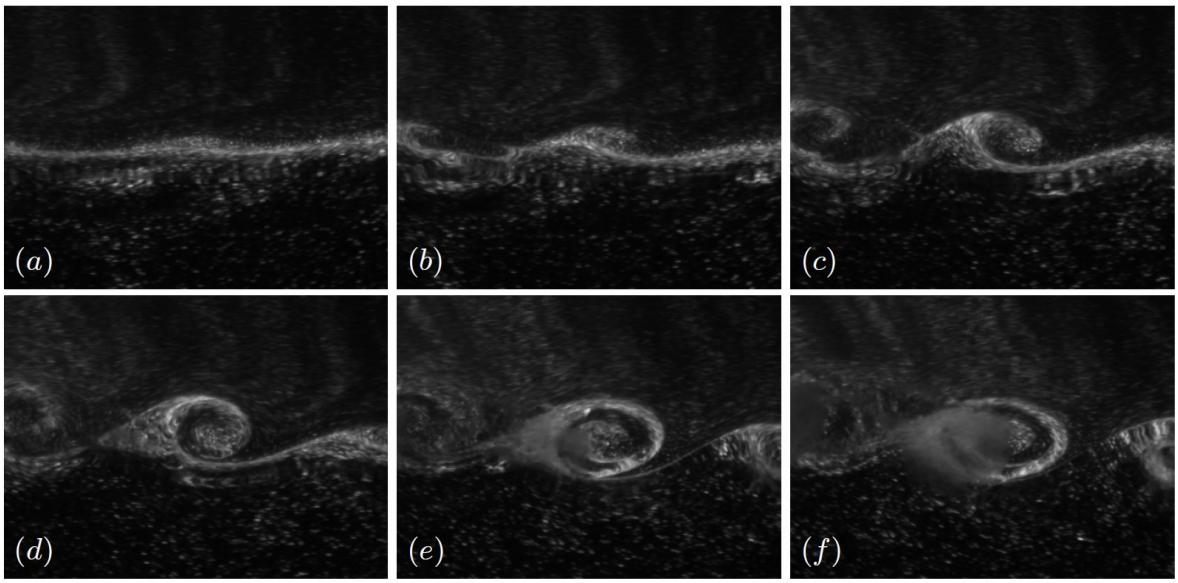

Figure 23 – The evolution of a billow from experiment 141010 key parameter in Figure 21's caption. Where z/H≈0.27 and x/H≈0.38. Panels (a)-(f) correspond to non-dimensional times $(t-t_0)N \approx$ *0, 1.69, 3.39, 4.52, 6.43, 7.79, 11.63, where* t_0 *marks the inception time of the billow.*

It will be shown later (Figure 34, Figure 35) that the non-dimensional time for complete KH billow growth (~11*tN*) was smaller than the non-dimensional time for the parent ISW to overtake the billow (~20*tN*). Consequently, the ISW did not limit the growth of a KH billow by removing the shear flow, prior to the billow reaching saturation. It will also be shown that the time for complete billow growth on an ISW was similar to the time found for billows growing in the uniform shear flow experiments of De Silva *et al*. (1996).

The billows in this study were observed to propagate forward with some percentage of the ISW speed, in the direction of the ISW (see section 6.1.6). It is possible, although it was not observed in these experiments (personal communication Carr, 2011), that some classes of internal waves could exhibit backward propagating billows. In these cases billows could become sensitive to their location on the ISW, as they develop their vertical growth may be limited by the ISW.

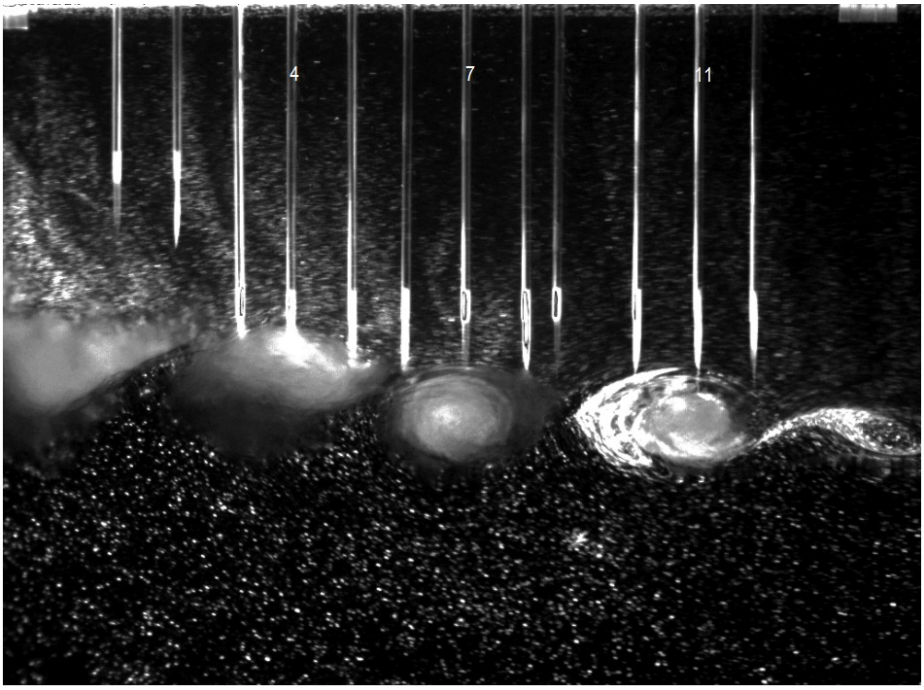

Figure 24 – Conductivity sensors in mid strike positions from experiment 141010 key parameter in Figure 21's caption. Sensors 4, 7 and 11 (indicated), Image size 0.84 x/H, 0.61 z/H.

Buoyancy profiles from billows were obtained when the conductivity sensors passed through the centre of a billow. This can be seen in Figure 24, where sensors 4, 7 and 11 were acceptably close to the centre of a billow. Sensors 8, 9 and 12 strike areas between billows revealing a stable density structure and a pycnocline that was relatively unaffected. This was typical of the undisturbed section between billows. The full buoyancy profiles from the strike can be seen in Figure 25, in which the buoyancy for each successive sensor was offset by unity so that each strike was easily identifiable. The buoyancy profiles in Figure 26 were clipped from full profiles similar to those seen in Figure 25 to show the buoyancy variation within a billow more clearly. The buoyancy profile within a billow evolved with time, the typical buoyancy structure of a KH billow over a generic cycle can be seen in Figure 26. Figure 26*(a)* corresponds with a billow undergoing its first overturn (similar to Figure 23*(b)*), the buoyancy inversion does not reach the ultimate limits of available buoyancy, as it has formed inside the linearly stratified pycnocline and fluid from the top or bottom layer was not

yet drawn into the billow. A second overturn can be seen in Figure 26*(b)*. The outside arm of the billow is now entraining fluid from the upper and lower limits of the pycnocline almost reaching the ultimate values of buoyancy available; typically this would look like the billow in Figure 23*(c)*, *(d)*. Figure 26*(c)* shows a third overturn where the maximum and minimum available buoyancy has been reached, typically this would look like the billow in Figure 23*(e)*, *(f)*. When the billow began to collapse (Figure 26*(d)*), the buoyancy structure of the billow was lost. Mixing and reordering in a buoyancy-dominated regime followed.

Thorpe scale analysis can be used on field data to identify billows in density profiles where no visual confirmation was available (Galbraith & Kelley, 1996). The identified billows may then be used to classify or compare the flow being studied. The Thorpe scale L_T (Thorpe, 1977) can also quantify the vertical scale and structure of statically-unstable regions or overturns. To compare the Thorpe scales in this study with others it was sensible to select Thorpe scales from the centre of billows, which is what is sought in the field. A billow's maximum Thorpe scale will be calculated from vertical profiles recorded within the middle quarter of a billow (De Silva *et al.*, 1996) and in this laboratory study only sensor strikes recorded from the centre (or close by) of a billow have been used. The procedure for obtaining Thorpe scales has been explained previously by Dillon (1982), and elsewhere (Thorpe, 2007). In short, a density profile may be re-ordered to a monotonically stable profile. The minimum vertical distance each fluid particle was moved to achieve this state is referred to as the Thorpe displacement (d') for that fluid particle. The corresponding Thorpe scale represents the RMS (root mean square) value of the Thorpe displacements for a given density profile. The maximum Thorpe scale (L_{Tmax}) used by some investigators, is defined as the maximum value of Thorpe displacement rather than the RMS. The vertical height of a billow (L_b) can be directly measured from any profile in Figure 26. The ratio L_T/L_b has been

found in other investigations (Dillion, 1982; De Silva, 1996) to be approximately constant for any vertical transect of a billow, unlike the Thorpe scales themselves which vary with position. This was discussed further in section 6.1.1.

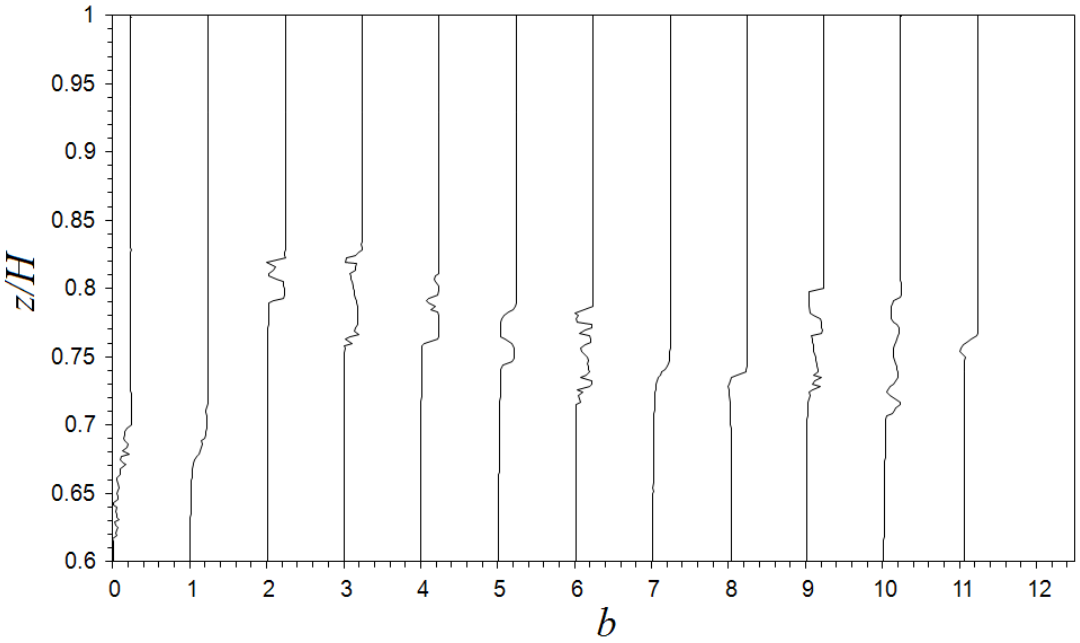

Figure 25 – b versus z/H for the entire strike depth for all sensors in experiment 141010. Note that sensors 1 and 2 were offset vertically for practical purposes; this can also be seen in Figure 24. Each profile was offset by unity so they could be seen more clearly.

Figure 24 shows sensors at mid depth, the sensor strike can be seen to hit the centre of three billows on sensors 4, 7 and 11; these were suitable candidates for Thorpe scale analysis. Consequently the clipped profiles, examples of which can be seen in Figure 26, were used to generate Thorpe scales.

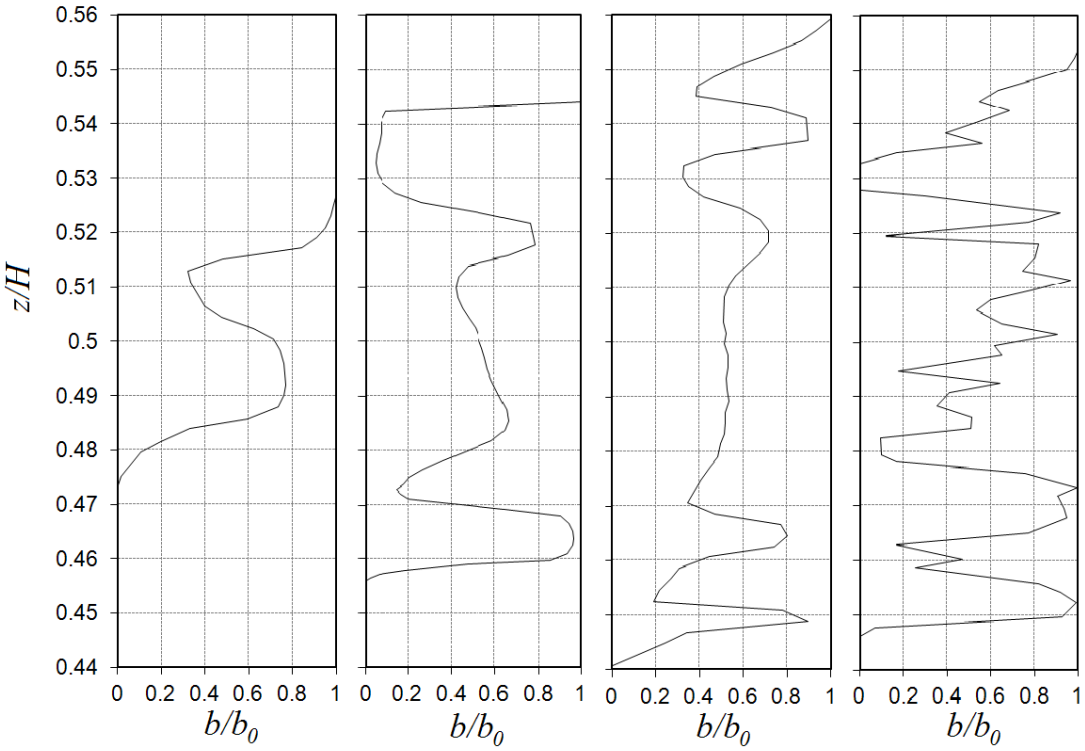

Figure 26 – The vertical buoyancy profile through the centre of a various billows (051010, 230910, 011010, 201010), for non-dimensional times $(t-t_0)N \approx 3.70, 5.85, 7.42, 11.71$ and Thorpe scales $L_T/L_b = 0.40, 0.49, 0.33, 0.42$. Where b_0 was the maximum buoyancy for each profile.

It can be seen from Figure 27 that the mid-density position on the density profile taken before and during a billow's development almost correspond. The assumption that these points overlap was made to estimate billow speed in section 6.1.6. It can be seen in Figure 29 that this assumption does not hold for asymmetric Holmboe billows.

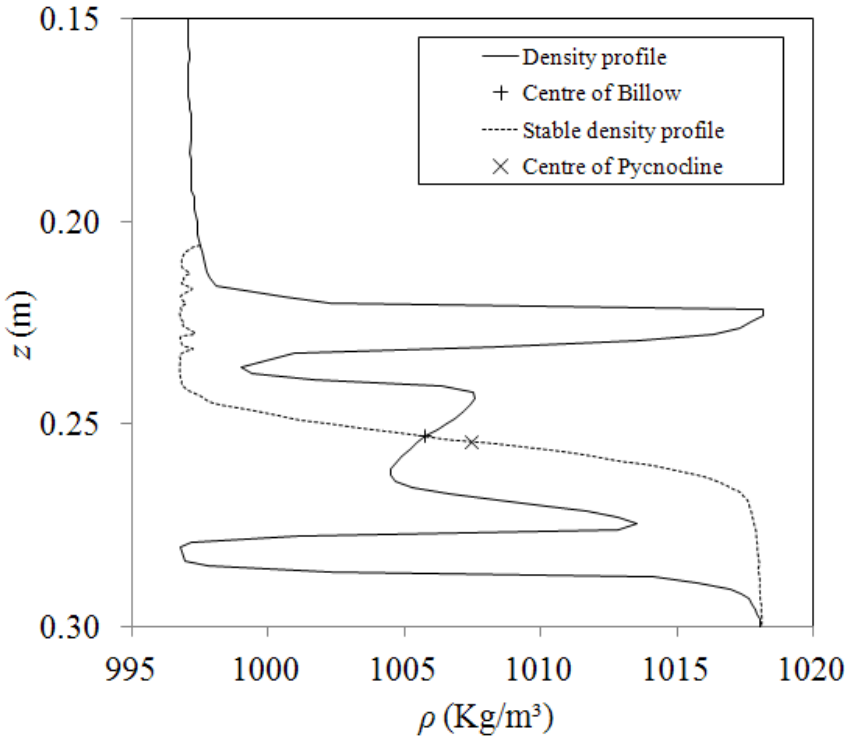

Figure 27 – Plot of z versus density for experiment 011010, parameters can be found in appendix H.

Holmboe like billows occurred in 2 experiments (051010 and 061010). It can be seen in Figure 28 that visually it was difficult to distinguish the Holmboe like billow from the KH billow shown in Figure 23. The most obvious visual difference was that the H billows appeared to be small when compared with KH billows. Without knowledge of the experimental parameters this was not strong supporting evidence that a suspected H billow was not just a small KH billow. Figure 28 illustrates the evolution of a AH like billow. Initially the H like instability had grown and the vorticity concentrated sufficiently to cause the first overturn. At this point, where there was a density inversion we refer to the phenomena as a billow. The H like billow grew vertically at a constant rate (Figure 28*(a)* - *(d)*) until collapse at around $tN \approx 11$ (Figure 28*(e)*). It was not possible to show the typical density structure of H like billow over a generic cycle because there were not enough sampled billows within the H data.

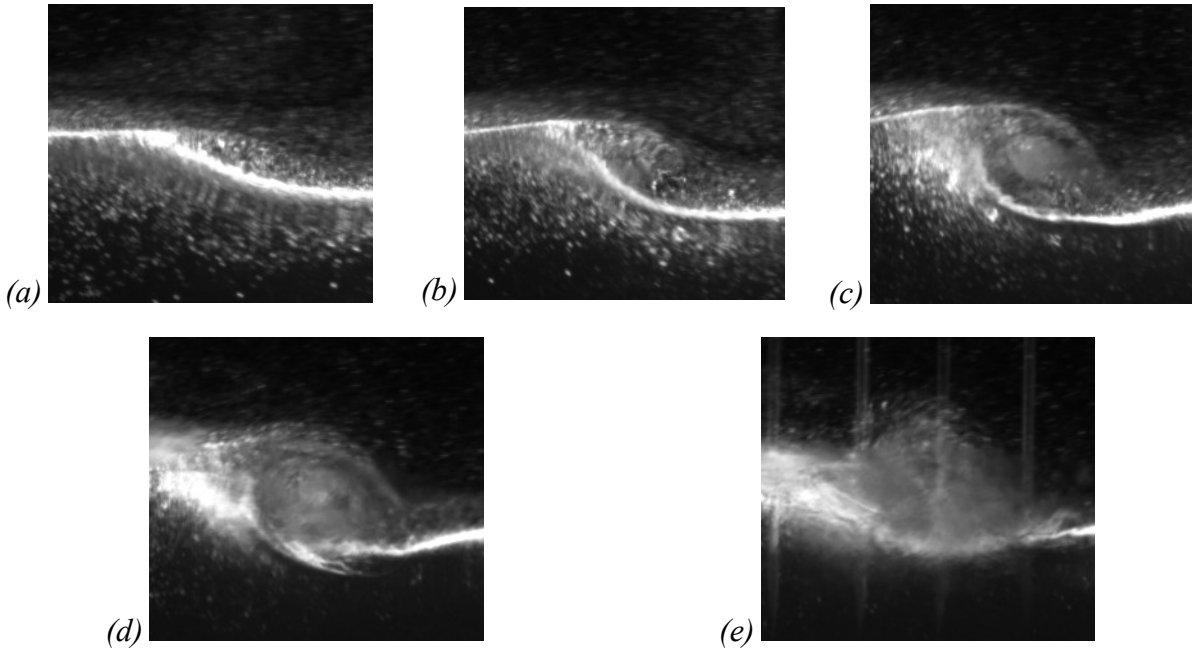

Figure 28 – The evolution of a asymmetric Holmboe like billow from 051010 experimental condition can be found in appendix H, Image size 0.20 x/H, 0.19 z/H. Panels (a)-(e) correspond to non-dimensional times $(t-t_0)N \approx$ *0, 2.55, 5.11, 7.66, 10.21, where* t_0 *marks the inception time of the billow.*

When the density profile from H billows were analysed, the differences between the KH and H billows became more apparent. The density profile that corresponds to the billow pictured in Figure 28*(e),* from experiment 051010, can be seen in Figure 29. It can be seen that the billow had not entrained fluid from the upper and lower extremes of available density. This indicated that the billow had rolled up within the pycnocline. Also it can be seen that the H billow had rolled up in the upper half of the pycnocline unlike the KH billows which rolled up in the middle of the density interface. These were both typical attributes of an asymmetric H billow (Carpenter *et al*., 2010; Carpenter *et al*., 2013). Further evidence, that experiments 051010 and 061010 were exhibiting asymmetric H billows can be found in Appendix H. It can be seen that the parameters R (R=2.1 and 2.2 respectively) and Ri_g (Ri_g=0.25 and 0.32 respectively) were in a regime that would favour H billows. Further differences between the KH and the asymmetric H billows were found when examining the vertical growth rates of the billows (see section 6.1.3).

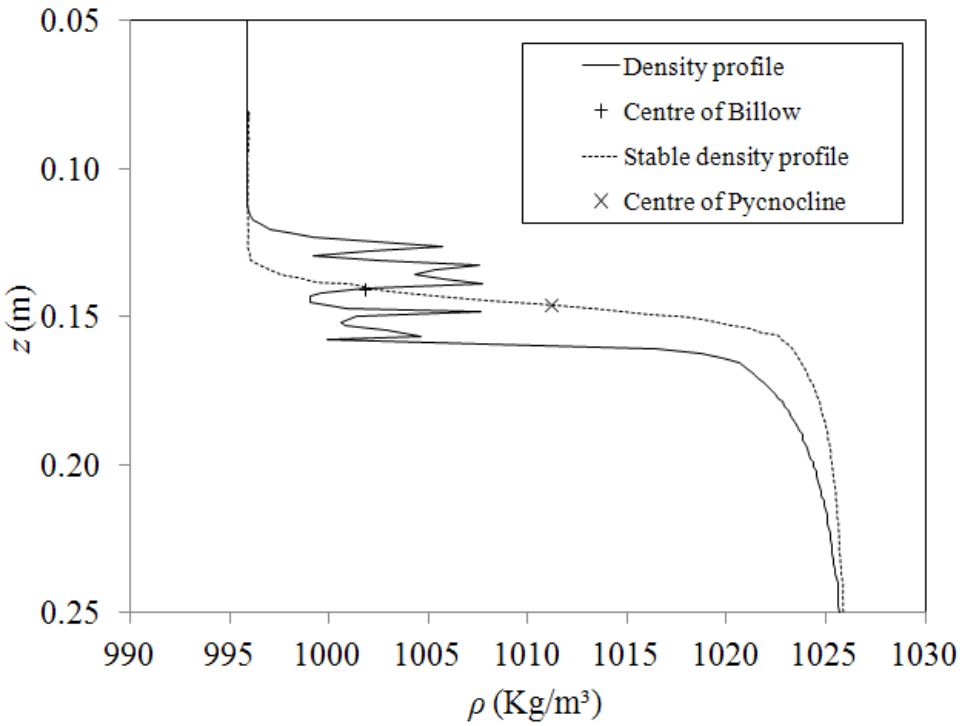

Figure 29 – A density profile through a asymmetric Holmboe like billow from experiment 051010. Experimental parameters can be found in appendix H. The strike can be seen in Figure 28 panel (e).

6 Experimental findings – Three layer stratification

6.1.1 *Billow structure*

As discussed earlier the Thorpe scale (L_T) is widely used in oceanography (Dillon, 1982). Comparing the ratio L_T/L_b found in this study (where L_b is the vertical extent of a billow) with the ratio commonly found in the ocean (Dillon, 1982), revealed that the billows formed on the ISW did not differ significantly in terms of vertical structure when compared to billows recorded in various conditions in the ocean. From Figure 30 it can be seen that the experimental ratio ($L_T/L_b \approx 0.43$) compared favourably with oceanographic estimates (Herbert *et al*., 1992; $L_T/L_b \approx 0.5$ and Gibson *et al*., 1993 ($L_T/L_b \approx 0.41$)) and compared well with numerical values ($L_T/L_b \approx 0.43$, private communication; King 2012). De Silva *et al*. (1996) found that $L_T/L_b \approx 0.49$ was common in the laboratory and the ocean. The Thorpe length scale's relationship with billow height was linear over the range investigated (Figure 30). Accurate measurements of L_b were difficult near the origin as L_b approached the experimental error. At some small length scale L_b will tend to some finite value before reaching the origin; this would be the minimum overturn scale of a billow.

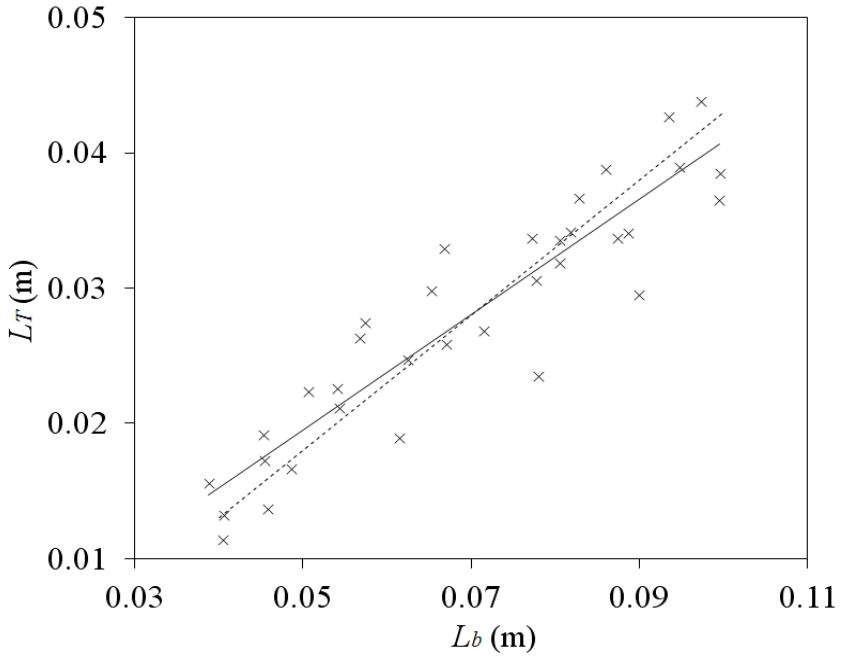

Figure 30 – Plot of L_T (m) versus L_b (m) for all billows measured in the experiments listed in appendix H. Dashed lines $L_T/L_b \approx 0.5$ ($L_T = 0.5\ L_b - 0.007$) and the solid $L_T/L_b \approx 0.43$ ($L_T = 0.43\ L_b - 0.0019$)

The ratio L_T/L_b was approximately constant across all the samples that were obtained in the non-dimensional time range $2<tN<12$. This was an indication that the ratio L_T/L_b was constant over a billow's evolution, admittedly with a wide band of uncertainty. It can be seen from Figure 31 that there was a constant disparity (L_T/L_b or $L_{T\,max}/L_b$) between De Silva *et al*. (1996) and this study. This disparity appeared to be systematic, possibly as the result of experimental or analytical bias, for example the subjectivity in the selection of the billow from the density profile. When selecting the billow from the profile the first deviation from the background density could be used as the upper bound of a billow (as in this study); alternatively one could select the first deviation from the Thorpe distance (d'=0). Using the second definition one could artificially increase the gradient of the (solid) line shown in Figure 30 by 0.05. The error associated with the sensor's resolution and the calibration of the potentiometer could account for the remaining error. The sensors were known to overshoot their estimate of density when a steep density gradient was first encountered.

Several H billows were thought to have been observed in these experiments and, although the mechanism for their generation was different from KH billows, their billow heights and Thorpe scales appeared to scale with those of the KH billows.

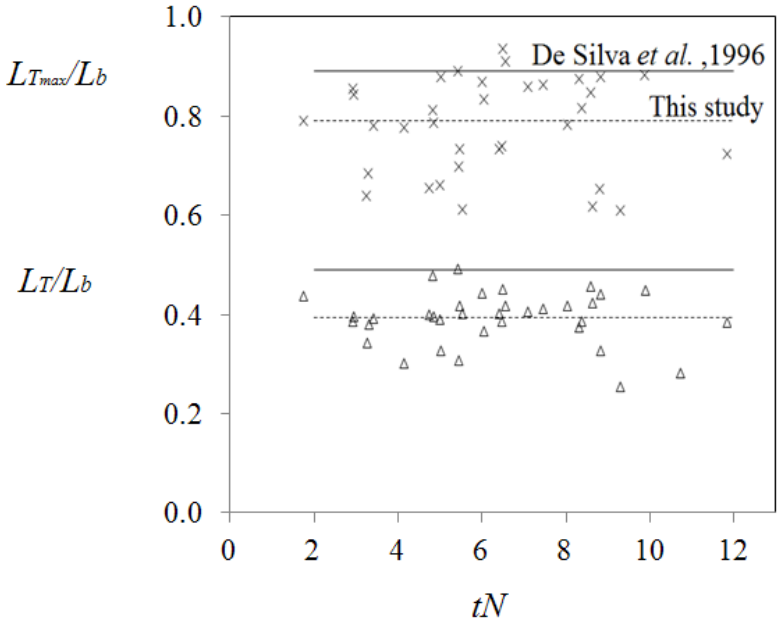

Figure 31 – The ratio L_T/L_b (denoted by x) and L_T max/L_b (denoted by Δ) versus non-dimensional time tN. For all billows measured in the experiments listed in appendix H.

6.1.2 *Selecting a non-dimensional scheme*

As established earlier, KH instabilities emerged from the vorticity field, as a result they can occur in stratified or homogenous fluids. With this in mind it was logical to use a vertical length scale from the velocity field to scale the vertical extent of a billow (L_b). The only vertical length scale available was the velocity interfacial thickness (d_z). De Silva *et al.* (1996) had already shown that the instability wavelength (λ_B) was useful for this purpose; this method was not adopted simply because it did not collapse the data well compared to other length scales. The failure of λ_B to collapse the data cannot be attributed to it being a poor choice of length scale; λ_B was a difficult parameter to measure in the laboratory and as such it had an unhelpful degree of uncertainty. It has been shown (Figure 37) that d_z and λ_B were

linearly related in these experiments, as such the two can be considered interchangeable for the purposes of dimensional analysis. Furthermore, it was thought that describing the KH billow with a property (d_z) of the background flow would prove more useful than describing the KH billow with a property of the flow that was not known a priori (λ_B). tN was chosen as a time scale because it was the only natural time scale in the experiments.

It was tempting to use length scales of the undisturbed system such as those found behind the gate i.e. the excess volume that became the ISW or ISWs when the gate was released. These quantities were avoided as they were not readily transferable to comparisons with oceanographic and numerical ISWs. Intuitively the next best option would be to take the amplitude, wavelength and phase speed of the ISW as the externally-prescribed parameters (at least in the non-breaking cases). However, the pitfall here, particularly for breaking ISWs was that the amplitude, phase speed and wavelength are affected by the breaking. There were other length scales that could have been selected. H_2 could be suitable but as mentioned it was sensible to select a length scale from the vorticity field. Additionally using d_z instead of H_2 would allow the billows from this study to be compared with billows that have grown in a homogeneous fluid (where there would be no H_2). Other length scales such as the external scales H_1, H and H_3 were not used because they did not collapse the data. One would not expect these parameters to scale with the shear so it was reassuring that they were not found to be useful length scales.

6.1.3 *Billow amplitude*

Billows that grew with the same initial conditions i.e. on the same ISW, were observed to grow vertically at the same rate. This can be seen in Figure 32 where 3 billows from the same ISW were tracked giving their vertical non-dimensional height (L_b/d_z) versus their local, non-

dimensional time since inception (t-t_0N). When overlaid as in Figure 33 it becomes clear that the billows were similar in nature for the same initial conditions i.e. on the same ISW.

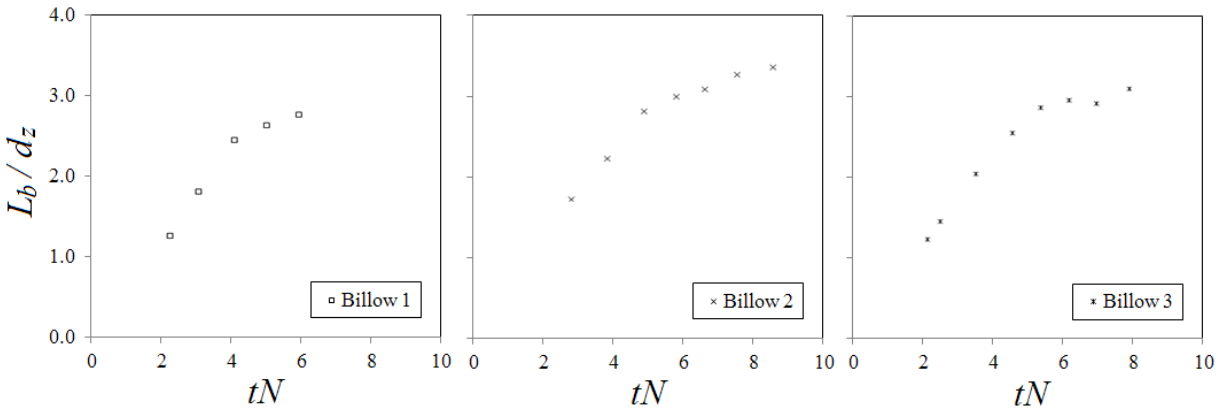

Figure 32 – Non-dimensional vertical amplitude versus non-dimensional time for 3 separate billows occurring on the same ISW (141010). The experimental parameters can be found in appendix H.

The error associated with measuring L_b may have been sufficiently large to mask variations that would otherwise be apparent; as shown in Figure 33. Furthermore only a few billows per ISW were sampled. Instabilities formed in a narrow band of positions on or near the ISW peak. It would be sensible to assume that this could also provide variability in the initial condition and resultant billows, as shear varied (albeit slowly) across the ISW peak.

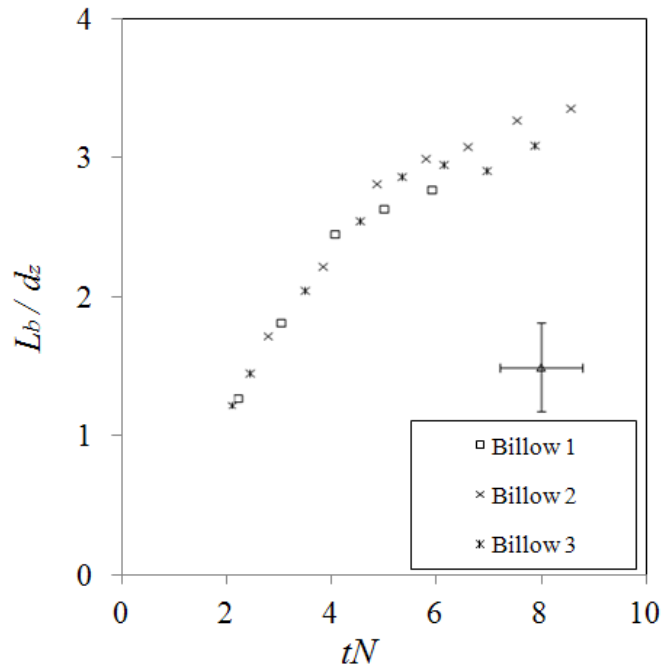

Figure 33 – Non-dimensional vertical amplitude versus non-dimensional time for 3 billows overlaid together, occurring on the same ISW (141010). The experimental parameters can be found in appendix H.

The approximate time for an ISW to pass a billow was estimated assuming a billow was stationary. A billow's horizontal velocity was insignificant compared to the wave speed in all cases. The time for the complete vertical growth of a KH billow ($tN \approx 11$), was shorter than the typical time for the ISW to overtake a growing KH billow ($tN \approx 20$). Consequently a billow was supplied with shear by the ISW for long enough to reach saturation. If the time scale of the billow and ISW had been comparable the ISW would have limited the vertical extent of a billow by removing the driving shear before saturation. This was not the case in this study but conceivably it ws possible.

When the dimensionless plots of the billow height versus time (Figure 33), from all the experiments, were plotted together it became clear that there were three different regimes of billow growth (Figure 34, Figure 35 and Figure 36). The ratio of velocity to density interfacial thickness ($R=d_z/H_2$) was found to be the determining parameter between the three

regimes. The parameter R has been used previously to separate different instabilities during linear stability analysis (see Smyth & Winters, (2003) and Carpenter *et al*. (2010) for a detailed explanation of the classification of different instabilities and consequently billows).

In the range $0<R<1$ (Figure 34) (regime 1) i.e. when the velocity interface thickness was greater than the density interface thickness, a KH instability grew only for a short time in the pycnocline before it was growing in the upper and lower homogeneous dense layers. Billows of this type (when $0<R<1$) exhibit a constant growth rate $L_b/t = 0.42\ N\ d_z$. This constant growth rate was followed by collapse at non-dimensional time $tN\approx11$, reaching a maximum vertical extent of $L_b/d_z\approx5$. It has been shown that d_z was proportional to λ_B (see Figure 37); it follows that if R was small λ_B was also small. The difference in appearance between regime 1 and regime 2 billows could be attributed to λ_B confining the billows in regime 1 and not confining them in regime 2.

Experimental and numerical data from low R value billows are rare; consequently there was a lack of data available for comparison with regime 1. Strictly speaking, in regime 1, R varied in the range $0.6<R<1$ (see Appendix H), it was assumed that no new behaviour existed between $0<R<0.6$. This assumption was reasonable when considered in terms of linear stability analysis. Revisiting Figure 6, it can be seen that, for fixed Ri_g and λ_B, the likelihood of producing a KH instability as opposed to a H instability increased with decreasing R. It followed that, as R approached zero, only KH instabilities were likely to appear. Consequently it was deemed safe to report regime 1 as being in the range $0<R<1$ instead of in the range $0.6<R<1$.

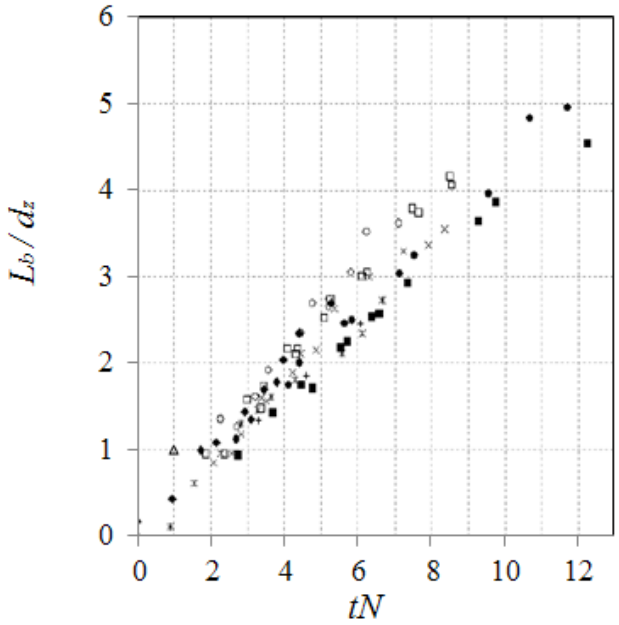

Figure 34 – Experimental vertical growth rate for Runs 1 -7 (see Appendix H) in the range: $0<R<1$ and $0.04<Ri_g<0.06$.

When the velocity interface thickness was thinner than the density interface thickness ($1<R<2$; Figure 35; regime 2), the KH billows were found to grow initially at the constant rate given for regime 1 ($L_b/t \approx 0.42 N d_Z$), between inception and $tN \approx 6$, at which point the growth rate was retarded. Regime 2 covered the range ($1<R<2$) that was typically investigated in parallel shear flow experiments; the change in the rate of vertical billow growth was typical of those experiments (Thorpe, 1971, 1973 1985, $1<R<1.7$; Scotti & Corcos, 1972 $1<R<1.4$, Koop & Browand, 1979 $R>1$). Parallel shear flow experiments in this regime compared well with these regime 2 experiments on an ISW (see Figure 38 for a visual comparison). The maximum non-dimensional vertical extent of a billow in regime 2 was $L_b/d_z \approx 3.5$ which occurred at $tN \approx 11$. With increased R comes increased λ_B (see Figure 37). The removal of confinement seen in regime 1, was thought to be responsible for the change in growth rate observed in regime 2. It was thought that the billows were able to spread horizontally due to this lack of confinement. This was not confirmed due to difficulties in measuring billow widths.

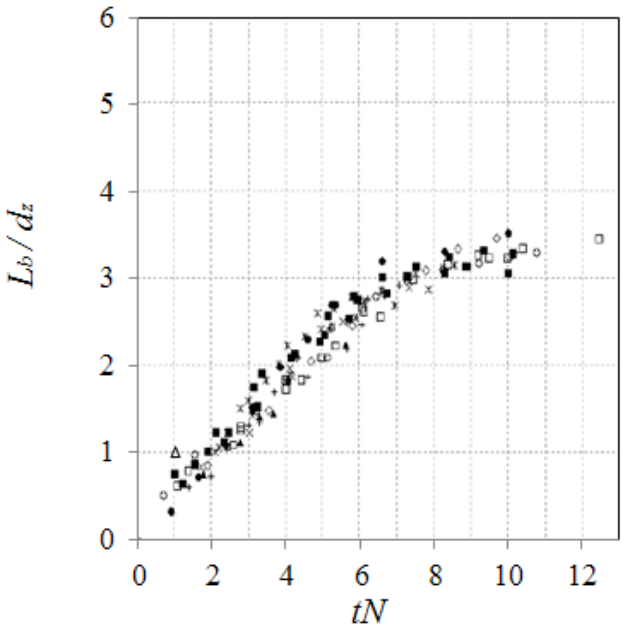

Figure 35 – Experimental vertical growth rate (Runs 8..18 Appendix H) in the range: 1<R<2 and 0.07<Ri_g<0.12.

It was found that when R>2 (regime 3; Figure 36), where the buoyancy interface thickness was at least twice that of the velocity interface thickness and where the billows grew in the linear stratified region, billows exhibited a much lower growth rate $L_b/t \approx 0.12Nd_z$ (when compared to the 0<R<2 data shown in Figure 34 and Figure 35). The lower growth rate shown for the R>2 regime was ascribed to the occurrence of H instabilities, in contrast to the 0<R<2 cases in which the KH instability dominated.

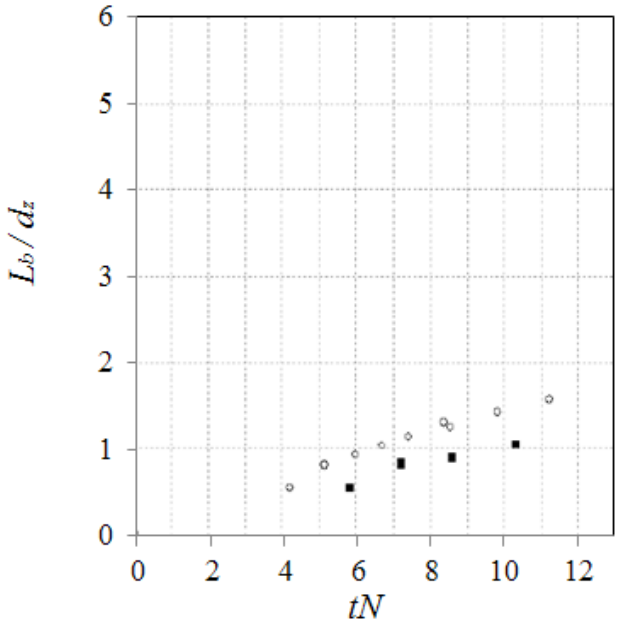

Figure 36 – Experimental vertical growth rates (Runs 19 & 20 in table 1) in the range: R>2 and 0.25<Ri_g<0.32.

When Ri_c becomes very low, as was the case for the two experiments shown in Figure 36, linear stability theory for parallel shear flows suggests that KH instabilities would require an extremely low Bulk Richardson number to form. In the absence of an extremely low Bulk Richardson number KH instabilities are supplanted with the next fastest growing instability, the H instability. In the numerical study of parallel stratified shear flow, Smyth and Winters (2003) found that the boundary between KH and H instabilities occurred at R=2.4 whereas here, with ISWs, it is found to occur at R≈2. The time scale for complete growth of the H type instabilities cannot be given on the strength of only two experiments. Similarly the vertical extent of the billows at saturation cannot be safely estimated. It is thought (Smyth and Winters, 2003) that H instabilities can grow for much longer than KH instabilities. The shear environment on the ISW was significantly weaker when tN>>11 near the back of the ISW. With this in mind it was possible that the ISW was limiting the time for growth for a H instability and as a consequence limiting the maximum vertical extent of a H billow. This could have resulted in a reduced amount of mixing for a H billow on an ISW compared to a H billow on a horizontal shear flow. It was difficult to ascertain if this was the case on the

strength of two experiments, therefore the maximum vertical extent of the H billow was not estimated nor was the time required to reach saturation.

6.1.4 *Billow wavelength*

The non-dimensional billow wavelength (λ_B/H_2), defined here as the horizontal distance between billow cores, was found to scale approximately linearly with the velocity interface thickness (d_Z) (Figure 37). Each data point on Figure 37 represents an average billow wavelength for a given experiment at a given observational point; two observational points have been plotted.

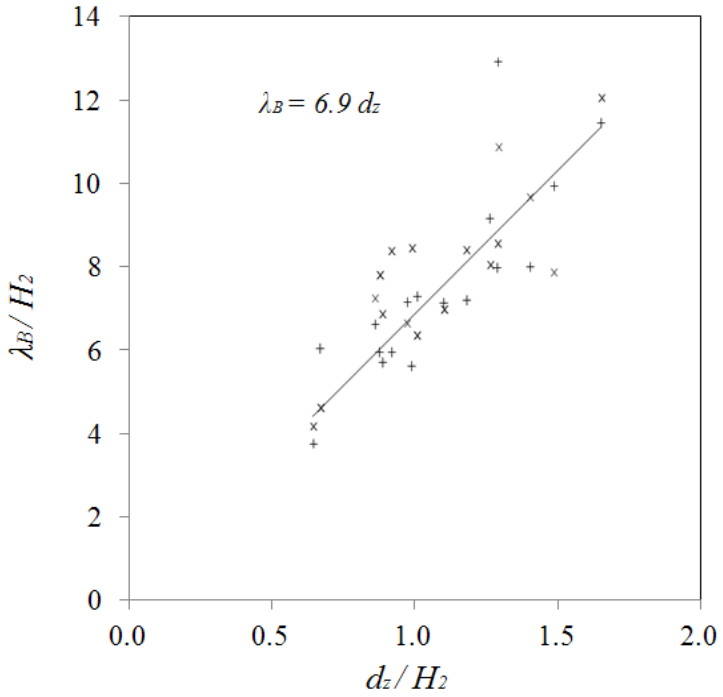

Figure 37 – Dimensionless plot of billow wavelength (λ_B/H_2) versus density interface thickness (d_z/H_2) for all experiments where 0<R<2. Where the x *symbol represents λ_B measured at the first observation point and the + symbol indicates λ_B measured at the second observation point. The experimental parameters can be found in appendix H. The error (coefficient of determination) on the line of best fit was 0.73.*

Fructus *et al*. (2009) reported that the λ_B had a linear relationship with H_2 about the gradient 7.9 while the billows were near the centre of the ISW ('early time' billows), but noted that at later times λ_B reduced in the rear of the ISW. Billows in the strongly breaking cases in this

study were not usually coherent enough to track far into the rear of the ISW; the poor quality of 'late time' data prevents a comparison with Fructus *et al*. (2009). Early time measurements ($0<tN<9$) demonstrated a constant λ_B in approximate agreement with early time estimated from Frutus *et al*. (2009).

De Silva *et al.* (1996) evidently did not find that λ_B varied with time (for parallel shear flows), because that would have preclude its use in their non-dimensional scheme. Thorpe (1971) found that λ_B varied linearly with d_z about the gradient 3.5, approximately half the value found in these experiments, again this value was constant. Koop & Browand (1979) reported that λ_B varied linearly with d_z about the gradient 1.5. It appeared that, although far from demonstrated, the relationship $\lambda_B \approx k\ d_z$ (where $1.5<k<7.9$) was sensitive to the type of experimental setup. It may have been that the choice of experimental setup had a systematic effect on the asymmetry of the flow and consequently λ_B. Linear stability theory, for parallel shear flows, tells us that increasing flow asymmetry will increase λ_B, for fixed Ri_B and R (Haigh & Lawrence, 1999; Hazel, 1972). ISWs are known to have highly asymmetric flows whereas tilt tank shear flows are known to have close to symmetric flows.

6.1.5 *Time evolution of billow*

The vertical growth rate of the KH billows in the range $1<R<2$ on an ISW were compared with billows growing in horizontal shear flows. Horizontal shear flow studies have tended to be in the regime $1<R<2$ (Thorpe, 1971, 1973 1985, 1<R<1.7; Scotti & Corcos, 1972 $1<R<1.4$, Koop & Browand, 1979 $R>1$; De Silva *et al*., 1996, $R\approx1$). De Silva *et al*. (1996) compared KH billows (that had not paired) in the atmosphere, ocean and laboratory, demonstrating that a common time and length scale existed allowing billows of various scale to be compared. It was suggested that the dimensionless time for complete growth of a KH

billow was approximately $\Delta Ut/\lambda_B \approx 5$ for parallel shear flows; this value compared well with the experimental results for ISWs presented here (Figure 38). Early numerical work by Patnaik *et al.* (1976) found that the 'climax state' (maximum billow amplitude) occurred at $Ut/\lambda_B \approx 1.3$ and 'relaxation' occurred at 4, (where $200<Re<400$) which was qualitatively similar to the experimental finding of Thorpe, (1973) and De Silva *et al.,*(1996). More recently Rahmani (2011) used analytical and DNS methods to investigate mixing in KH billows in horizontal shear flows at larger *Re* ($200<Re<240{,}000$) demonstrating that Patnaik's results were dominated by *Re* effects. Rahmani obtainined good agreement with the results presented in this study (see Figure 38*(b)*) and previous experimental studies (De Silva *et al*., 1996; Patnaik *et al.,* 1976; Thorpe, 1973), finding saturation at time $Ut/\lambda_B \approx 4.6$ when $Re>1000$ and $0<Pr<1000$ at a non-dimensional maximum vertical extent of $L_b/\lambda_B \approx 0.5$.

It can be seen in Figure 38*(a)*, an excerpt from De Silva *et al.* (1996), that there was a slight discrepancy between Thorpe and De Silva *et al*.'s measurements of billow growth rate and this study. Given the uncertainty on the measurements it can be seen that (Figure 38*(b)*) the difference was insignificant and the data matched when Thorpe and De Silva *et al*.'s measurements were reduced vertically by 10%. Unlike horizontal shear flows billow on an ISW were translated vertically by the passing of the ISW. It appeared that the vertical growth rate of ISW billows, time to saturation and maximum amplitude were unaffected by the vertical displacement they underwent when compared with billow on a horizontal shear flow (Figure 38). The conditions at the inception of the instability (i.e. at or near the peak of the ISW) appear sufficient to determine the subsequent billow evolution.

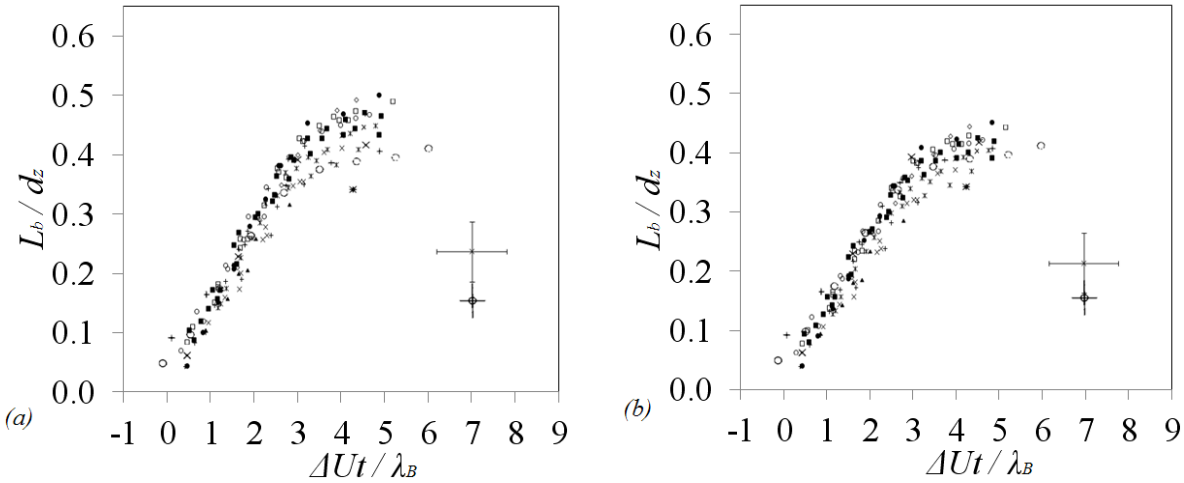

Figure 38 – (a) De Silva et al. (1996) and Thorpe's (1973) plot of L_b/λ_B versus $\Delta Ut/\lambda_B$ with billows from this study (1<R<2) overlaid (b) with the y axis shrunk by 10%.

6.1.6 *Billow speed*

Individual billow speeds were found to be constant from inception until saturation. An accurate measurement of billow position was impossible once billows had begun to collapse in the turbulent rear of the ISW. A typical example plot of billow position versus time can be seen in Figure 39; an average value of C_b was taken. At any non-dimensional time tN, the x/H distance between lines corresponded to the billow wavelength λ_B. The error in measuring the experimental billow speed was estimated to be ±10%. The variation in billow speed was possibly due to small variation in the initial conditions of the billows, as they originated from a band of positions on the ISW peak. The average distance between measurements for Figure 39 was 30 pixels. Given that a selection error of 6 pixels at each point was easily achieved, sampling more frequently would have been of no advantage.

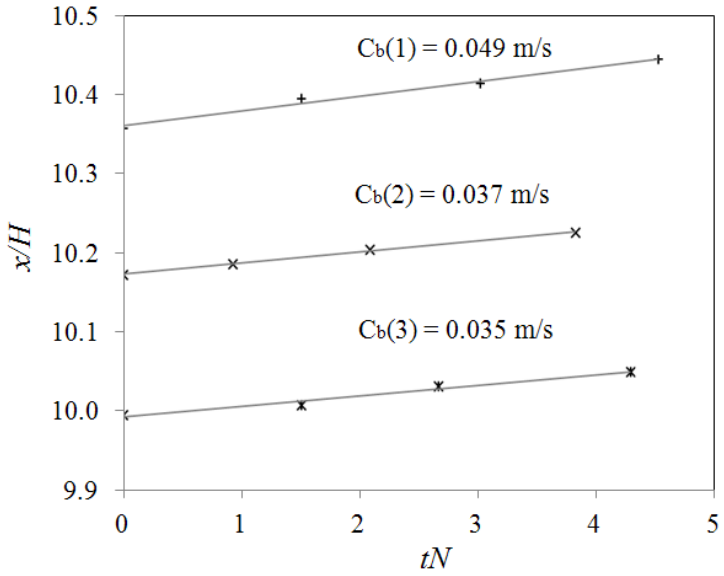

Figure 39 – Plot of billow centre position x/H versus time tN for 3 separate billows in experiment 141010.

C_b has been noted as being a linear function of the asymmetry a_s (Equation 21; Figure 41) of the flow for shear flows (personal communication: Lawrence & Carpenter, 2012). The asymmetry can be non-dimensionalised by the velocity interface thickness (d_z) as:

$$a_{sn} = (Z_2 - Z_1) / d_z = a_s/d_z \qquad \text{Equation 20}$$

$$C_b = (a_s/d_z)\, C_{wave} \qquad \text{Equation 21}$$

where Z_2 is the vertical distance from some arbitrary datum to the centre of the density interface and Z_1 is the vertical distance from the same arbitrary datum to the centre of the velocity interface (see Figure 40). These values were obtained at the ISW peak for consistency with horizontal shear flow type studies.

Put simply, whatever a billow's vertical position was within a flow it would propagate with the background velocity at that position. For example, when a_s=0, i.e. the centres of the velocity and density profiles were coincident (vertically aligned about the centre of their respective interfacial regions), a billow would be stationary assuming it was generated at the centre of the density interface. When $a_s \neq 0$ the position of the billow (approximately the

centre of the density interface) with respect to the velocity profile governed the propagation speed of the billow. The assumption that a billow's vertical position would be at the centre of the density interface was only approximate. Thus, the asymmetry from the profiles may not represent the true position of the billow relative to the velocity profile. Density profiles taken through individual billows showed that the billows did not always originate from the exact centre of the density stratified layer, as shown in Figure 27. It was obvious from density profiles that the centre of a billow and the centre of the density interface did not coincide but they were close enough for the assumption above to remain approximately true (see Figure 27).

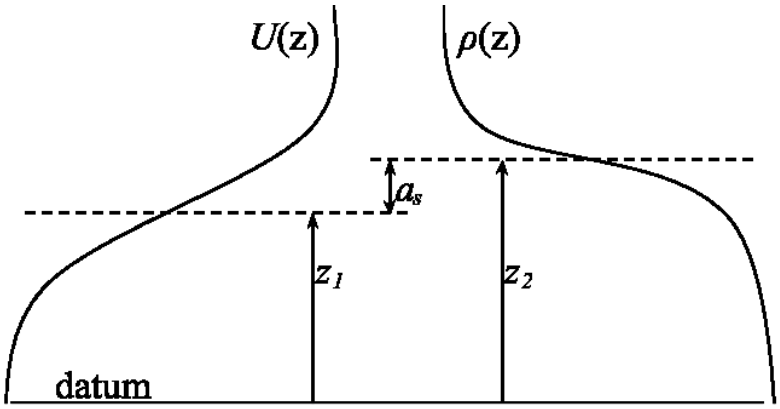

Figure 40 – Sketch illustrating the definition of the asymmetry a_s in terms of the velocity U(z) and density ρ (z) profiles. See the text for definitions of $Z_{1,2}$.

This assertion appeared to hold when applied to the experimental data (Figure 41), although the correlation appeared noisy. It can be seen (Figure 41) that the equation posed in Fructus *et al*. (2009):

$$C_{best} = 0.09\, C_{wave} \qquad \text{Equation 22}$$

where C_{best} was the estimated billow speed and C_{wave} was the ISW speed, predicted billow speeds accurately over a very small parameter range and badly over the whole range. The high degree of scatter in Figure 41 can be attributed to several factors:

The asymmetry of the flow at the ISW peak cannot be measured directly in the laboratory. The presence of the billows in the ISW peak distorted the density field and refraction distorted the visual measurement of the velocity field. Therefore, a steady state numerical model was used to estimate the asymmetry based on the experimental ISW. The match between numerical and experimental ISWs was estimated to be ±5% in amplitude, having specified the wave speed. This approach was validated previously (Fructus *et al.*, 2009) using non-breaking ISWs.

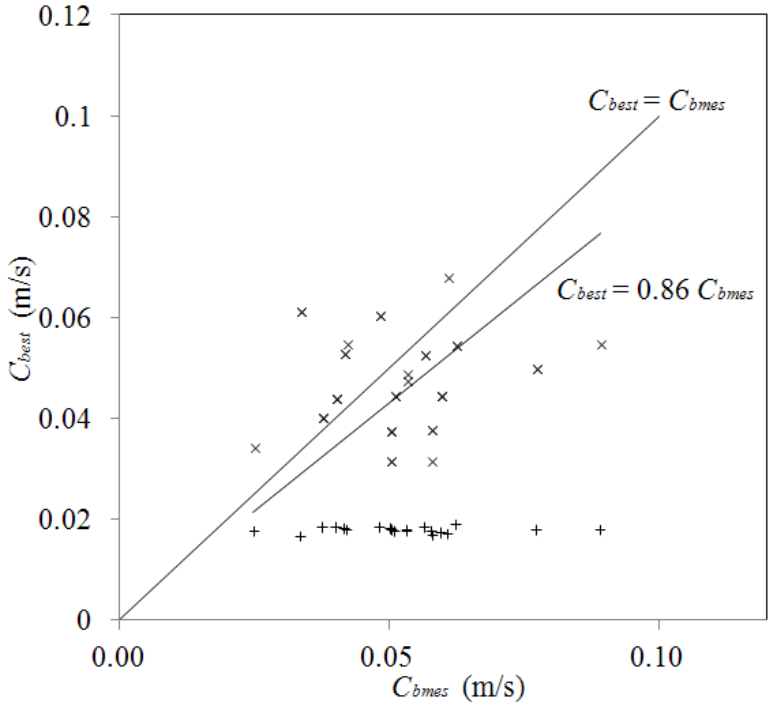

Figure 41 – Billow speed C_{best} (m/s) from Equation 22 (+) and Equation 21 (x) versus measured billow speed C_{bmes} (m/s), for all experiments in appendix H.

6.1.7 *Entrainment*

Making a direct comparison with entrainment rates (u_e) from previous studies (Strang & Fernando, 2001b) was not possible. Strang and Fernando's (2001b) experimental measurements were in a regime where the dissipative eddies were isotropic, whereas the measurements from KH and H eddies in this study were from coherent, anisotropic

structures. To make a comparison it was necessary to average a billow over a wavelength and therefore obtain an average entrainment rate. Two assumptions were necessary:

The initial, non-dimensional, vertical, growth rate of a KH billow at its centre ($dL_b/dt \approx L_b/t = 0.42\ N\ d_z$) was assumed to be constant over the range $0<tN<11$. This assumption was only found to be true when $0<R<1$ (see Figure 34) but still approximately true for $1<R<2$ (see Figure 35). The billows were assumed to be circular so that the rate at which the cross sectional area of the billow (A_c) varies with its radius (r) was $dA_c/dr = 2\ \pi\ r$, where $r = L_b\ /2$. It can be seen in Figure 23 that the billows are not perfectly circular and to assume so would only be approximately true.

If the area of a rectangle (A_e), with dimensions $A_e = H_e\lambda_B$ where H was the vertical height, was equal to A_c so that $dA_c/dt \approx dA_e/dt$ then it would be possible to find the rate at which H_e varied with time dH_e/dt. This rate would be a spatially averaged entrainment rate ($dA_e/dt = \lambda_B\ dH_e/dt \approx\ \lambda_B\ u_e$) which would allow a comparison with Strang and Fernando (2001b). The chain rule was used to obtain dA_c/dt:

$$dA_c/dt = dA_c/dr\ .\ dr/dt \qquad \text{Equation 23}$$

Substituting $dA_c/dr = 2\ \pi\ r$, $dr/dt=(0.42\ N\ d_z)/2$ and $dA_c/dt= \lambda_B\ dH_e/dt$ into Equation 23:

$$\lambda_B\ dH_e/dt = (2\ \pi\ r)\ \ (0.42\ N\ d_z\ /2) \qquad \text{Equation 24}$$

Cancelling terms, rearranging and substituting $dH_e/dt= u_e$ into Equation 24:

$$u_e = 0.42\ \pi\ \ N\ d_z\ r\ \ /\ \lambda_B \qquad \text{Equation 25}$$

The radius varied with time and therefore the spatially averaged entrainment rate will vary with time. This was not compatible with other measurements of entrainment that are not time

dependant. To bypass this problem r_{max}, which was the radius at the non-dimensional time for saturation ($tN \approx 11$), was substituted for r in Equation 25; which gave a maximum entrainment rate $u_{e\,max}$:

$$u_{e\,max} = 0.42\,\pi\ N\,d_z\,r_{max}\ /\lambda_B \qquad \text{Equation 26}$$

Substituting for $r_{max}=(0.42\,d_z\,t\,N)/2$ into Equation 26:

$$u_{e\,max} = 0.42\,\pi\ N\,d_z\,((0.42\,d_z\,t\,N)/2)\,/\lambda_B \qquad \text{Equation 27}$$

And substituting for $tN = 11$ into Equation 28:

$$u_{e\,max} = 0.42\,\pi\ N\,d_z\,((0.42\,d_z\,11)/2)\,/\lambda_B \qquad \text{Equation 28}$$

Cancelling terms and rearranging:

$$u_{e\,max} = 0.97\,\pi\ N\,d_z^2\ /\lambda_B \qquad \text{Equation 29}$$

Given that 0.97 was close to unity:

$$u_{e\,max} \approx\ \pi\ N\,d_z^2\ /\lambda_B \qquad \text{Equation 30}$$

Plotting the non-dimensional entrainment ($u_{emax}\,/\,\Delta U$) versus the bulk Richardson number Ri_B (see Figure 42), showed that $u_{emax}/\Delta U$ varied with Ri_B and followed the trend from Strang & Fernando (2001b), where:

$$Ri_B = g'\,H_2\,/\,\Delta U^2 \qquad \text{Equation 31}$$

The bulk and gradient Richardson numbers are approximately equivalent and exactly equal when R=1, but they are not linearly proportional.

When considering H billows the constant (0.42) in Equation 24 was replaced with 0.14 as the growth rate for H billows was $dL_b/dt \approx L_b/t = 0.14\ N\ d_z$, as shown in Figure 36. The H billows were assumed to reach saturation at $tN \approx 11$. H billows have been shown numerically to grow for longer when compared to KH billows in shear flows (Smyth & Winters, 2003). It was possible that the ISW was limiting the time for growth of the H billows to $tN \approx 11$ and that the time to reach saturation for a Holmboe billow was $tN > 11$. The effect of increasing the time for saturation for H billows would be an increase in $u_{emax} / \Delta U$. Increasing the time for saturation to $tN = 20$ would bring the H billow entrainment rate within the scatter of the KH data in Figure 42. In addition to the uncertainty over the H billows time to reach saturation on an ISW, there were only two experiments where H billows formed on an ISW.

Strang & Fernando (2001b) found that entrainment was independent of Ri_B when Ri_B ($Ri_B < 1.5$; $Ri_g < 0.09$) was small ($E_n = u_e/U \approx 0.024$) which was consistent with Christodoulou (1986). Initially this appeared significant however due to both axis being logarithmic the spread of the data about the line of best fit was not well represented. It can be seen at the higher end of the data set (Figure 42) that the spread of data about the line of best fit was $7Ri_B$. A simplistic measure of error is given by half the spread of the data about the mean. Using this method the error could be estimated to be $3.5\ Ri_B$. Going back to the Ri_B independent data it can be seen that this data only extends through $0.8 < Ri_B < 1.5$. As this regime was only measured across a range of $0.7Ri_B$, the significance of this regime compared to the error as measured here can now be seen to be small. This may go some way to explain why the additional data point from this investigation do not agree with the predicted constant entrainment rate at low Ri_B (when $Ri_B < 1.5$, $u_e/U \approx 0.024$). Rather than choosing the maximum entrainment rate, as shown in Equation 28 where $tN = 11$ was substituted in to represent the radius of the billow at saturation, an average value could be used. For example,

using tN=5 the entrainment rate drops to a value much closer to $u_e/U \approx 0.024$. If we take into account that the billow growth rate was not constant for some billows (growth tailed off toward saturation; as shown in Figure 35), an even lower value of tN could be justified. For example using $tN \approx 4$ brought the H billows down to the expected entrainment value and using $tN \approx 2$ brought the KH billows down to the expected entrainment value ($u_e/U \approx 0.024$).

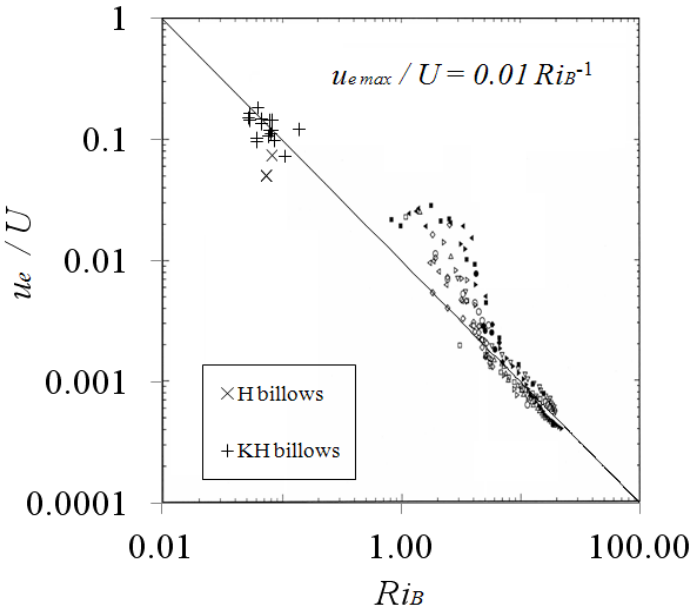

Figure 42 – Excerpt from Strang & Fernando (2001b) The non-dimensional entrainment rate (u_e / U) versus the bulk Richardson number (Ri_B). Solid symbols represent experiments with a two layer stratification and hollow symbols a three layer stratification. Different symbol shapes represent different experiments. Data from this report (3 layer experiments) were overlaid as shown in the legend.

Without the context provided by the previous investigator's data it was difficult to attribute any trend to the data as shown in Figure 43. However the logarithmic trend line that was a fit to Strang & Fernando's (2001b) data shows good agreement.

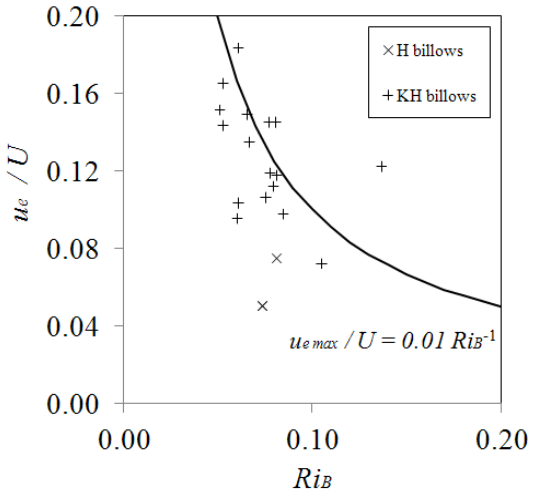

Figure 43 – The non-dimensional entrainment rate (u_e / U) versus bulk Richardson number (Ri_B).

6.1.8 *Mixing and dissipation*

The growth of a KH billow to saturation converted turbulent kinetic energy (*TKE*), to available potential energy (P_A) with very little mixing, whilst the dissipation rate remained near its laminar value (Caulfield & Peltier, 2000). The mixing transiting is known to commence at billow saturation, triggered by three dimensional buoyant secondary instabilities, subsequently spanwise vortex streaks appeared from these instabilities (Peltier & Caulfield, 2003). When streaks from adjacent billows interact the flow will collapse into a turbulent state. At this late time, when the bulk of the mixing takes place, the mixing efficiency (which has varied over the life cycle of the billow) has now settled to a value of 0.2. It was possible to estimate P_A using the assumptions from the previous section:

Given that $A_c = A_e = H_e\lambda_B$, H_e can be found at the time of saturation (H_s) assuming saturation occurs at $tN = 11$.

$$H_S \approx 2.31\ \pi\ d_z^2 \qquad \text{Equation 32}$$

Using the spatially averaged height of a billow at saturation H_S, and making 2 further assumptions it was possible to get a spatially averaged estimate for P_A (see Equation 33):

It was assumed that the density of fluid was evenly distributed within the billow and that the average density of the billow was $\rho_{av} = (\rho_3 - \rho_1)/2$. The datum was assumed to be at the centre of the pycnocline and the spatially averaged billow extended from $z = 0$ to $z = H_S$. Strictly speaking, at saturation, a billow would have extended from $z=0+(H_2/2)$ to $z=H_S+(H_2/2)$.

$$P_A \approx (H_S^2 \rho_{av} g) / 2 \qquad \text{Equation 33}$$

Density profiles from the wake of an ISW, where P_A had completely converted to an increase in background potential energy P_B and internal energy (heat) via dissipation (ϵ), could be compared with P_A at billow saturation. The difference between P_A at billow saturation, and the change in P_B at some late time where $P_A \rightarrow 0$, would give an estimate of ϵ. Unfortunately no measurements in the wake of the ISWs were made during the three layer experiments, due to the constraints of the instruments used at the time. If several measurements were taken, at increasing time intervals in the wake of the ISW, a mixing rate could have been obtained. If the assumption that the mixing efficiency dropped to 0.2 ($\Gamma \approx 0.2$) after the mixing transition, the mixing rate (M) could still be estimated using Equation 34 (Peltier & Caulfield, 2003).

$$\Gamma \approx M / (M+\epsilon) \qquad \text{Equation 34}$$

The dissipation rate is widely accepted to be 0.2 when mixing is taking place, as discussed in section 2.1. Using this rate, the amount of mixing can be estimated to be $0.2P_A$ per square m. In words it was estimated that 20% of the fluid entrained was converted to a gain in potential energy to the background stratification and that 80% of the available potential energy was converted to internal energy (heat). Again applying these assumptions to H billows was inadvisable for the reason given previously.

7 Experimental observations – Two layer stratification

Breaking ISWs in the 2 layer stratification exhibited shear-like behaviour that was heavily distorted (see Figure 44*(a)*); unlike the 3 layer experiments (see Figure 44*(b)*), the billows in the 2 layer experiments could not be clearly distinguished in the shear layer (within the window of observation). Convective breaking in the leading edge of the 2 layer ISWs triggered mixing earlier, compared with the 3 layer ISWs. In turn this caused blurring (due to the refractive index mismatch between layers) of the video stills, making visual observations of the nature of the turbulence difficult and PIV less accurate.

(a) 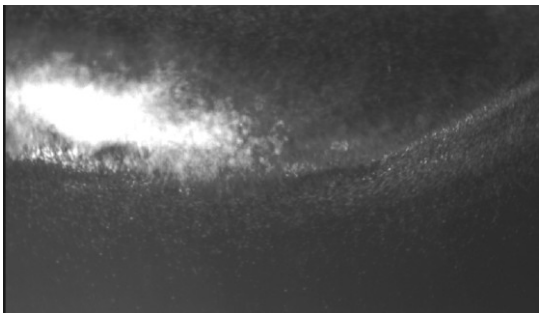 *(b)* 

Figure 44 – (a) The heavily distorted shear layer in a two layer density configuration experiment 221211. (b) K-H billows in a three layer density configuration experiment 141010.

ISWs in the 2 layer stratification exhibited convective breaking, shear breaking or a mixture of both (Figure 45). In most cases periodic KH or H like billows were not observed. It has been proposed that convective breaking triggers instabilities which form shear billows (Carr *et al*., 2008; Helfrich, 2010). This was not easily observed from the fixed location cameras. Experimentally ISWs evolved over the adjustment length, from a block of displaced fluid, which was released from behind the partially submerged gate. The initial behaviour of the ISWs and the initial convective triggering of billows was masked by this evolution. The cameras were positioned downstream of the adjustment length so that ISWs captured would have settled to a quasi steady speed and amplitude.

(a)  (b) 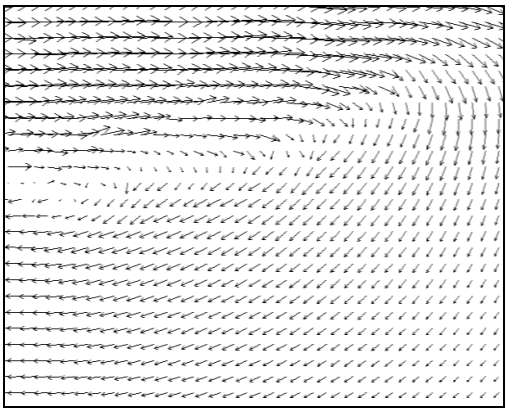

Figure 45 – (a) Shear breaking with convective breaking in a two layer regime, raw image. (b) PIV from the same image. Exp. 050312. Image size 1.45 x/H, 0.97 z/H

For these reasons it was not possible to study the evolution of the turbulence. Instead the change in background *PE* due to the passing of the ISW was analysed to attempt to measure the bulk effect of the passing of the ISW.

7.1 The rotating core

Evidence of rotation in the breaking ISWs was sought, as it had been suggested that convective breaking and the subsequent billows, may become trapped in the ISW; causing the core to rotate (Personal communication: Stuart King, 2013). Non-breaking, large amplitude ISWs were also generated with the expectation that they may also show evidence of rotation in the core that was perhaps being suppressed by shear and/or convective breaking in breaking cases.

7.2 Core behaviour

There has been uncertainty surrounding the behaviour of the ISW core in breaking and non-breaking cases, Figure 46 shows two scenarios discussed in the literature (Carr *et al.*, 2008). The following sections report the various techniques used to try and verify this behaviour. The initial indications, from visual inspection did not support the concept of a rotating core. The seeding in the fluid within the core appeared to move along with the ISW at the wave

speed (Figure 46*(b)*). However the eye does not necessarily pick up on small deviations in velocity while in a fixed (Eulerian) frame of reference.

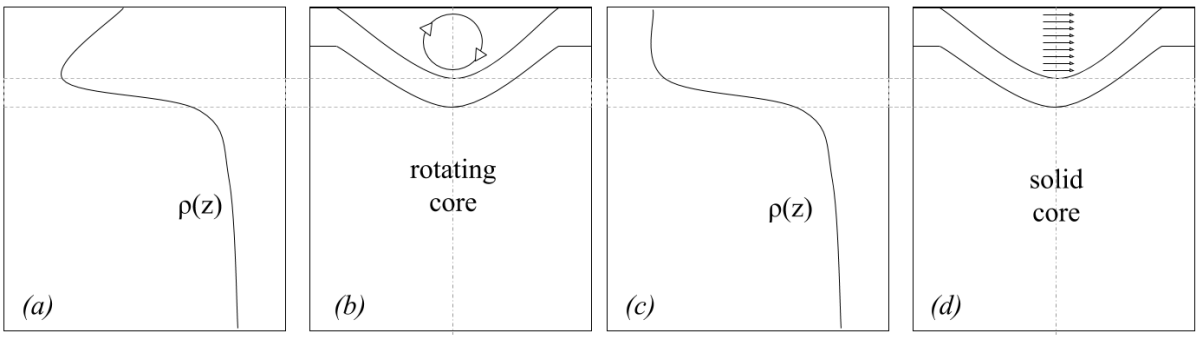

Figure 46 – schematic density profiles and core behaviour one would expect from a rotating core (a-b) and a solid or non-rotating core (c-d) taken through the centre of the ISW (dashed dotted vertical line).

PIV was more sensitive than the eye to small changes in velocity. Vertical velocity profiles (taken through the ISW peaks), generated using the PIV techniques available within Digiflow, did not detect a rotating core. A Typical experimental velocity profile taken through the ISW peak can be seen in Figure 47; the indications of a rotating core were not present as discussed below.

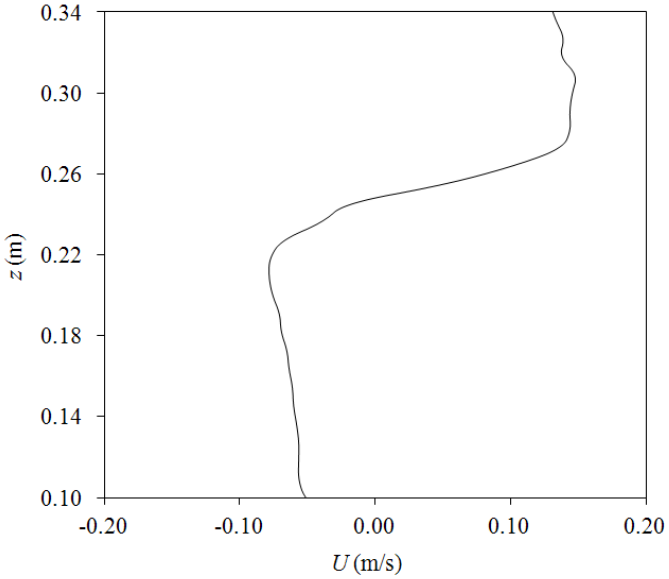

Figure 47 – The horizontal component of velocity (u) versus depth (z) for experiment 240112.

The presence of a rotating core could have been revealed by deviations from the typical ISW velocity profile (Figure 48*(a)*). The horizontal velocities associated with rotation within the

core (Figure 48*(b)*) would be expected to distort the typical velocity profile, as shown in Figure 48*(c)*. Vertical velocity profiles showing this distortion were not found; see Figure 47 for a typical experimental profile. If however the velocity field within the core was sufficiently weak, the distortion would not be distinguishable from the experimental noise in the velocity data.

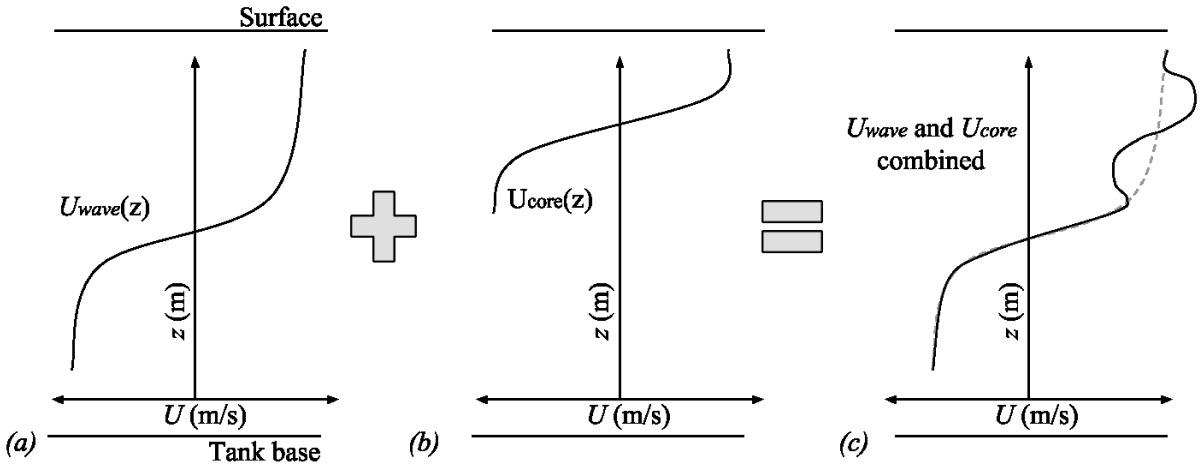

Figure 48 – Schematic representation of superposition of the (a) horizontal wave velocity at the wave peak, (b) the horizontal velocity associated with a rotating core (also taken at the wave peak) and (c) resulting vertical profile of horizontal velocity.

Numerical studies (Carr *et al*., 2008; Helfrich, 2010) predict density inversions in the core of the ISW, where fluid from the pycnocline was entrained and rotated to a position where it was not statically stable. In this laboratory study, density profiles taken at various locations through the ISW do not show density inversions that one would expect to see with a rotational core type ISW. For example, it can be seen in the second and third profiles from the left in Figure 50, that no large scale density inversions were present; this was typical.

No evidence to support the existence of an ISW with a rotational core was found visually, in the density profiles taken through the peak of the ISWs, in the velocity field from experiments exhibiting breaking and from experiment with no breaking. It was possible that the conditions required to trigger a rotating core were not present in these laboratory

experiments and that it was still possible to produce a rotating core type ISW by expanding the range of the experimental parameters. In the oceans, for example, high surface shear (wind) or transverse currents may trigger the rotating core; these effects were not considered in the experiments. It was possible that the scale of the experiment was suppressing the rotation. Perhaps the time scale was not sufficiently long for the rotation to develop; this was likely true and will be discussed later.

7.3 Density profiles

Profiles were obtained in the stable stratification, prior to the partially submerge gate being released, within the ISW and in the wake of the ISW (approximately 1 wavelength behind the ISW). Averaging profiles from several sensors gave a reliable measurement of the stable profile; a typical profile can be seen in Figure 49.

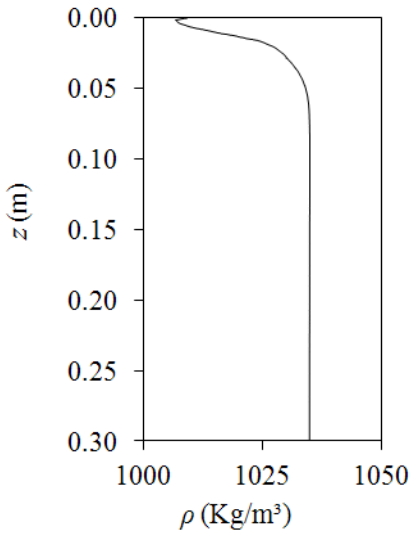

Figure 49 – Density variation with depth, stable stratification from experiment 240112.

It was not appropriate to average the profiles taken during an ISW's passing (Figure 50). Density inversions can be seen in the profiles but they could not be visually associated with a distinct turbulent structure e.g. a KH or H billow.

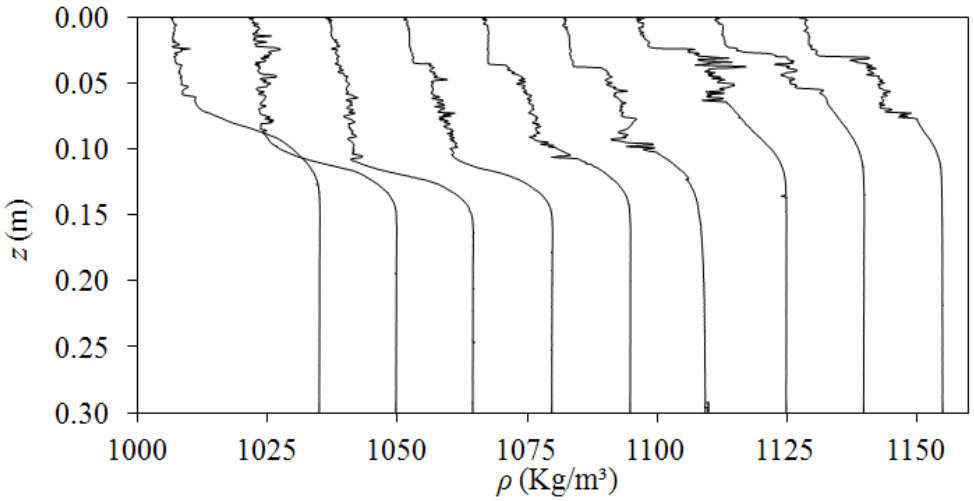

Figure 50 – Density variation with depth, density profiles taken during the passing of an ISW, experiment 240112. Profiles were offset by 15kg/m^3.

Profiles that were taken in the wake of the ISW (see Figure 51) can be seen to have a trailing block of light fluid near the surface, with a density matching that of the fluid released from behind the gate. If more time had passed (given a longer tank), between the ISW passing and the sampling of the density profile in the wake, it was thought that this trailing volume would not have been present. It can also be seen that the remaining density inversions were small, demonstrating that the majority of transfer of P_A to P_B and ϵ was complete. The profiles taken from the wake exhibited enough similarity to justify using an averaged profile.

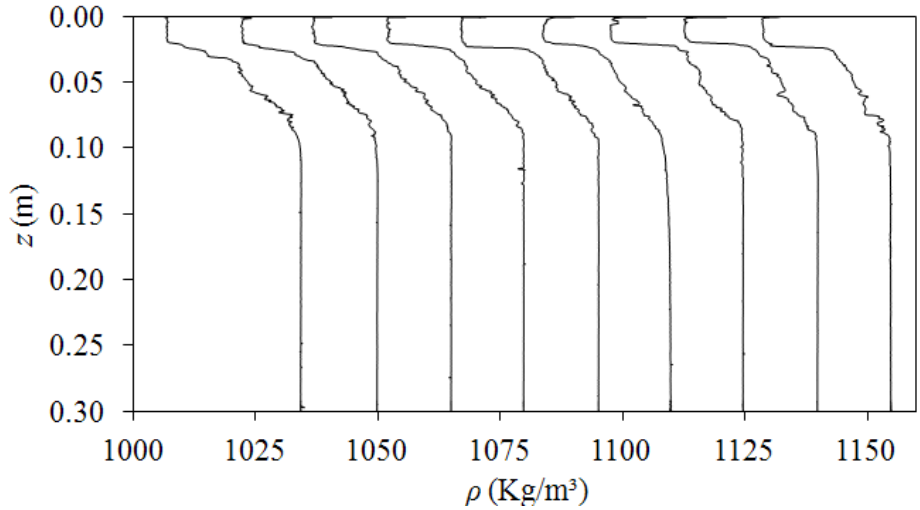

Figure 51 – Density variation with depth in the wake from experiment 240112. Profiles were offset by 15kg/m^3.

Having an average profile to represent the vertical density stratification before and after the ISWs passing, in each case where $P_A \approx 0$ and $P \approx 0$, allows the change in background potential energy to be estimated. It can be seen in Figure 52*(a)* that the raw profiles show a large loss of P_B; this was typical of all the experiments. Normally in stratified mixing an increase in P_B would be expected (Winters, 1995; Strang & Fernando, 2001a , 2001b), because it is assumed that a local balance of P to B and ϵ was present ($P=B+\epsilon$). Given a loss of P_B ($B=P_A+P_B$; $B=P_B$ when $P_A \approx 0$) and that $\epsilon > P$ is not possible, we must assume that a local balance of energy was not present in the 2 layer experiments. Adjusting the profiles to take account of the afore mentioned trailing volume (Figure 52*(b)*) removes the bias involved in using a relatively short (~6m) wave tank. P_B was calculated over the region shown in Figure 52*(c)*.

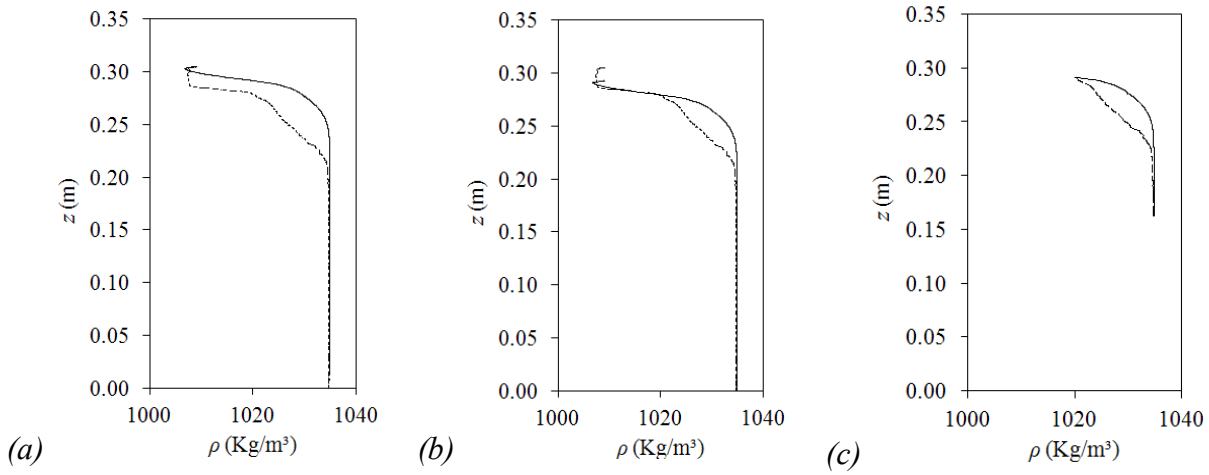

Figure 52 – Density variation with depth from experiment 240112, where the solid line represented the averaged stable profile and the dashed line represented the averaged profile in the wake of the ISW and where (a) shows the raw averaged profiles, (b) the realigned profile removing the bias given by the trailing volume and (c) the region over which the change in P_B was calculated.

8 Experimental findings – Two layer stratification

In contrast to the three layer experiments, in the two layer experiments, distinct, billow like structures were not observed; consequently a different approach was taken to represent the breaking process. Instead the change in background potential energy (P_B) to the stratification, that resulted from the passing of a breaking ISW, was found. In all cases the background potential energy experienced a loss of energy due to the ISWs passing. This was an unexpected result, it implied that there was not a local balance of production (P) of turbulent kinetic energy (TKE) to dissipation (ϵ) and buoyancy flux ($B=P_A+P_B$). Globally, there should have been a net energy balance over the whole domain of the experiment; unfortunately the sampling window did not encompass enough of the domain to estimate net values.

The percentage change in P_B ($\%\Delta P_B$) was measured in the wake of the ISW some distance from the ISW peak. It can be seen in Figure 53 that the percentage change in P_B remained relatively constant across all experiments. The non-dimensional time tN=0 corresponded with an ISW's peak passing the sensors. Increasing tN represents increasing non-dimensional time until P_B was re sampled in the ISW's wake (marked with the 'x' symbol). The loss of P_B was only apparent in the breaking ISWs. The absence of a local energy balance implied that the entrained fluid must have been trapped within the core of the ISW, indicating that the two layer breaking ISWs produced in this data set were indeed transitioning to the rotating core type ISW. It can be seen that the loss of P_B was approximately 0.5%. This corresponded to a non-dimensional layer depth increase of $\Delta H_1/H_1$ =0.025±0.015. This was interesting as typically a mixing event would be assumed to decrease H_1. Within the experiments shown in

Figure 53 there were a range of gradient Richardson numbers (Ri_g), non-dimensional ISW amplitudes (a/H_2) and ratios of velocity to density interfacial thicknesses (R).

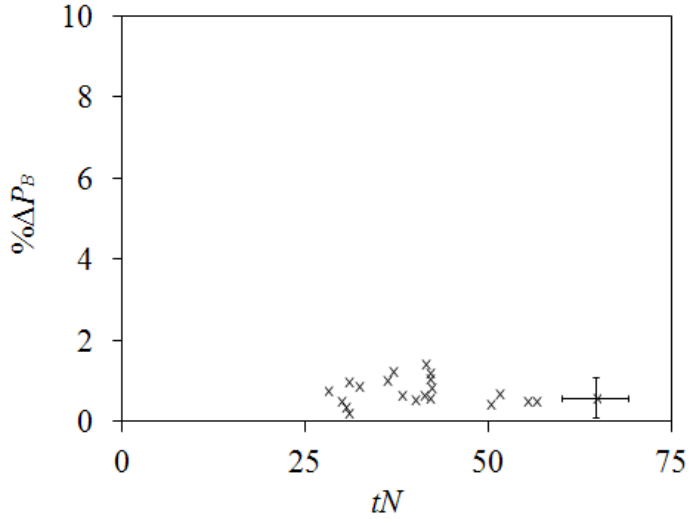

Figure 53 – The percentage decrease of background potential energy ($\%\Delta P_B$) (ratio of P_B before and after the waves passing) versus tN for all the two layer experiments, parameter can be found in Appendix I. Bars show the estimated error.

The $\%\Delta P_B$ in the three layer experiments was found to be dependent on the characterisitic Richardson number, it can be seen in Figure 54 that no dependence on Ri_g was present in the two layer experiments. More data in the region $0.75<Ri_g<2$ would allow the dependence of mixing, on Ri_g, to be ascertained with more certainty.

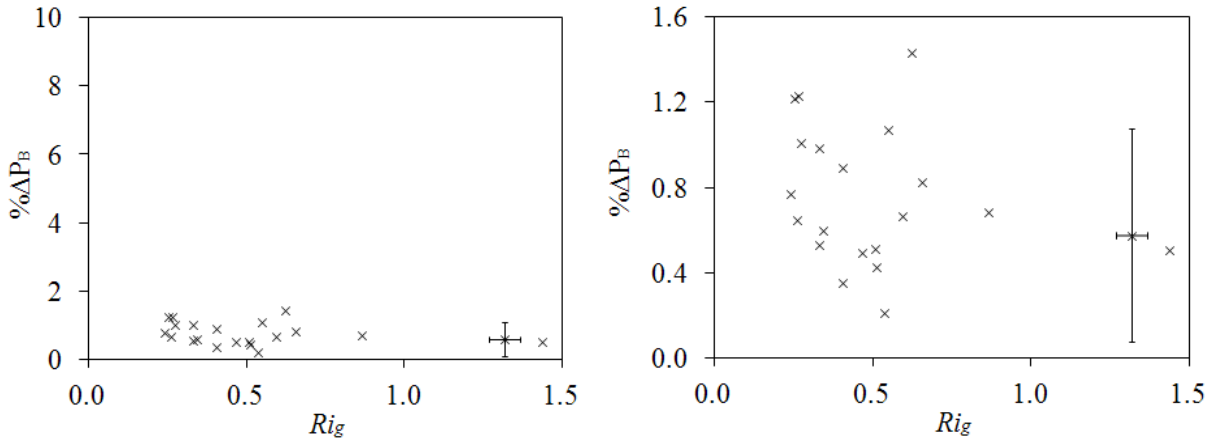

Figure 54 – The percentage decrease of background potential energy ($\%\Delta P_B$) (ratio of P_B before and after the waves passing) versus Ri_g for all the two layer experiments, parameter can be found in Appendix I. Bars show the estimated error.

The ratio of velocity and density interfacial thicknesses (R), was also found to be an important parameter in the three layer experiments. Again it can be seen in Figure 55 that no dependence on R was apparent in the data for the two layer experiments.

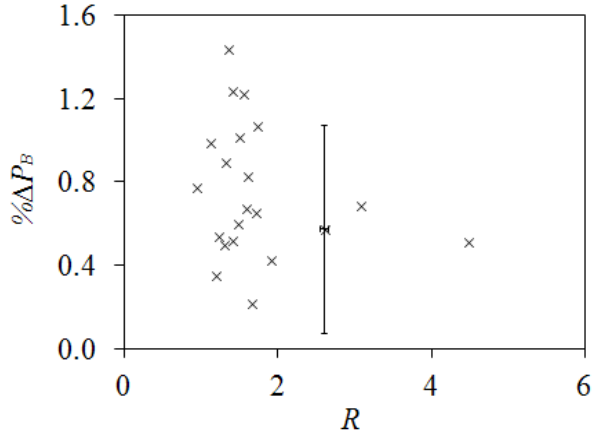

Figure 55 – The percentage decrease of background potential energy ($\%\Delta P_B$) (ratio of P_B before and after the waves passing) versus R for all the two layer experiments, parameter can be found in Appendix I. Bars show the estimated error.

The $\%\Delta P_B$ did not show any dependence on the non-dimensional ISW wave amplitude (a/H_2) as shown in Figure 56. In general because $\%\Delta P_B$ was small compared to the estimated error on the measurement of $\%\Delta P_B$, it was difficult to find any trend in the data.

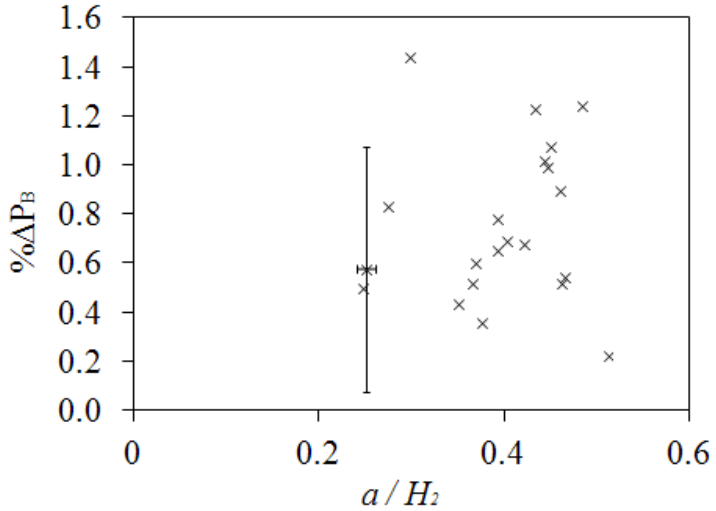

Figure 56 – The percentage decrease of background potential energy ($\%\Delta P_B$) (ratio of P_B before and after the waves passing) versus a/H_2 for all the two layer experiments, parameter can be found in Appendix I. Bars show the estimated error.

9 Conclusion

9.1 Three layer

Instabilities were found to grow from various positions around the ISW peak. For this reason it was considered best to characterise billow growth from the time of inception of a billow, rather than from a fixed position on the ISW. Billows with the same initial conditions (i.e. on the same ISW from approximately the same position on the ISW) were found to be self-similar with respect to billow speed, vertical growth rate and the maximum vertical extent (within the experimental error of the measurements and the limited number of billows sampled per ISW). It was not possible to reliably measure billow width. The non-dimensional Thorpe scale L_T/L_b measured through the centre of the billows was comparable to L_T/L_b ratios measured in the field and in other experimental studies in horizontal shear flows.

The interaction of Kelvin Helmholtz billows and the parent ISW did not modify the vertical growth rate, height at saturation, speed, wavelength or the non-dimensional Thorpe scale of the billows when compared to Kelvin Helmholtz billows that had formed on horizontal parallel shear flows. This was most evident in the non-dimensional vertical growth rate of a billow. Parameters of the shear flow at the ISW peak successfully collapsed the growth rates of billows onto one of three curves. It was evident that the conditions at inception, i.e. in the peak of the ISW, set the billows subsequent behaviour.

It was possible that the time required for a Holmboe billow to reach its maximum vertical extent and the time required for an ISW to pass a Holmboe billow ($tN \approx 20$) were close enough to limit the growth of a Holmboe billow, i.e. the shear would be removed from the billow

before it reached its maximum vertical extent. More experiments would be required to fully gauge the ISW's effect on a Holmboe billow, as only two such experiments were performed.

Experimentally R, the ratio of velocity and density interfacial thicknesses, has been shown to be an important factor for the first time (to the author's knowledge). For the range of parameters investigated, 3 types of billows were observed which were conveniently separated by the parameter R.

$0<R<1$: A 'confined' (see section 6.1.3), asymmetric (see section 6.1.6), Kelvin Helmholtz billow was found in this regime. The growth rate did not have the classic (see section 6.1.3) slowing down (at $t \approx 6tN$) in the later stages of billow evolution that was observed in this and other studies when R was in the range $1<R<2$ (De Silva *et al*., 1996).

$1<R<2$: The classic 'unconfined' (see section 6.1.3), asymmetric (see section 6.1.6), Kelvin Helmholtz type billow was found in this regime. The growth rate, of the vertical extent of the billows, slowed down in the later stages of evolution (when $t>6tN$; see section 6.1.3). Billows in this regime compared favourably with previous studies of Kelvin Helmholtz billows in horizontal shear flows.

$R>2$: Asymmetric (see section 6.1.6) Holmboe billows were found to grow in this regime. Smyth & Winters (2003) have suggested that Holmboe billows can attain much larger amplitudes than Kelvin Helmholtz billows. This was not observed, leaving some doubt over whether Holmboe billows growing on an ISW attain their maximum amplitude.

It should be noted that the actual R range investigated was $0.6<R<2.2$. It was presumed that no regime change was present between $0<R<0.6$ and that no regime change was present between $2.2<R<\infty$, because the expected regime changes have occurred within the range $0.6<R<2.2$. For this reason the more convenient bracketing $0<R<1$; $1<R<2$; $R>2$ was adopted.

The 3 different types of instabilities had 3 different maximum vertical extents. An attempt to compare the rate of entrainment was hampered by the 3 different maximum vertical extents of the 3 different billow types. A worst case estimate compared favourably with the trend line fit to Strang & Fernando's (2001b) data; previously it was thought that mixing deviated from this trend at low Richardson numbers.

The vertical growth rates of billows were found to scale with the velocity interface thickness d_z and the buoyancy frequency N, associated with the interfacial layer, implying that d_z set the vertical extent of billows and that N set the time scale for that growth. Other studies (De Silva *et al*., 1996) found that the billow wavelength λ_B successfully scaled (i.e. collapsed the data) the vertical growth rate. It was found in this study that d_z was linearly proportional to λ_B going someway to explaining why both scalings appeared to collapse the data. Several authors (Thorpe, 1971; Koop & Browand, 1979; Fructus *et al.*, 2009) have found that the billow wavelength was approximately proportional to the velocity interfacial thickness ($\lambda_B \approx k\, d_z$, where $1.5<k<7.9$). Although not proven, it appeared that this relationship was sensitive to the type of experimental setup. It may have been that the choice of experimental setup had a systematic effect on the asymmetry of the flow and consequently λ_B.

It was found that a billow's speed was related to the wave speed via the billow's asymmetry, (see section 6.1.6) and that this characterised billow speed over a larger range than previous estimates (Fructus *et al.,* 2009; see Figure 41).

Many authors (Holmboe, 1962; Baines & Mitsudera, 1994; Caulfield, 1994; Smyth & Winters, 2003; Carpenter *et al*., 2010), utilising linear stability analysis, have demonstrated that Ri_c cannot be a sufficient criterion for breaking as it does not characterise the behaviour of Holmboe billows. It has been shown that it was possible to produce asymmetric Holmboe billows on an ISW. The Richardson number for these billows was Ri_g>0.25. The often quoted critical Richardson number Ri_c<0.25, did not correctly predict the limit for breaking in these experiments as it only characterises Kelvin Helmholtz instabilities when the scale ratio, R=1 and the asymmetry a_s=0 (Taylor, 1931; Miles, 1961; Howard 1961).

9.2 Two layer

Distinct turbulent structures were not apparent in most cases. An individual billow's evolution could not be observed visually; consequently the associated density profiles were difficult to interpret given their lack of context. Convective instabilities were thought to trigger the formation of billows (personal communication: King, 2013) on the front of ISWs leading to a disorganised turbulent patch in the ISW peak.

The development of the ISW towards a steady state rotating core was not observed despite efforts to generate it. It can be seen that with an inviscid 2D numerical model, it was possible to produce a rotating core type ISW (personal communication: King, 2014) given similar experimental parameters to those used in this thesis (Figure 57; credit for the DNS simulation goes to Dr. Stuart King). The only evidence that the ISWs were developing to the rotating

core was found by comparing the background *PE* before and after an ISW's passing. An approximate 1% loss of *PE* from the background stratification to the ISW demonstrated the absence of a local energy balance, and that the ISW must gain energy from the background via entrainment.

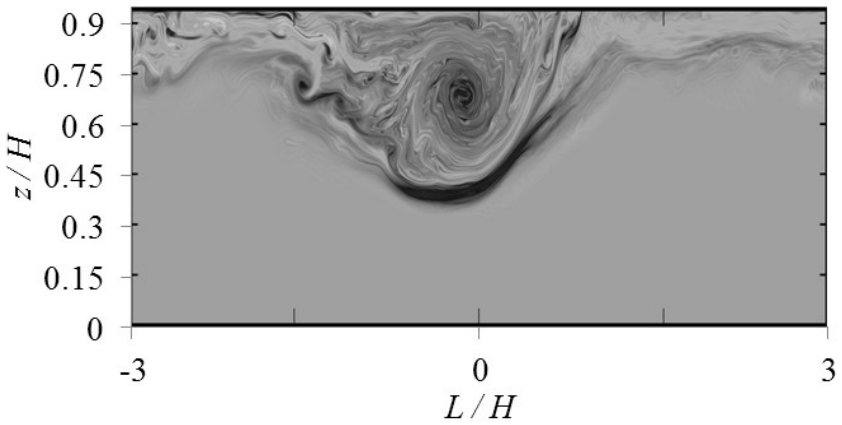

Figure 57 – Vorticity field of a rotating core, where H_1/H_2 = 0.11, tN≈300. Darker colour represents stronger vorticity.

Two important experimental conditions were required that would allow a rotating core ISW to fully develop. Firstly, there could be absolutely no mixing at the surface before an experiment ran, echoing the results of Lamb (2002). Figure 58 (credit for the DNS simulation goes to Dr. Stuart King) shows the typical result of mixing the top 2% of the vertical domain; no rotating core develops. In the laboratory this part of the stratification was sensitive to disturbances generated while filling the tank, the numerical 2% *z/H* was the dimensional equivalent of 5mm water depth. The first few millimetres of stratification were not reliably measured in the laboratory due to the nature of the conductivity sensors. As the sensors passed from touching the surface of the water to a position where they were partially submerged (typically the first 3mm of a strike), the sensors produced a spike in conductivity due to the rapid change in environment (air to water), a known issue with the instrument. Guaranteeing that any of the experiments did not have a thin mixed layer at the surface was not possible, although great care was taken.

The second important condition was that sufficient time was allowed for the rotating core to develop. This was 300*tN* in the numerical experiment shown, the experimental equivalent was 100 seconds or taking an average wave speed, 30m of tank. Clearly this was not possible in the laboratory, the tank was 6.4m in length and had an effective working length of 5m. An additional factor in the numerical experiment was that the horizontal boundary condition was periodic. Meaning that, even thought the domain was quite wide, eventually the ISW had to travelled through density inversions from collapsed billows and fossil turbulence (Gibson, 1980) that had travel across the whole domain. One could argue that an ISW propagating into a previously turbulent stratification would be more representative of oceanic conditions, however the stratification in the laboratory was quiescent. It was felt that encountering the previously turbulent stratification in the numerical model brought about the transition to a rotating core more quickly because it triggered convective instabilities.

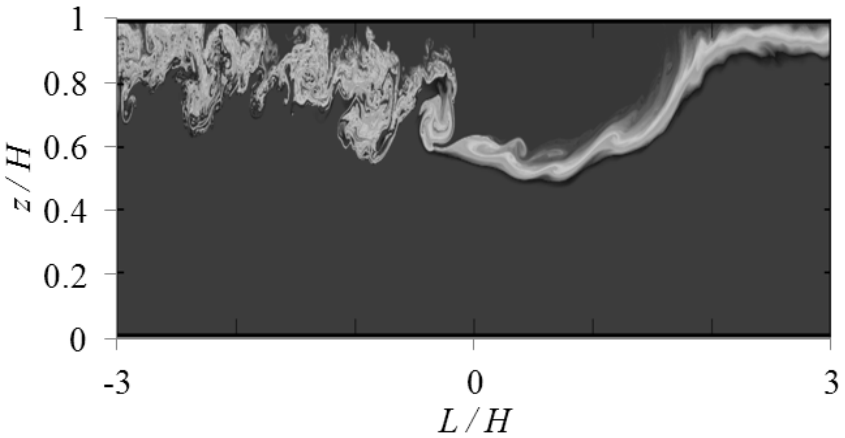

Figure 58 – Buoyancy field of a non rotating core, where H_1/H_2 = 0.11, tN≈170 and top 2% of the vertical domain was well mixed.

9.3 Implications for entrainment and mixing

It was clear that ISWs developing to the rotating core type ISW, in a two layer stratification, behaved very differently when compared to ISWs in a three layer stratification. There cannot be a blanket value of entrainment and mixing for both types of ISWs. The two layer rotating

core type ISWs were transitioning to the rotating core within the observational window. Although estimates of entrainement were made they do not apply to the steady state rotating core, making them of limited use. As previously discussed the ISWs in this regime appeared to collect *PE* through entrainment from the background stratification. But they may have also been returning energy to the background via mixing. It was not possible to separate these processes. No estimate for entrainment or mixing can be offered for those reasons. Estimating entrainment and mixing would be more appropriate and useful, if the rotating core type ISW had developed to a quasi-steady state.

It was possible to estimate entrainment per billow wavelength for ISWs, in a three layer stratification. This was achieved by obtaining a scaling for the maximum vertical extent of billows. Firstly given the ratio of velocity and density interfacial thicknesses R, the type of instability that was likely to appear on an ISW could be estimated. Following this step, if the buoyancy frequency N was known, a worst case or maximum rate estimate for the entrainment could be made. Assuming that the mixing efficiency was 0.2 after the mixing transition, the amount of mixing could be estimated to be 20% of the entrainment.

9.4 Caveats

The presence of side walls in the laboratory prevents vortex stretching from taking place and is known to induce an unnatural bulging of the billows (Thorpe, 1973). Vortex stretching balanced by viscosity would likely prolong the life of a Kelvin Helmholtz or Holmboe billow in an unbounded (laterally) domain creating significantly different behaviour at the point of collapse. It is possible that billows on an unbounded ISW may warp along their longitudinal axis to form hairpin vortices, increasing the billows length per meter width of ISW and therefore increase the mixing per unit width.

Vortices from the lead ISW (in a train of ISWs) may seed subsequent ISWs with vorticity or fossil turbulence (Gibson 1986). This may result in billows forming on the leading edge of subsequent ISWs via convective instability (even in a three layer regime). These convective billows may have wavelengths that would not be well predicted by linear stability analysis (as the billows did not grow from the fastest growing perturbation). Furthermore, if billows are grown from convective instabilities on the front of an ISW, the extra time for growth (compared to billows that grow from the wave peak) could generate more frequent pairing of billow and greater mixing.

The gradient Richardson number was calculated using the undisturbed upstream density profile, whereas ideally it would be calculated with the density profile measured at the ISW peak. Thickening or thinning of the density interface (H_2) at the ISW peak can occur, it may also be distorted by the billows forming. The effect was thought to be minor.

9.5 Future work

The refractivity-matched LIF technique used in De Silva *et al*. (1996), expanded over a greater parameter range in combination with PIV, would produce density and velocity field measurements that would give a fuller and clearer picture of billow evolution on an ISW. The method would also provide improved estimates of the contribution to mixing that each billow makes. A 3D numerical simulation would provide the same information and with more control over the initial conditions.

If one was to repeat the experiments in this study it would be useful to measure the increase to the background *PE* due to the breaking ISW in the 3 layer stratification, as this could be related to the type, size and frequency of billow.

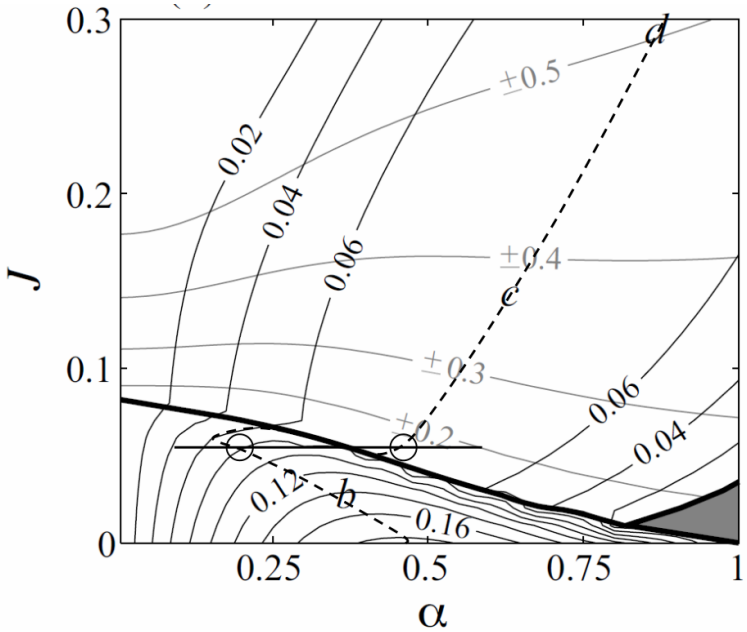

Figure 59 – Stability diagram (from Carpenter et al., 2010)in terms of the bulk Richardson number J and the dimensional perturbation wave number for constant scale ratio R (R=5). Dark contours are growth rates. Dashed dark line is peak growth rate and the grey contours are phase speed.

It is argued by some (Carpenter *et al*., 2010) that there is a smooth transition from Kelvin Helmholtz to Holmboe instability. Currently this has not been established experimentally. It is possible that no such transition exists and that Kelvin Helmholtz and Holmboe instabilities can appear simultaneously on an ISW given the right conditions. ISWs lose amplitude very slowly, which in turn slowly varies shear. Given a long flume, an ISW may pass through the transition from Kelvin Helmholtz instabilities to Holmboe instabilities. At the transition, the opportunity for both KH and H billows to appear on the same ISW will be present. Figure 59 from Carpenter *et al*. (2010), with additional lines from the author, shows that for the same Richardson number there are Kelvin Helmholtz and Holmboe instabilities with the same growth rate. In the figure, α is the non-dimensional wave number of perturbations

($\alpha=k\lambda_B/2d_z$) and J is the bulk Richardson number (Ri_B). Given that the two instabilities have the same growth rate it is feasible that they could appear on the same ISW at the same time.

10 References

AGHSAEE, P., BOEGMAN, L. & LAMB, K. G. 2010. Breaking of shoaling internal solitary waves. *Journal of Fluid Mechanics,* 659, 289-317.

APEL, J.R., BADIEY, M., CHING-SANG CHIU, FINETTE, S., HEADRICK, R., KEMP, J., LYNCH, J.F., NEWHALL, A., ORR, M.H., PASEWARK, B.H., TIELBUERGER, D., TURGUT, A., VON DER HEYDT, K. & WOLF, S. 1997. An overview of the 1995 SWARM shallow-water internal wave acoustic scattering experiment. *Oceanic Engineering*, 22, 3, 465-500.

APEL, J. R., PRONI, J. R., BYRNE, H. M. & SELLERS, R. L. 1975. Near-simultaneous observations of intermittent internal waves on the continental shelf from ship and aircraft. *Geophysical Research Letters*, 2, 128-131.

BAINES, P. G. & MITSUDERA, H. 1994. On the mechanism of shear flow instabilities. *Journal of Fluid Mechanics,* 276, 327-342.

BARAD, M. F. & FRINGER, O. B. 2010. Simulations of shear instabilities in interfacial gravity waves. *Journal of Fluid Mechanics,* 644, 61-95.

BENJAMIN, T. B. 1966. Internal waves of finite amplitude and permanent form. *Journal of Fluid Mechanics,* 25, 241-270.

BERNAL, L. P. & ROSHKO, A. 1986. Streamwise vortex structure in plane mixing layers. *Journal of Fluid Mechanics,* 170, 499-525.

BREIDENTHAL, R. 1981. Structure in turbulent mixing layers and wakes using a chemical reaction. *Journal of Fluid Mechanics,* 109, 1-24.

BROWN, G. L. & ROSHKO, A. 1974. On density effects and large structure in turbulent mixing layers. *Journal of Fluid Mechanics,* 64, 775-816.

BOUSSINESQJ, J. V. **1877** Essai **sur** la thhorie des eaux courantes. *Me'm. prksentis par divers Savants* ci *L'Acad. Sci. Inst. France (shies* **2) 23, 1-680** (see also **24, 1-64).**

CAMASSA, R. & VIOTTI, C. 2012. On the response of large-amplitude internal waves to upstream disturbances. *Journal of Fluid Mechanics,* 702, 59-88.

CARPENTER, J. R., BALMFORTH, N. J. & LAWRENCE, G. A. 2010. Identifying unstable modes in stratified shear layers. *Physics of Fluids,* 22, 054104-13.

CARPENTER, J. R., LAWRENCE, G. A. & SMYTH, W. D. 2007. Evolution and mixing of asymmetric Holmboe instabilities. *Journal of Fluid Mechanics*, 582, 103–132.

CARPENTER, J. R., TEDFORD, E. W., HEIFETZ, E. & LAWRENCE, G. A. 2013. Instability in Stratified Shear Flow: Review of a Physical Interpretation Based on Interacting Waves. *Applied Mechanics Reviews,* 64.

CARR, M., FRUCTUS, D., GRUE, J., JENSEN, A. & DAVIES, P. A. 2008. Convectively induced shear instability in large amplitude internal solitary waves. *Physics of Fluids,* 20, 126601.

CARR, M., KING, S. E. & DRITSCHEL, D. G. 2011. Numerical simulation of shear-induced instabilities in internal solitary waves. *Journal of Fluid Mechanics,* 683, 263-288.

CARR, M., KING, S. E. & DRITSCHEL, D. G. 2012. Instability in internal solitary waves with trapped cores. *Physics of Fluids,* 24.

CAULFIELD, C. P. & PELTIER, W. R. 2000. The anatomy of the mixing transition in homogeneous and stratified free shear layers. *Journal of Fluid Mechanics,* 413, 1-47.

CAULFIELD, C. P. 1994. Multiple linear instability of layered stratified shear flow. *Journal of Fluid Mechanics,* 258, 255-285.

CHRISTODOULOU, G. C. 1986. Interfacial mixing in stratified flows. *Journal of Hydraulic Research*, 24, 77-92.

COOK, R. D. 1979. Influential Observations in Linear Regression. *Journal of the American Statistical Association,* 74, 169-174.

CORCOS, G. M. & SHERMAN, F. S. 1976. Vorticity concentration and the dynamics of unstable free shear layers. *Journal of Fluid Mechanics,* 73, 241-264.

DALZIEL, S. B. 2006. *DigiFlow Users Guide* [Online]. Available: http://www.dalzielresearch.com/digiflow/digiflow.htm [Accessed 06/05/2014 2014].

DALZIEL, S. B., CARR, M., SVEEN, J. K. & Davies, P. A. 2007. Simultaneous synthetic schlieren and PIV measurements for internal solitary waves. *Measurement Science and Technology,* 18, 533.

DAVIS, P. A. & PELTIER, W. R. 1979. Some characteristics of the Kelvin-Helmholtz and resonant overreflection modes of shear flow instability and of their interaction through vortex pairing. *Journal of the Atmospheric Sciences*, 36, 2395.

DE SILVA, I. P. D., FERNANDO, H. J. S., EATON, F. & HEBERT, D. 1996. Evolution of Kelvin-Helmholtz billows in nature and laboratory. *Earth and Planetary Science Letters,* 143, 217-231.

DIAMESSIS, P. J. & REDEKOPP, L. G. 2006. Numerical investigation of solitary internal wave-induced global instability in shallow water benthic boundary layers. *Journal of Physical Oceanography*, 36, 784–812.

DILLON, T. M. 1982. Vertical overturns: A comparison of Thorpe and Ozmidov length scales. *Journal of Geophysical Research: Oceans,* 87, 9601-9613.

DJORDJEVIC, V. D. & REDEKOPP, L. G. 1978. The Fission and Disintegration of Internal Solitary Waves Moving over Two-Dimensional Topography. *Journal of Physical Oceanography,* 8, 1016-1024.

DRAZIN, P.G. & HOWARD, L.N. 1966. Hydrodynamic stability of parallel flow of an inviscid fluid. *Advances in Applied Mechanics*, 9, 1–89.

DUDA, T. F., LYNCH, J. F., IRISH, J. D., BEARDSLEY, R. C., RAMP, S. R., CHING-SANG, C., TSWEN YUNG, T. & YANG, Y. J. 2004. Internal tide and nonlinear internal wave behavior

at the continental slope in the northern south China Sea. *IEEE Journal of Oceanic Engineering,* 29, 1105-1130.

ECONOMIDOU, M. & HUNT, G. R. 2009. Density stratified environments: the double-tank method. *Experiments in Fluids,* 46, 453-466.

EILBECK, C. 2013. *John Scott Russell and the solitary wave* [Online]. Available: http://www.macs.hw.ac.uk/~chris/scott_russell.html. [Accessed 11/04/2014].

FARMER, D. & ARMI, L. 1999. The Generation and Trapping of Solitary Waves over Topography. *Science,* 283, 188-190.

FERNANDO, H. J. S. 1991. Turbulent Mixing In Stratified Fluids. *Annual Review of Fluid Mechanics,* 23, 455-493.

FERRON, B., MERCIER, H., SPEER, K., GARGETT, A. & POLZIN, K. 1998. Mixing in the romanche fracture zone. *Journal of Physical Oceanography*, 28, 1929–1945.

FOCHESATO, C., DIAS, F. & GRIMSHAW, R. 2005. Generalized solitary waves and fronts in coupled Korteweg–de Vries systems. *Physica D: Nonlinear Phenomena,* 210, 96-117.

FORTUIN, J. M. H. 1960. Theory and application of two supplementary methods of constructing density gradient columns. *Journal of Polymer Science,* 44, 505-515.

FRUCTUS, D., CARR, M., GRUE, J., JENSEN, A. & DAVIES, P. A. 2009. Shear-induced breaking of large internal solitary waves. *Journal of Fluid Mechanics,* 620, 1-29.

FU, L. L. & HOLT, B. 1982. *Seasat Views Oceans and Sea Ice with Synthetic Aperture Radar*, Jet Propulsion Laboratory Publication, 81-120.

GALBRAITH, P. S. & KELLEY, D. E. 1996. Identifying Overturns in CTD Profiles. *Journal of Atmospheric and Oceanic Technology,* 13, 688-702.

GARDNER, C. S., GREENE, J. M., KRUSKAL, M. D. & MIURA, R. M. 1967. Method for Solving the Korteweg-deVries Equation. *Physical Review Letters,* 19, 1095-1097.

GEYER, W. R. & SMITH, J. D. 1987. Shear Instability in a Highly Stratified Estuary. *Journal of Physical Oceanography,* 17, 1668-1679.

GIBSON, C. H. 1980. *Fossil temperature, salinity, and vorticity turbulence in the ocean, in Marine Turbulence*, Nihoul, J. (Ed.), Elsevier Publishing Co.

GIBSON, C. H. 1986. Internal waves, fossil turbulence, and composite ocean microstructure spectra. *Journal of Fluid Mechanics*, 168, 89-117.

GIBSON, C. H., NABATOV, V. & OZMIDOV, R. 1993. Measurements of turbulence and fossil turbulence near ampere seamount. *Dynamics of Atmospheres and Oceans,* 19, 175-204.

GILL. A, E. 1982. *Atmosphere-ocean dynamics*, Academic Pr.

GOFF, M., JEANS, G., HARRINGTON-MISSIN, L. & BASCHENIS, C. 2010. Soliton Early Warning system for Offshore Applications. *Oceanology International 2010*, London, UK. 9-11 March 2010.

GOLDSTEIN, S. 1931. On the Stability of Superposed Streams of Fluids of Different Densities. *Proceedings of the Royal Society of London, Series A,* 132, 524-548.

GREGG, M. C. 1987. Diapycnal mixing in the thermocline: A review. *Journal of Geophysical Research: Oceans,* 92, 5249-5286.

GRUE, J., FRIIS, H. A., EACUTE, PALM, E., RUS, ARING & S, P. O. 1997. A method for computing unsteady fully nonlinear interfacial waves. *Journal of Fluid Mechanics,* 351, 223-252.

GRUE, J., JENSEN, A., RUS, ARING, S, P. & SVEEN, J. K. 1999. Properties of large-amplitude internal waves. *Journal of Fluid Mechanics,* 380, 257-278.

HAIGH, S. P. & LAWRENCE, G. A. 1999. Symmetric and non-symmetric Holmboe instabilities in an inviscid flow. *Physics of Fluids*, A 11, 1459–1468.

HALPERN, D. 1971. Semidiurnal internal tides in Massachusetts Bay. *Journal of Geophysical Research,* 76, 6573-6584.

HAZEL, P. 1972. Numerical studies of the stability of inviscid stratified shear flows. *Journal of Fluid Mechanics,* 51, 39-61.

HEAD, M. J., 1983. *The use of miniature four-electrode conductivity probes for high resolution measurements of turbulent density or temperature variations in salt-stratified water flows* [PhD Thesis]. University of California.

HELFRICH, K. R. & MELVILLE, W. K. 2006. Long nonlinear internal waves. *Annual Review of Fluid Mechanics.*

HELFRICH, K. R. & WHITE, B. L. 2010. A model for large-amplitude internal solitary waves with trapped cores. *Nonlin. Processes Geophys.,* 17, 303-318.

HELFRICH, K. R., MELVILLE, W. K. & MILES, J. W. 1984. On interfacial solitary waves over slowly varying topography. *Journal of Fluid Mechanics,* 149, 305-317.

HILL, D. F. 2002. General density gradients in general domains: the "two-tank" method revisited. *Experiments in Fluids,* 32, 434-440.

HOLMBOE, J. 1962. On the behaviour of symmetric waves in stratified shear layers. *Geophys. Publ.*, 67-113.

HOLT, S. E., KOSEFF, J. R. & FERZIGER, J. H. 1992. A numerical study of the evolution and structure of homogeneous stably stratified sheared turbulence. *Journal of Fluid Mechanics*, 237, 499-539.

HORN, D. A., IMBERGER, J. & IVEY, G. N. 2001. The degeneration of large-scale interfacial gravity waves in lakes. *Journal of Fluid Mechanics,* 434, 181-207.

HOWARD, L. N. & MASLOWE, S. A. 1973. Stability of stratified shear flows. *Boundary-Layer Meteorology,* 4, 511-523.

HOWARD, L. N. 1961. Note on a paper of John W. Miles. *Journal of Fluid Mechanics,* 10, 509-512.

HUNKINS, K. & FLIEGEL, M. 1973. Internal undular surges in Seneca Lake: A natural occurrence of solitons. *Journal of Geophysical Research,* 78, 539-548.

ITSWEIRE, E. C. 1984. Measurements of vertical overturns in a stably stratified turbulent flow. *Physics of Fluids*, 27, 764-766.

ITSWEIRE, E. C., KOSEFF, J. R., BRIGGS, D. A. & FERZIGER, J. H. 1993. Turbulence in Stratified Shear Flows: Implications for Interpreting Shear-induced Mixing in the Ocean. *Journal of Physical Oceanography*, 23, 1508–1522.

JACKSON, D. & LAUNDER, B. 2007. Osborne Reynolds and the Publication of His Papers on Turbulent Flow. *Annual review of fluid mechanics*, 39, 19-35.

JOSEPH, R. I. 1977. Solitary waves in a finite depth fluid. *Journal of Physics A: Mathematical & General,* 10, N.12, 225-227.

KAKUTANI, T. & YAMASAKI, N. 1978. Solitary Waves on a Two-Layer Fluid. *Journal of the Physical Society of Japan,* 45, 674-679.

KAO, T. W., PAN, F. & RENOUARD, D. 1985. Internal solitons on the pycnocline: generation, propagation, and shoaling and breaking over a slope. *Journal of Fluid Mechanics,* 159, 19-53.

KERSHAW, R. 1995. Parametrization of momentum transport by convectively generated gravity waves. *Q.J.R. Meteorol. Soc*., 121: 1023–1040.

KING, S. E., CARR, M. & DRITSCHEL, D. G. 2011. The steady-state form of large-amplitude internal solitary waves. *Journal of Fluid Mechanics,* 666, 477-505.

KLAASSEN, G. P. & PELTIER, W. R. 1985a. The effect of prandtl number on the evolution and stability of Kelvin—Helmholtz billows. *Geophysical & Astrophysical Fluid Dynamics,* 32, 23-60.

KLAASSEN, G. P. & PELTIER, W. R. 1985b. The onset of turbulence in finite-amplitude Kelvin Helmholtz billows. *Journal of Fluid Mechanics,* 155, 1-35.

KLAASSEN, G. P. & PELTIER, W. R. 1991. The influence of stratification on secondary instability in free shear layers. *Journal of Fluid Mechanics,* 227, 71-106.

KLYMAK, J. M. & MOUM, J. N. 2003. Internal solitary waves of elevation advancing on a shoaling shelf. *Geophysical Research Letters,* 30, 2045.

KOOP, C. G. & BROWAND, F. K. 1979. Instability and turbulence in a stratified fluid with shear. *Journal of Fluid Mechanics,* 93, 135-159.

KOOP, C. G. & BUTLER, G. 1981. An investigation of internal solitary waves in a two-fluid system. *Journal of Fluid Mechanics,* 112, 225-251.

KUNZE, E., WILLIAMS, A. J. & BRISCOE, M. G. 1990. Observations of shear and vertical stability from a neutrally buoyant float. *Journal of Geophysical Research: Oceans,* 95, 18127-18142.

LAMB, K. G. & FARMER, D. 2011. Instabilities in an Internal Solitary-like Wave on the Oregon Shelf. *Journal of Physical Oceanography,* 41, 67-87.

LAMB, K. G. 2002. A numerical investigation of solitary internal waves with trapped cores formed via shoaling. *Journal of Fluid Mechanics,* 451, 109-144.

LAUNDER, B. E. & SPALDING, D. B. 1974. The numerical computation of turbulent flows. *Computer Methods in Applied Mechanics and Engineering*, 3, 269-289.

LAWRENCE, G. A., BROWAND, F. K. & REDEKOPP, L. B. 1991. The stability of a sheared density interface. *Physics of Fluids*, A3, 2360–2370.

LAWRENCE, G. A., BROWAND, F. K. & REDEKOPP, L. G. 1991. The stability of a sheared density interface. *Physics of Fluids A: Fluid Dynamics,* 3, 2360-2370.

LEE, C.-Y. & BEARDSLEY, R. C. 1974. The generation of long nonlinear internal waves in a weakly stratified shear flow. *Journal of Geophysical Research,* 79, 453-462.

LIEN, R.-C., D'ASARO, E. A., HENYEY, F., CHANG, M.-H., TANG, T.-Y. & YANG, Y.-J. 2012. Trapped Core Formation within a Shoaling Nonlinear Internal Wave. *Journal of Physical Oceanography,* 42, 511-525.

LIU, W., BRETHERTON, F. P., LIU, Z., SMITH, L., LU, H. & RUTLAND, C. J. 2010. Breaking of Progressive Internal Gravity Waves: Convective Instability and Shear Instability. *Journal of Physical Oceanography,* 40, 2243-2263.

LONG, R. R. 1956. Solitary Waves in the One- and Two-Fluid Systems1. *Tellus,* 8, 460-471.

LUCE, H., MEGA, T., YAMAMOTO, M. K., YAMAMOTO, M., HASHIGUCHI, H., FUKAO, S., NISHI, N., TAJIRI, T. & NAKAZATO, M. 2010. Observations of Kelvin-Helmholtz instability at a cloud base with the middle and upper atmosphere (MU) and weather radars. *Journal of Geophysical Research: Atmospheres,* 115, D19116.

M. J. ALBLOWITZ AND H. SEGUR. 1981. *Solitons and the inverse scattering transform*, SIAM.

MICHALLET, H. & BARTHÉLEMY, E. 1998. Experimental study of interfacial solitary waves. *Journal of Fluid Mechanics*, 366, 159-177.

MICHALLET, H. & IVEY, G. N. 1999. Experiments on mixing due to internal solitary waves breaking on uniform slopes. *Journal of Geophysical Research: Oceans,* 104, 13467-13477.

MILES, J. W. 1961. On the stability of heterogeneous shear flows. *Journal of Fluid Mechanics,* 10, 496-508.

MILES, J. W. 1981. The Korteweg-de Vries equation: a historical essay. *Journal of Fluid Mechanics,* 106, 131-147.

MITTENDORF, G. H. 1961. *The instability of stratified flow* [M.Sc. thesis]. State University of Iowa.

MOUM, J. N., FARMER, D. M., SMYTH, W. D., ARMI, L. & VAGLE, S. 2003. Structure and Generation of Turbulence at Interfaces Strained by Internal Solitary Waves Propagating Shoreward over the Continental Shelf. *Journal of Physical Oceanography,* 33, 2093-2112.

MOUM, J. N., KLYMAK, J. M., NASH, J. D., PERLIN, A. & SMYTH, W. D. 2007. Energy Transport by Nonlinear Internal Waves. *Journal of Physical Oceanography,* 37, 1968-1988.

MUNK, W. 1981. *Internal waves and small scale processes*, MIT Press Cambridge.

NASH, J. D. & MOUM J. N. 2005. River plumes as a source of large-amplitude internal waves in the coastal ocean. *Nature.* 437, 400-403.

NATIONAL INSTRUMENTS. 2013. *LabVIEW* [Computer program]. Available at: http://www.ni.com/labview [Accessed 07/04/2014].

OSBORNE, A. R. & BURCH, T. L. 1980. Internal Solitons in the Andaman Sea. *Science,* 208, 451-460.

PACANOWSKI, R. & PHILANDER, S. G. H. 1981. Parameterization of vertical mixing in numerical models of tropical oceans. *Journal of Physical Oceanography*, 11, 1443-1451.

PATNAIK, P. C., SHERMAN, F. S. & CORCOS, G. M. 1976. A numerical simulation of Kelvin-Helmholtz waves of finite amplitude. *Journal of Fluid Mechanics,* 73, 215-240.

PATTERSON, M. D., CAULFIELD, C. P., MCELWAINE, J. N. & DALZIEL, S. B. 2006. Time-dependent mixing in stratified Kelvin-Helmholtz billows: Experimental observations. *Geophysical Research Letters,* 33.

PELTIER, W. R. & CAULFIELD, C. P. 2003. Mixing efficiency in stratified shear flows. *Annual Review of Fluid Mechanics,* 35, 135-167.

PELTIER, W. R. & CAULFIELD, C. P. 2003. Mixing efficiency in stratified shear flows. *Annual Review of Fluid Mechanics*, 35, 135–167.

PELTIER, W. R., HALLÉ, J. & CLARK, T. L. 1978. The evolution of finite amplitude Kelvin-Helmholtz billows. *Geophysical and Astrophysical Fluid Dynamics,*10, 53-87.

PERRY, R. B. & SCHIMKE, G. R. 1965. Large-amplitude internal waves observed off the northwest coast of Sumatra. *Journal of Geophysical Research,* 70, 2319-2324.

PETERS, H. & GREGG, M. C. 1988. Some Dynamical and Statistical Properties of Equatorial Turbulence.

PETERS, H., GREGG, M. C. & SANFORD, T. B. 1995. Detail and scaling of turbulent overturns in the Pacific Equatorial Undercurrent. *Journal of Geophysical Research,* 100, 18349-18368.

POLZIN, K. L., OAKEY, N. S., TOOLE, J. M. & SCHMITT, R. W. 1996. Fine structure and microstructure characteristics across the northwest Atlantic Subtropical Front. *Journal of Geophysical Research: Oceans,* 101, 14111-14121.

PREUSSE, M., STASTNA, M., FREISTÜHLER, H. & PEETERS, F. 2012. Intrinsic Breaking of Internal Solitary Waves in a Deep Lake. *PLoS ONE,* 7(7): e41674.

RAHMANI, M. 2011. *Kelvin-Helmholtz instabilities in sheared density stratified flows* [PhD thesis]. University of British Columbia.

RAMP, S. 2006. *The Windy Islands Soliton Experiment* [Online]. Available: http://www.nps.edu/research/ResTopics/NPS_Solitons.pdf. [Accessed 11/04/2014].

SCHOWALTER, D. G., VAN ATTA, C. W. & LASHERAS, J. C. 1994. Baroclinic Generation of Streamwise Vorticity in a Stratified Shear Layer. *Meccanica*, Vol. 29, 361-371.

SCOTTI, A. & PINEDA, J. 2004. Observation of very large and steep internal waves of elevation near the Massachusetts coast. *Geophysical Research Letters,* 31, 22307.

SCOTTI, R. S. & CORCOS, G. M. 1972. An experiment on the stability of small disturbances in a stratified free shear layer. *Journal of Fluid Mechanics*, 52, 499-528.

SEGUR, H. & HAMMACK, J. L. 1982. Soliton models of long internal waves. *Journal of Fluid Mechanics,* 118, 285-304.

SMITH, W. H. F. & SANDWELL, D. T. 1997. Global Sea Floor Topography from Satellite Altimetry and Ship Depth Soundings. *Science,* 277, 1956-1962.

SMYTH, W. D. & WINTERS, K. B. 2003. Turbulence and Mixing in Holmboe Waves. *Journal of Physical Oceanography,* 33, 694-711.

STRANG, E. J. & FERNANDO, H. J. S. 2001a. Vertical Mixing and Transports through a Stratified Shear Layer. *Journal of Physical Oceanography,* 31, 2026-2048.

STRANG, E. J. & FERNANDO, H. J. S. 2001b. Entrainment and mixing in stratified shear flows. *Journal of Fluid Mechanics,* 428, 349–386.

SUTHERLAND, B. R. 2010. *Internal Gravity Waves*, Cambridge University Press.

SVEEN, J. K., GUO, Y., DAVIES, P. A. & GRUE, J. 2002. On the breaking of internal solitary waves at a ridge. *Journal of Fluid Mechanics,* 469, 161-188.

TAYLOR, G. I. 1931. Effect of Variation in Density on the Stability of Superposed Streams of Fluid. *Proceedings of the Royal Society of London. Series A,* 132, 499-523.

TENNEKES, H. & LUMLEY, J. L. 1972. *A First Course in Turbulence*, MIT press.

THORPE, S. A. 1968. A method of producing a shear flow in a stratified fluid. *Journal of Fluid Mechanics,* 32, 693-704.

THORPE, S. A. 1971. Experiments on the instability of stratified shear flows: miscible fluids. *Journal of Fluid Mechanics,* 46, 299-319.

THORPE, S. A. 1973. Experiments on instability and turbulence in a stratified shear flow. *Journal of Fluid Mechanics,* 61, 731-751.

THORPE, S. A. 1977. Turbulence and Mixing in a Scottish Loch. *Philosophical Transactions of the Royal Society of London. Series A, Mathematical and Physical Sciences,* 286, 125-181.

THORPE, S. A. 1985. Laboratory observations of secondary structures in Kelvin-Helmholtz billows and consequences for ocean mixing. *Geophysical & Astrophysical Fluid Dynamics*, 34, 175-199.

THORPE, S. A. 2007. *An Introduction to Ocean Turbulence*, Cambridge University Press.

THORPE, S. A. 1987. Transitional phenomena and the development of turbulence in stratified fluids: A review. *Journal of Geophysical Research,* 92, 5231–5248.

TOOLE, J. M. & SCHMITT, R. W. 1987. Small-scale structures in the north-west Atlantic sub-tropical front. *Nature,* 327, 47-49.

TROY, C. D. & KOSEFF, J. R. 2005. The instability and breaking of long internal waves. *Journal of Fluid Mechanics,* 543, 107-136.

TURNER, J. S. 1979. *Buoyancy Effects in Fluids,* Cambridge, Cambridge University Press.

WEIDMAN, P. D. & MAXWORTHY, T. 1978. Experiments on strong interactions between solitary waves. *Journal of Fluid Mechanics,* 85, 417-431.

WHITHAM, G. B. 1974. *Linear and Nonlinear Waves*, Interscience.

WINTERS, K. B., LOMBARD, P. N., RILEY, J. J. & D'ASARO, E. A. 1995. Available potential energy and mixing in density-stratified fluids. *Journal of Fluid Mechanics*, 289, 115-128.

WOODS, J. D. 1968. Wave-induced shear instability in the summer thermocline. *Journal of Fluid Mechanics*, 32, 791-800.

ZABUSKY, N. J. & KRUSKAL, M. D. 1965. Interaction of "Solitons" in a Collisionless Plasma and the Recurrence of Initial States. *Physical Review Letters,* 15, 240-243.

ZIEGENBEIN, J. 1970. Spatial observations of short internal waves in the Strait of Gibraltar. *Deep Sea Research and Oceanographic Abstracts,* 17, 867-875.

11 Appendix A – Obtaining a two layer stratification

To summarise the main document:

A tank was filled initially with a homogeneous layer of fluid of density ρ_2 to a thickness H_2. A linearly-stratified layer (pycnocline) of thickness H_1 was then placed above the first layer using the double reservoir technique (Fortuin, 1960; Hill, 2002; Economidou & Hunt, 2009) or the wave technique, such that the density within this layer varied between ρ_2 and ρ_1. The stratified layer was delivered into the main tank via a floating sponge (item 4., Figure 60).

An excess homogenous volume of fluid of density ρ_1 was then added behind a partially-lowered, solid gate. When the gate was removed vertically, an ISW of depression propagated away from the gate on the pycnocline in the main part of the channel.

11.1 The Double reservoir technique

The double reservoir technique can be computer controlled as in Hill (2003), where peristaltic pumps were used to control the flow between tanks to acquire the desired density stratification (Figure 60). Or the double buckets as in Economidou & Hunt (2009), can be driven by pressure head alone (Figure 61).

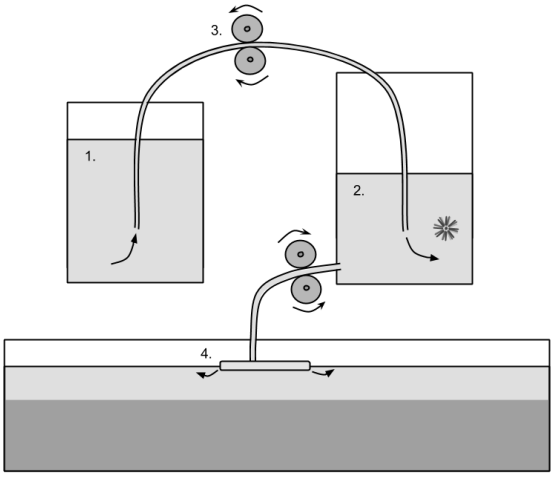

Figure 60 –Double reservoir technique using pumps, the light grey represents less dense water and darker grey more dense.

Figure 60 shows fresh water being pumped from tank 1 into tank 2. In tank 2 a saline solution of density ρ_2 was mixed with the incoming fresh water from tank 1. Initially the water pumped from tank 2 into the main tank was the same as that in the main tank (ρ_2). As more water from tank 1 was added to tank 2 (and mixed) the water entering the main tank from 2 was diluted (the density of the additional water was less than ρ_2). This caused the main tank to become stratified. Due to limitation in the laboratory, the pressure head technique was used to drive the flow when using the double reservoir technique. The stratification obtained using the double bucket (driven with a pressure head) technique was difficult to repeat and it provided a limited range of layer depths, for the following reasons:

- As the fluid entered the tank the pressure head driving the flow was reduced. Thus the rate that the water entered the main tank reduced with time. The time for fluid to be added to the main tank was a critical factor when stratifying. This was avoided when using pumps.
- The sources and magnitude of mixing while the tank was being stratified were difficult to avoid or minimise. For example the floating sponge moved as the water

level changed and when the flow rate was adjusted. If the flow rate was too high the water spreading across the tank would mix with the layer beneath it, reducing the density gradient at that depth in the final density profile. Removing the floating sponge also caused considerable mixing.

- Often a thin stratified layer was required. One approach was to use small volumes of water in tank 1 and 2. This led to impractically low rates of flow from tank 2 into the main tank. An alternative was to use large volumes of water and a bigger density difference but stop the flow when the required depth of fluid was achieved in the main tank. This was acceptable, but the density difference in the stratified layer was difficult to control. Consequently thin stratified layers were difficult to control.
- Tanks 1 and 2 were not big enough to create a thick stratified layer in one go. When they ran almost empty the density of the remaining fluid in tank 2 was measured. Tank 2 was then refilled with fluid of the appropriate density and tank 1 was refilled with fresh water. The process of stratification was then recommenced. This procedure was slow and provided ample opportunity for human error. Refilling tank 2 meant that a temperature gradient could be present in the final stratification. This was undesirable as no instrument was available to measure a temperature gradient.
- When a stratification was chosen, for example a density gradient that ranged from 1020kg/m^3 at the interface to 1000kg/m^3 at the surface. Tank 1 would be filled with water of density 1000kg/m^3 and tank 2 would be filled with water of density 1020kg/m^3. When the final stratification was measure the upper density was rarely realised, the error was in the range ±5kg/m^3.

In summary the double reservoir technique with the apparatus available was not very good at producing small stratified layer or large stratified layers. It had many opportunities for human

error and there were several sources of unquantifiable mixing. Furthermore irrespective of the layer depth required the density gradient across said layer depth was difficult to specify. Finally the whole process was very long an average experiment took 2 days to complete. Another method was sought.

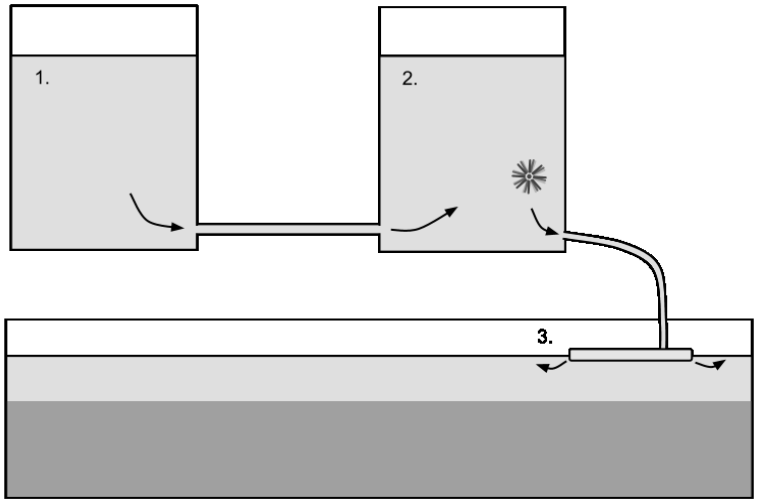

Figure 61 – Double reservoir technique driven by pressure head, the light grey represents less dense water and darker grey more dense

11.2 The wave technique

After experimenting with various techniques it was found that releasing a gravity current provided the desired outcome of a linearly stratified upper layer. The wave method involved releasing a volume of fluid density ρ_1 from behind the gate into the main tank filled with homogenous fluid density ρ_2 (Figure 62). When the tank had come to rest a linear stratification remained that varied from ρ_2 to a value slightly less than ρ_1.

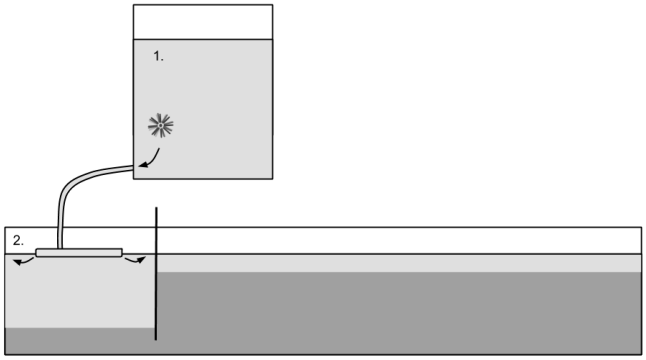

Figure 62 – Wave method, the light grey represents less dense water and darker grey more dense.

The method had several benefits:

- It was quicker to set up when compared to the double reservoir technique.
- There was less opportunity for human error when compared to the double reservoir technique.
- There was more control over the stratified layer thickness and they were easy to repeat.
- There was more control over the density change across the stratified region, and stratifications were easy to repeat.
- Very thin stratified layers became available as well as very thick stratified layers.
- Avoiding remixing fluid for thick stratified layers avoided temperature stratification.
- There was less opportunity for mixing in the main tank.

Consequently this alternative method (wave method) was used for all the reported 2 layer experiments. The main drawback of the wave method was that the upper density in the stratified layer (at the surface) could not be predicted exactly. This was a drawback shared with the double reservoir technique. The upper density of the stratified region was an important variable as this was the density that the wave would have. The following section discusses this in detail.

12 Appendix B – Matching ρ_{wave} to ρ_1

Following from the previous section, once the stratification was established in the main tank the exact density at the surface of the tank was unknown. The conductivity sensors were aligned with the surface of the water. The sensors were driven through the stratification slowly and the vertical density profile was obtained. This information was used to set the density of water that was added behind the gate to create the ISW.

When there was a mismatch in density between the ISW volume behind the gate and the stratification it was moving into, unusual behaviour was found (Figure 63). If the wave volume had a density that was lighter than any density found in the stratification it was moving into then a wave like current propagating at the surface (Figure 63*(b)*) was expected. If the ISW density was some density that was found in the stratification, the volume of water behind the gate would propagate at its neutral density at some depth. Depending on where in the stratification said depth was, ISW like behaviour was possible (Figure 63*(c)*), tending towards a bulge lower in the stratification (Figure 63*(d)*).

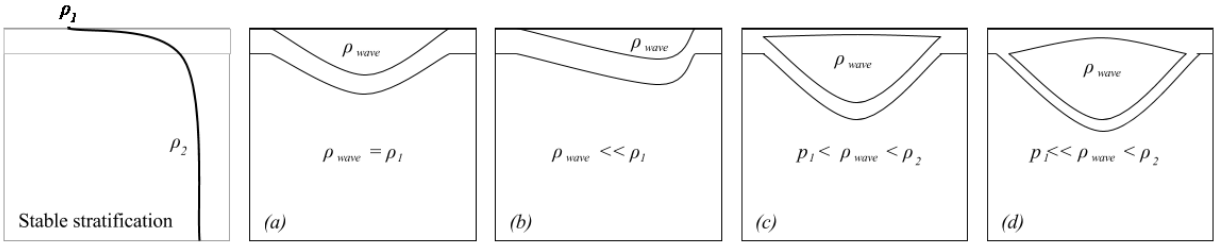

Figure 63 – Possible outcomes of a density mismatch between the density of the ISW volume added behind the gate and the stratification it propagated into when the gate was released. The variation between these parameters is given in the figure.

Only in cases where a match was achieved (Figure 63*(a)*) was an experiment considered successful. Obviously in cases where the wave density was much less than the density of the stratification (Figure 63*(b)*) the error was easy to identify by eye. Experiments where the

wave was propagating at its neutral buoyancy (Figure 63*(c)*, *(d)*) were more difficult to spot. Prior to the experiment running these (Figure 63*(c)*, *(d)*) cases were easy to identify. If a density mismatch was present the trapped part of the pycnocline that was normally depressed by the additional volume spilt, which can be seen by eye (Figure 64).

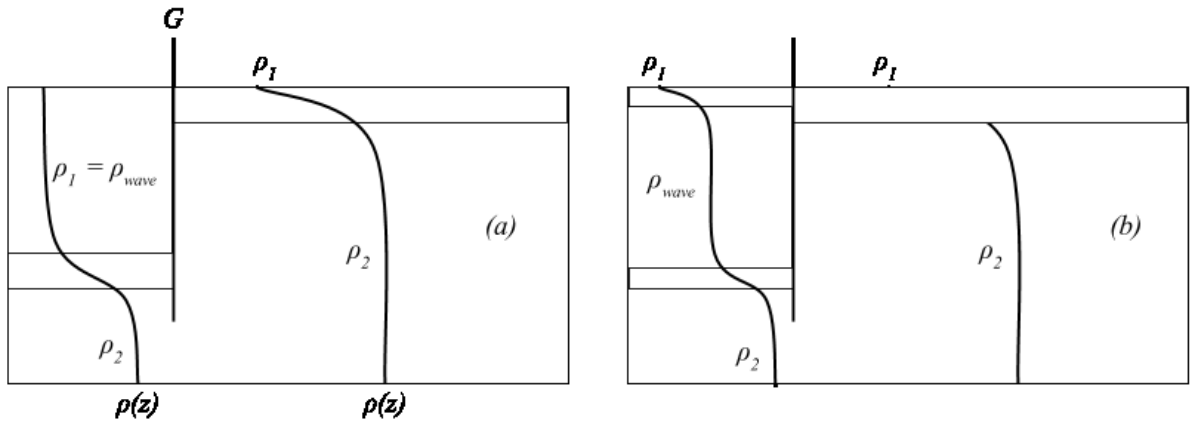

Figure 64 – (a) The correct experimental setup for an ISW. (b) A density mismatch behind the gate prior to the experiment running.

Waves like those shown in Figure 63*(c)*, *(d)* and Figure 64*(b)* may well behave like ISWs but the technique used to measure the buoyancy frequency prevented these failed experiments from being analysed fully. The buoyancy frequency was measured, as explained earlier, using the conductivity sensors in the main tank prior to the experiment running. Clearly this value is not going to represent a wave that is splitting the pycnocline while propagating at its neutral buoyancy and depth.

13 Appendix C – Calibrating the sensors

To summarise the main document:

The rapid response micro-conductivity sensors (Head, 1983) were calibrated in advance of the experiment using saline solutions of known density and ambient temperature, additional calibration information was gained during the experiment to ensure a good match. The acquisition rate of the ADC was set to 2000 Hz.

A typical base line calibration can be seen in Figure 65, the sensor appeared to be behaving linearly. Error bars represent a ±2 Kg/m^3 confidence in the density reading measured with a hydrometer. At this stage it can be seen that the sensor was working correctly and the experimental setup can commence.

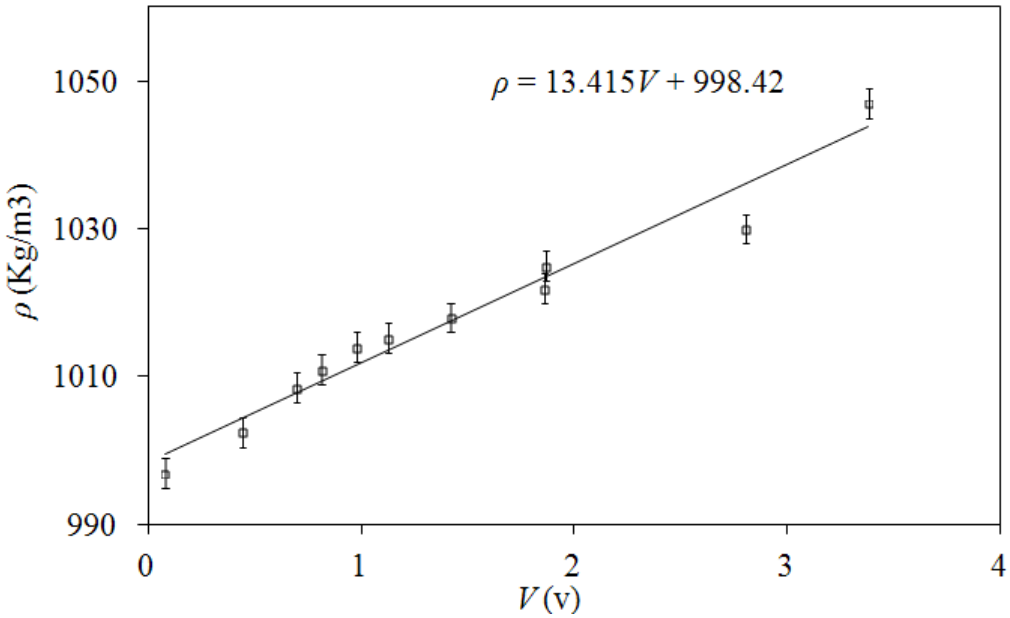

Figure 65 – Measured density versus voltage from the sensor

During the experiment the base line calibration was added to with a measurement from fresh water and a measurement from the homogenous lower layer in the main tank, these two points can be seen in Figure 66.

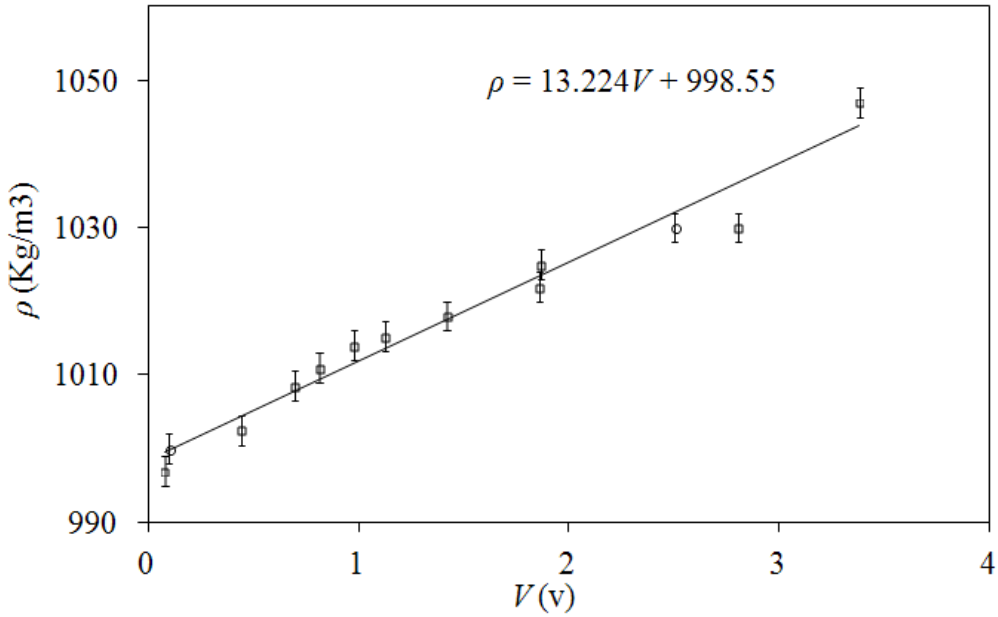

Figure 66 – Measured density versus voltage from the sensor, circular symbols represent the additional data.

This was the final calibration that was used to convert the ADC data to density values. It was necessary to assume that there was no variation with temperature between the calibrations. Every effort was made to ensure that the water was at an ambient temperature before a calibration took place. It is worth noting that the variation of density with the temperatures and pressures experience in the lab would be less than 1 Kg/m^3 which is below the accuracy of the measurement device used to measure density.

As mentioned earlier in the document the acquisition rate of the ADC was set to 2000 Hz in the software. This rate is well above the maximum response frequency of the sensor which was approximately 800 Hz and also well above the Nyquist limit of the sampled data (1600 Hz).

14 Appendix D – Sensor information

Excerpts from the PME's web site giving detailed sensor information are given below.

Fast Conductivity Sensor

The Fast Conductivity Sensor is designed to make very rapid, high resolution measurements of electrical conductivity of water. The sensor consists of four electrodes (platinum spheres) supported by fused glass. Each electrode is electroplated with an amorphous platinum coating. The picture to the right shows typical dimensions. This sensor can be used for investigating turbulent mixing in stratified fluids.

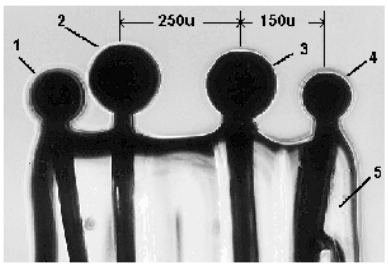

This sensor must be used in conjunction with suitable electronics such as the MicroScale Conductivity and Temperature Instrument, and SCAMP (available through PME). The sensor functions by being a dimensionally stable contact between the water around the sensor and the electronic circuit. This circuit makes a four terminal measurement of the conductance of the water supplying an A.C. current between the inner electrodes of the sensor and measuring the A.C. voltage that develops across the outer electrodes.

The conductivity-averaging nature of this sensor causes it to have the property of spatial resolution. The sensor will respond to conductivity features that are large compared to the separation between the inner electrodes and is increasingly less sensitive to increasingly smaller features.

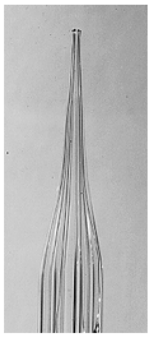

The spatial averaging volume of the sensor can be estimated to be a sphere of radius 1/2 mm centered between the inner electrodes. This is only an approximation however of the actual sensitivity described by a complicated weighting function applied to all points around the sensor.

The spatial resolution can also be described in wave number space: the sensor attenuates the measurement 3bd at approximately 4 cycles/cm.

Features

- Measurement of very rapid temperature fluctuations under special circumstances
- Measurement of double diffusive features
- Measurement of mean density profiles (as part of a buoyancy flux measurement system)
- Measurement of bubble concentration
- Measurement of interface position

Request MSCTI Quote

- Head, M.J., **The Use of Miniature Four-Electrode Conductivity Probes for High Resolution Measurement of Turbulent Density or Temperature Variations in Salt-Stratified Water Flows**, *Ph.D. Thesis, University of California, San Diego*, 1983.

Figure 67 – Excerpts from the PME's web site giving Fast conductivity sensor details.

HEAD, K. 2014. Fast Conductivity Sensor [online]. Available: http://www.pme.com/HTML%20Docs/Mscti_FastC.html [Accessed 20/05/2014]

MSCTI Components

- Analog voltage outputs for conductivity and temperature.
- Electronic bridge performs amplification and control functions.
- Probe-preamplifier consists of the fast conductivity and temperature sensor on a 0.25 inch diameter stainless steel shaft.
- Power supply is a wall-mounted or tabletop transformer that supplies +/- 12 VDC from 120 VAC 60 Hz or other AC source upon request.
- Replacement sensors include the Fast Conductivity and the Fast Conductivity and Temperature sensors.

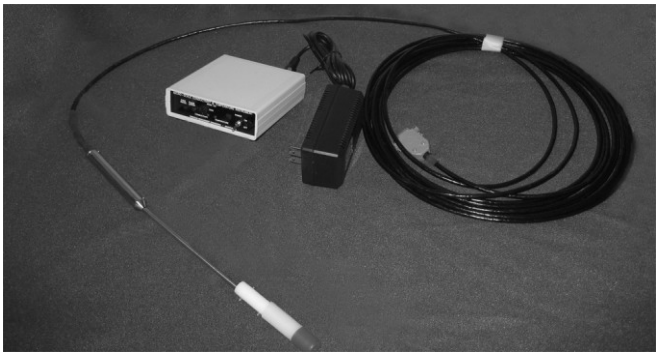

Figure 68 – Excerpts from the PME's web site giving MicroScale Conductivity and Temperature Instrument details.

HEAD, K. 2014. MicroScale Conductivity and Temperature Instrument [online]. Available: http://www.pme.com/HTML%20Docs/Mscti_home2.html [Accessed 20/05/2014]

15 Appendix E – Acquisition card (DAS1000) information

Excerpts from the MCC's web site giving detailed PCI-DAS1000 information are given below.

Overview: PCI-DAS1000 features

This manual explains how to install and use the PCI-DAS1000. This board is a multifunction analog and digital I/O board designed for the PCI bus.

The PCI-DAS1000 provides either 16 single-ended or eight differential analog inputs. Input ranges are software-selectable as either bipolar or unipolar.

Analog input ranges for the PCI-DAS1000 are:

- Bipolar: ±10 V, ±5 V, ±2.5 V, and ±1.25 V
- Unipolar: 0 to 10 V, 0 to 5 V, 0 to 2.5 V and 0 to 1.25 V

The PCI-DAS1000 provides a 250 kHz sample rate.

The PCI-DAS1000 offers 24-bits of parallel, digital I/O (two 8-bit ports and two 4-bit ports). You can configure each port independently as input or output.

This board has an 82C54 counter chip which has three user-accessible 16-bit counters. Clock, gate, and output signals from two of three counters are available on a 100-pin connector. The third counter is used internally.

The PCI-DAS1000 is fully plug-and-play. All addresses and interrupt channels are set with software.

Figure 69 – Excerpts from the Measurement Computing's web site giving PCI DAS1000 details.

MCC. 2014. PCI-DAS1000 Users guide [online]. Available: : http://www.mccdaq.com/PDFs/Manuals/PCI-DAS1000.pdf [Accessed 20/05/2014]

Analog input

Table 1. Analog input specifications

Parameter	Specification
A/D converter type	*7800*
Resolution	12 bits
Number of channels	8 differential or 16 single-ended, software selectable
Input ranges	±10 V, ±5 V, ±2.5 V, ±1.25 V, 0 to 10 V, 0 to 5 V, 0 to 2.5 V, 0 to 1.25 V. Fully programmable
Polarity	Unipolar/bipolar, software selectable
A/D pacing	Programmable: Internal counter or external source (A/D External Pacer, positive or negative edge selectable by software), or software polled
Burst mode	Software selectable option, rate = 4 µs
A/D trigger sources	External digital (A/D External Trigger)
A/D triggering modes	Digital: Software enabled, rising edge, hardware trigger Pre-trigger: Unlimited pre- and post-trigger samples. Total # of samples must be > 512.
Data transfer	From 1024 sample FIFO via REPINSW, interrupt or software polled
A/D conversion time	*3 µs*
Throughput	250 kHz
Relative accuracy	±1.5 LSB
Differential linearity error	±0.75 LSB
Integral linearity error	±0.5 LSB typ, ±1.5 LSB max
Gain error (relative to calibration reference)	± 0.02% of reading, max
No missing codes guaranteed	*12 bits*
Calibration	Auto-calibration, calibration factors for each range stored on board in non-volatile RAM
Gain drift (A/D specs)	*±6 ppm/°C*
Zero drift (A/D specs)	*±1 ppm/°C*
Common mode range	±10 V
CMRR @ 60 Hz	70 dB
Input leakage current	*200 nA*
Input impedance	*10 MOhms, min*
Absolute maximum input voltage	*Channels 1-15: -40 V to +55 V power on or off;* *Channel 0 : ±15 V*
Noise distribution	Rate = 1-250 kHz, average % ±2 bins, average % ±1 bin, average # bins
	All bipolar ranges: 100% / 99.5% / 4 bins All unipolar ranges: 100% / 99% / 5 bins

Figure 70 – Excerpts from the Measurement Computing's web site giving PCI DAS1000 details.

MCC. 2014. PCI-DAS1000 Users guide [online]. Available: : http://www.mccdaq.com/PDFs/Manuals/PCI-DAS1000.pdf [Accessed 20/05/2014]

PCI-DAS1000 block diagram

PCI-DAS1000 functions are illustrated in the block diagram shown here.

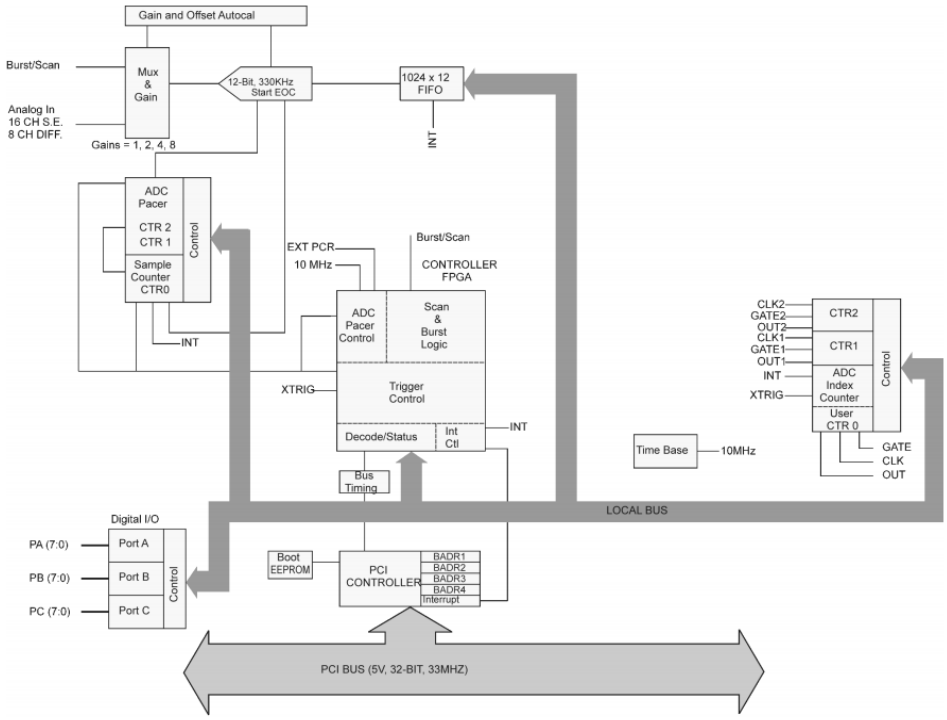

Figure 1. PCI-DAS1000 functional block diagram

Figure 71 – Excerpts from the Measurement Computing's web site giving PCI DAS1000 details.

MCC. 2014. PCI-DAS1000 Users guide [online]. Available: http://www.mccdaq.com/PDFs/Manuals/PCI-DAS1000.pdf [Accessed 20/05/2014]

16 Appendix F – BNC connection box (BNC-16SE) information

Excerpts from the MCC's web site giving BNC-16E terminal board information are given below.

The BNC series of signal connection boxes have been designed as universal interfaces for the DAS family of analog I/O boards. The BNC-08DI accepts up to 8 differential pairs of analog inputs while the BNC-16SE and the BNC-16DI can accept up to 64 single ended or 32 differential analog inputs. For user convenience, a variety of I/O signals from the DAS board are brought out to a 37 pin D connector at the front of the enclosure.

Figure 72 – Excerpts from the OMEGA web site giving BNC-16SE Terminal Board details.

OMEGA. 2014. BNC-16SE Terminal Board Users guide [online]. Available: http://www.omega.com/manuals/manualpdf/MBNC16.pdf [Accessed 20/05/2014].

17 Appendix G - Producing a single ISW

As mentioned in the main text the length L_G (Figure 10) was chosen so that when the gate was removed a single ISW was generated rather than a train of ISWs. Kao *et al*. (1985) offered an equation (Equation 35) to estimate the number (N_w) of ISWs produced and demonstrated good experimental agreement with this equation. Where the layer depths $\hat{H}_1$ and $\hat{H}_2$ were estimated by: $\hat{H}_1=H_1+(H_2/2)$, $\hat{H}_2=H_3+(H_2/2)$ and where η_0 was the excursion of the pycnocline due to the volume added behind the gate.

$N_w \leq 1+(S/\pi)$ Where: $S= L_G\,[(3/2)\,\eta_0\,(\hat{H}_1 - \hat{H}_2 / \hat{H}_1^2 - \hat{H}_2^2)]^{1/2}$ Equation 35

Figure 73 shows the effect of varying η_0, $\hat{H}_1$ and L_G. It can be seen that the step depth (excursion) has little affect on the number of ISWs produced when L_G was small. It can also be seen that for any given L_G, $\hat{H}_1$ had a big influence on the number of ISWs generated. It appeared that if L_G was small, and small values of $\hat{H}_1$ were avoided, a single ISW would be produced whilst retaining the freedom to vary the excursion without the worry of producing two or more ISWs.

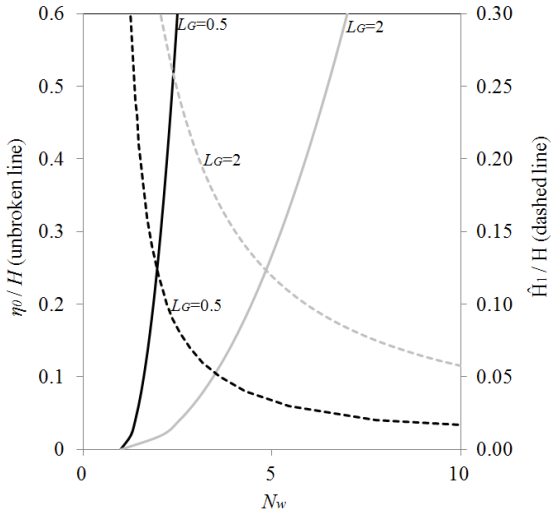

Figure 73 – Plot showing the variation of non-dimensional excursion $\hat{H}_1$, and L_G with N. The right hand axis applies to the dashed lines $\hat{H}_1/H$. The left hand axis applies to the unbroken line (excursion). The variation of L_G is marked accordingly.

18 Appendix H – Experimental parameters (3 layer experiments)

exp	Run	a/H (±8%)	C/C_o (±6%)	h_1/H (±2%)	h_2/H (±5%)	h_3/H (±0%)	dz/H (±5%)	N (s^{-1}) (±10%)	R (±5%)	Ri_{min} (±8%)
081010	1	0.275	1.61	0.101	0.048	0.851	0.031	2.59	0.6	0.05
071010	2	0.319	1.59	0.084	0.046	0.871	0.031	2.59	0.7	0.04
160910	4	0.340	1.57	0.081	0.042	0.877	0.036	2.74	0.9	0.06
111010	5	0.294	1.44	0.123	0.029	0.848	0.025	3.34	0.9	0.05
240910	6	0.327	1.71	0.077	0.041	0.882	0.036	2.80	0.9	0.06
121010	7	0.317	1.57	0.082	0.035	0.883	0.032	3.03	0.9	0.06
300910	8	0.363	1.68	0.066	0.048	0.886	0.046	2.58	1.0	0.08
191010	9	0.332	1.61	0.086	0.038	0.876	0.037	2.88	1.0	0.07
201010	10	0.322	1.51	0.100	0.027	0.873	0.027	3.44	1.0	0.07
141010	11	0.272	1.41	0.125	0.026	0.849	0.029	3.48	1.1	0.07
131010	12	0.336	1.71	0.082	0.032	0.886	0.037	3.18	1.2	0.09
200910	13	0.317	1.63	0.082	0.029	0.889	0.036	3.37	1.3	0.08
230910	14	0.322	1.74	0.072	0.028	0.900	0.036	3.38	1.3	0.09
290910	15	0.342	1.64	0.076	0.033	0.891	0.042	3.12	1.3	0.10
280910	16	0.286	1.64	0.079	0.025	0.896	0.035	3.59	1.4	0.11
210910	17	0.303	1.70	0.077	0.022	0.901	0.033	3.75	1.5	0.10
011010	18	0.321	1.35	0.117	0.022	0.861	0.037	3.65	1.7	0.12
051010	19	0.267	1.35	0.123	0.023	0.854	0.048	3.83	2.1	0.25
061010	20	0.294	1.26	0.169	0.029	0.802	0.064	3.43	2.2	0.32

Table 1 – Summary of parameter for all experimental runs, where c_0 was the wave speed predicted by linear wave theory see Frutus et al (2009) for more details. Ri_{min} was the minimum gradient Richardson number at the ISW peak.

19 Appendix I - Experimental parameters (2 layer experiments)

exp	*H1/H*	*H2/H*	*dz* (*m*)	*N* (*s*$^{-1}$)	Ri_g	%ΔPB	*a/H*	c/c_0	*R*
140212	0.14	0.86	0.05	2.47	0.24	0.78	0.34	0.61	0.92
010212	0.06	0.94	0.03	3.74	0.25	1.23	0.41	1.33	1.55
200212	0.05	0.95	0.03	2.31	0.26	0.65	0.37	2.63	1.70
080112	0.08	0.92	0.04	3.13	0.26	1.24	0.44	1.17	1.39
170212	0.08	0.92	0.05	1.81	0.27	1.02	0.41	1.72	1.48
160212	0.12	0.88	0.05	2.01	0.33	0.99	0.39	1.01	1.10
161211	0.10	0.90	0.04	2.42	0.33	0.54	0.42	1.11	1.22
240112	0.06	0.94	0.04	3.72	0.34	0.60	0.34	1.27	1.46
180112	0.11	0.89	0.05	1.98	0.40	0.90	0.41	1.33	1.31
230112	0.12	0.88	0.05	2.47	0.40	0.36	0.33	0.74	1.18
020212	0.05	0.95	0.02	4.42	0.47	0.50	0.23	1.11	1.28
211211	0.12	0.88	0.06	2.13	0.51	0.52	0.41	0.82	1.39
100112	0.06	0.94	0.04	4.11	0.51	0.43	0.33	1.23	1.90
171211	0.12	0.88	0.07	2.10	0.54	0.22	0.45	0.85	1.64
221211	0.09	0.91	0.06	3.00	0.55	1.07	0.41	0.81	1.71
250112	0.10	0.90	0.06	2.68	0.59	0.67	0.38	0.94	1.57
030212	0.08	0.92	0.04	3.21	0.62	1.44	0.27	0.83	1.33
170112	0.07	0.93	0.04	3.37	0.66	0.83	0.25	0.82	1.59
090112	0.05	0.95	0.06	4.27	0.86	0.69	0.38	1.39	3.07
200112	0.05	0.95	0.05	4.62	1.32	0.58	0.24	1.21	2.59
230212	0.04	0.96	0.07	2.52	1.43	0.51	0.35	3.19	4.47

Table 2 – Summary of parameter ranges for all experimental runs